Development of water electrolyzers with additive manufacturing for efficient and low-cost energy conversion and storage

A Dissertation Presented for the

Doctor of Philosophy

Degree

The University of Tennessee, Knoxville

Gaoqiang Yang

December 2018

ACKNOWLEDGEMENTS

As the old Chinese adage goes, deep gratitude to mentor outgoes the sea. So my special appreciation goes to my advisor, Dr. Feng-Yuan Zhang, who has been a tremendous mentor for me during my doctoral study. Thanks for encouraging my research and for making me growing as a young research scientist. I would like to express my gratitude to Dr. Matthew M. Mench, Dr. Reza Abedi, Dr. Lloyd M. Davis, and Dr. Zhili Zhang for serving as my committee members. Their academic expertise, earnestness, and brilliant comments and suggestions have been invaluable on my research career.

My sincere thanks also goes to our group members, Dr. Jingke Mo, Dr. Zhenye Kang, Dr. Bo Han, Yifan Li, Shule Yu, Dr. Qiang Yang, Derrick A Talley, Yeshi Dohrmann, and Stuart M. Steen III, who supported me for everything in my research and daily life. I want to express my appreciation to Douglas Warnberg, Alexander Terekhov, Kathleen Lansford, Dr. Lee Leonard, Dr. Lino Costa, and Natallia Kaptur, who gave access to the laboratory and research facilities, and to my friends, Hang Wang, and Zefeng Lyu for all the fun we have had.

I thank Dr. Sudarsanam S. Babu, Frederick A. List III, Dr. Scott T. Retterer, Dr. David A. Cullen, Dr. Todd J. Toops, Dr. Michael P. Brady, Dale Hensley, Kevin C. Lester, and Dr. Bernadeta R. Srijanto from ORNL; Dr. Johney B. Green Jr., Dr. Guido Bender, and Dr. Bryan S. Pivovar from NREL; and Dr. Haiying Huang from the University of Texas for their advice and help.

I am grateful for the support from U.S. Department of Energy's National Energy Technology Laboratory under Award DE-FE0011585, and National Renewable Energy Laboratory under Award DE-AC36-08GO28308.

A special thanks to my beloved family, my parents, my brother, my sisters, and my girlfriend for all the sacrifices they have made. I can't thank them enough for their support, which sustained me during the three years' study abroad. I believe my grandparents in heaven can see their grandson is going to earn a Ph.D degree. May they rest in peace.

ABSTRACT

Hydrogen is considered as an environmentally friendly storage medium for renewable energies and has attracted extensive attention, since it can provide 2.5 times as much energy per unit mass as fossil fuels, and provide hazard-free products. As an effective method for hydrogen production, the proton exchange membrane electrolyzer cell (PEMEC) provides a number of advantages: rapid response to the power input, compact system design, high purity product (up to 99.995%), high operation current density (above 2 A/cm^2), and high operation pressure (up to 350 bar). Due to insufficient performance and high cost of PEMEC stacks, the use of hydrogen as large-scale energy storage with PEMECs has been limited so far. Thus, low-cost and high-efficiency PEMECs are highly desirable to establish a clean and sustainable energy infrastructure. To bridge the gap between lab-scale and industrial hydrogen productions, the main objectives in this research include: (1) Exploring the possibility of application of metallic additive manufacturing (AM) on PEMECs. (2) Integrating the components of PEMECs into one part with better performance and compact system design by using AM technologies. (3) Bipolar plate development with AM and protective coating for durable and high-efficiency PEMECs. (4) Combination of AM non-conductive bipolar plate with thin film liquid/gas diffusion layers for low-cost hydrogen production. (5) Developing conductive mesoporous bi-material catalysts with ultra-high reaction sites and efficiency for oxygen evolution reaction in PEMEC by using advanced manufacturing. Those bipolar plates and membrane electrode assemblies (MEAs) with excellent electrochemical performance and low cost will open a pathway for developing

widely available water electrolyzers or other energy conversion devices, such as batteries, solar cells, and fuel cells.

TABLE OF CONTENTS

CHAPTER I INTRODUCTION 1

1.1 Overview 1

1.2 Background and literature review 4

1.3 Motivation and objectives 10

References 11

CHAPTER II ADDITIVE MANUFACTURED BIPOLAR PLATE FOR HIGH-EFFICIENCY HYDROGEN PRODUCTION IN PROTON EXCHANGE MEMBRANE ELECTROLYZER CELLS 24

2.1 Abstract 25

2.2 Introduction 26

2.3 Experimental details 28

2.4 Results and discussion 31

2.4 Summary 37

References 39

CHAPTER III FULLY PRINTED AND INTEGRATED ELECTROLYZER CELLS WITH ADDITIVE MANUFACTURING FOR HIGH-EFFICIENCY WATER SPLITTING 44

3.1 Graphical Abstract 45

3.2 Abstract 46

3.3 Highlights 46

3.4 Introduction 47
3.5 Experimental 50
3.5.1 Fabrication of AM plates 50
3.5.2 Characterization and testing system 52
3.6 Results and discussion 54
3.6.1 Ex-situ measurements 54
3.6.2 Polarization curves and EIS 59
3.6.3 Quantifications of AM plates on PEMEC performance 65
3.6.4 Stability 68
3.7 Conclusions 70
References 72
CHAPTER IV BIPOLAR PLATE DEVELOPMENT WITH ADDITIVE MANUFACTURING AND PROTECTIVE COATING FOR DURABLE AND HIGH-EFFICIENCY HYDROGEN PRODUCTION 81
4.1 Abstract 82
4.2 Highlights 83
4.3 Introduction 83
4.4 Experimental details 88
4.4.1 Additive manufacturing of BPs 88
4.4.2 Gold protective coating 88
4.4.3 Characterization and testing system 89

4.5 Results and discussion 92
4.5.1 Ex-situ measurements 92
4.5.2 Polarization curves and EIS 98
4.5.3 Stability 101
4.6 Conclusions 104
References 105
CHAPTER V A NOVEL PEMEC WITH 3D PRINTED NON-CONDUCTIVE BIPOLAR PLATE FOR LOW-COST HYDROGEN PRODUCTION FROM WATER ELECTROLYSIS 116
5.1 Abstract 117
5.2 Introduction 118
5.3 Experimental details 123
5.4 Results and discussions 127
5.4.1 Ex-situ analysis 127
5.4.2 Electrochemical full-cell measurements 130
5.4.3 Stability assessment 135
5.4.4 Simulation analysis for BPs with different resistivity 137
5.5 Conclusion 141
References 143
CHAPTER VI ADDITIVE MANUFACTURED MICRO-SENSOR FROM SILVER NANOPARTICLES FOR MEASURING SHEAR STRESS AND PRESSURE 152

6.1 Abstract 153
6.2 Background 154
6.3 Current results 155
References 162
CHAPTER VII 2-D CONDUCTIVE MESOPOROUS BI-MATERIAL CATALYSTS (CMBMCS) ENABLES ULTRA-HIGH REACTION SITES AND EFFICIENCY FOR OXYGEN EVOLUTION REACTION 165
7.1 Graphic abstract 167
7.2 Abstract 168
7.3 Introduction 168
7.4 Fabrication method 172
7.4.1 Synthesis of CMBMCs 172
7.4.2 Ex-situ Characterization 173
7.5 Results 174
7.5.1 Ex-situ characterization 174
7.5.2 Electrocatalystic water splitting 178
7.5.3 Visualization and current mapping 184
7.5.4 Performance with different catalyst loadings 189
7.6 Summary 191
References 192
Appendix 198

CHAPTER VIII CONCLUSIONS AND FUTURE RESEARCH 202

VITA 206

LIST OF TABLES

Table 1. Characteristics and working conditions of AM PEMECs. 53

Table 2. Evaluation of different cathodes. 60

Table 3. The EEC fitting parameters of EIS of different cells at 1.0 A/cm2 and 80 °C (A1 – cell with AM plate with parallel flow channel; A2 – cell with AM plate with pin flow channel; A3 – cell with AM integrated plate with pin flow channel and LGDL.)..... 67

Table 4. Configurations of different PEMECs. 125

Table 5. Relative data of different materials for BP manufacturing. 129

Table 6. Parameters for the simulation of PEMECs with BPs with different resistivity. 140

LIST OF FIGURES

Figure 1. Schematic of a PEMEC. 3

Figure 2. Mass, proton and electron transport path in PEMECs. 5

Figure 3. (a). Schematic of SLM technology. (b) Configuration of AM PEMEC, 1-anode end plate, 2- anode current distributor, 3- graphite bipolar plate, 4- anode gasket, 5-Ti felt LGDL, 6- CCM, 7- carbon paper LGDL, 8- cathode gasket, 9- AM SS bipolar plate, 10- cathode end plate. 29

Figure 4. Photographic and SEM images of the AM cathode bipolar plate before and after polishing. (a) SEM image of land before polishing. (b) SEM image of land after polishing. (c) Photo before polishing. (d) Photo after polishing..... 32

Figure 5. EDS spectrum of AM SS 316L cathode bipolar plate..... 34

Figure 6. (a). Polarization curves of PEMEC with AM SS cathode bipolar plate at different temperatures. (b). EIS results of PEMECs with AM SS cathode bipolar plates at different temperatures. 36

Figure 7. Schematic illustration of the integration of current distributor, bipolar plate, gasket, and LGDL into one AM plate via additive manufacturing..... 51

Figure 8. (a). EDS analysis of AM plates. (b). XRD analysis of AM plates..... 56

Figure 9. Schematics of (a) parallel flow channel, (b) pin flow channel, and (c) pin flow channel with LGDL; Photographs of (d) AM plate with parallel flow channel after printing and polishing, (e) AM plate with pin flow channel after polishing, and (f) AM integrated plate with pin flow channel with LGDL after polishing; SEM images of (g)

parallel flow channel of AM plate, (h) pin flow channel of AM plate, and (i) LGDL of AM plate. 57

Figure 10. (a) Polarization curves and (b) EIS results of PEMECs with different cathode plates. (c) Polarization curves and (d) EIS results of PEMECs AM integrated plate with pin flow channel and LGDL at different temperatures. 64

Figure 11. (a) Simplified illustration of ion and electron exchange processes across PEMECs. (b) Equivalent electrical circuit. (c) In-situ EIS results and the EEC fitting of AM PEMECs with pin flow channel and LGDL. 66

Figure 12. (a) Stability test of PEMECs with AM plate with pin and LGDL. (b) SEM image of AM plate before stability test and its corresponding (c) Fe and (d) O EDS mappings. (d) SEM image of AM plate after stability test and its corresponding (f) Fe and (g) O EDS mappings. 69

Figure 13. Schematic of (a) the internal structure of a PEMEC, (b) manufacturing processes of Au-coated AM SS BPs. 87

Figure 14. Schematics of (a) Gold striking on AM SS BP. (b) Gold plating on AM SS BP. 90

Figure 15. Photos of AM SS BPs (a) after printing, (b) after polishing, (c) and after electroplating. SEM images of AM SS BPs (d) after printing, (e) cross section of Au-coated AM SS BPs, and (f) the corresponding EDS mapping. 94

Figure 16. EDS of AM BP (a) before and (b) after electroplating. XRD images of (c) AM SS BP and standard SS 316L, and (d) AM SS BP after electroplating. 95

Figure 17. Setup schematics for ohmic resistance measurements (Set 1) and ICR measurements (Set 2). (b) Results of ICR measurements..... 97

Figure 18. (a) Polarization curves and (c) EIS results of PEMECs with different cathode plates. (b) Polarization curves and (d) EIS results of PEMECs with AM integrated plates at different temperatures. The EIS results are recorded at the frequency range of 200 kHz to 30 mHz..... 100

Figure 19. (a) Potentiodynamic polarization curves of AM SS BPs with and without Au-coating at a scanning rate of 50 mV/s. And (b) potentiostatic polarization curves of AM SS BPs with Au-coating over 100 h. Those tests are in pH2 H_2SO_4 solution bubbled with O_2 at 22 ^oC..... 103

Figure 20. Schematic of (a) manufacturing non-conductive PLA BP with FDM, and (b) wet etching process for developing TF-LGDL. Configuration and electron-conducting path of (c) conventional PEMEC and (d) PEMEC with PLA BPs. 122

Figure 21. Printed BPs and etched TF-LGDL. Images of surface of (a) CGPLA BP, (b) PLA BP, and (c) TF-LGDL. Images of cross-section of (d) CGPLA BP and (e) PLA BP. (g,k) SEM images of cross-section of CGPLA BP. (h, f) SEM images of surface of CGPLA BP. (i, l) SEM images of cross-section of PLA BP. (j, m) SEM images of surface of PLA BP. (f, n) Microscopy images of TF-LGDL etched area. 128

Figure 22. (a) Normalized materials cost, and (b) weight of BPs..... 131

Figure 23. Electrochemical performance of PEMECs with different BPs. (a) Polarization curves recorded on PEMECs with CGPLA BP at cathode (gray), PLA BPs at both

sides(cyan), PLA BPs at cathode(red), graphite BPs at both sides(green). (b) Hydrogen generation rate and normalized hydrogen production rates per unite BP cost at 2.32 V. (c) HFRs recorded on PEMECs and (d) the corresponded zoomed-in graph of (c). 133

Figure 24. Chronopotentiometry measurements of PEMEC with A/C- PLA BP at 200 mA/cm^2 and 20 ^oC for 100 h. 136

Figure 25. (a) MATLAB/Simulink model schematic of PEMECs with different BPs. (b) Simulated polarization curves. (c) Simulated cell voltage (red line), and percentage of voltage for BP resistance in total voltage (dark blue line) vary with BP resistivity, and (d) corresponded zoomed-in graph of c. 138

Figure 26. Photo of 3D ink jet printer. 155

Figure 27. Drop watcher view of droplet. 156

Figure 28. Flexible micro-sensor. 157

Figure 29. SEM and EDS images of the silver films. (a) SEM image of the silver films before sintering at 200 °C. (b) SEM image of the silver films after sintering at 200 °C. (c) EDS analysis of the silver films before sintering at 200 °C. (b) EDS analysis of the silver films after sintering at 200 °C. 158

Figure 30. Surface profile image of the antenna after sintering at 200 °C. 159

Figure 31. Change of resistivity of silver films with sintering temperature. 159

Figure 32. Antenna sensor bonded on a printed circuit board. 161

Figure 33. Measured S11 parameter of the antenna sensor. 161

Figure 34. Synthetic process and reaction pathway of CMBMCs. (a) Spraying of nafion membrane, (b) depositing AuNLs with sputter coating, and (c) inkjet printing of CL with IrO_2NP ink. (2) Reaction pathway on CMBMCs. 171

Figure 35. SEM images of CMBMCs with (a) 10 um scale bar and with (b) 500 nm scale bare. (c) SEM image of Cross-section of CMBMCs. (d) Sheet resistances of CMBMCs with different thicknesses of AuNLs before testing (yellow line), after testing (wine line), and in theoretical (green line). 177

Figure 36. Electrochemical performance of CMBMCs with AuNL thicknesses range from 0-197 nm in DI water. (a) polarization curves corresponding to CMBMCs with different AuNL thickness, clearly indicating the AnNLs can improve the performance, and an optimal thickness is obtained. (b) LSV plots and (c) the corresponding Tafel slopes of CMBMCs. (d) Fitting Plot showing the extraction of C_{dl} for each type of CMBMCs with differences in current density variation ($\Delta J = J_a - J_c$) at the no faradic region (1.25 V). (e) HFR recorded at 3 KHz frequency. (f) Chronopotentilmetry curves of CMBMCs at a constant current density of 1.25 mA/cm^2 for 20 h. 181

Figure 37. Simulation and visualization analysis of CMBMCs with different AuNL thicknesses. (a) Schematic of current and proton transport on the CMBMCs. (b) Proton current or generated electron current distribution along the CMBMCs; the inset of (b) Current density distribution along the CMBMC. Visualization of distribution of OER reaction sites, and current mapping along the CMBMC-0AuNL (c), CMBMC-5AuNL (d), and CMBMC-10AuNL (e). 186

Figure 38. Electrochemical performance of CMBMCs with different IrO_2 loading. (a) polarization curves corresponding to CMBMCs with printed layers range from 0-20, clearly showing a low catalyst loading can achieve good performance. (b) Tafel slopes of CMBMCs extracted from IR-correction LSV plots. (c) HFR recorded at 3 KHz frequency. (d) Chronopotentilmetry curves of CMBMCs at a constant current density of 1.25 mA/cm^2 for 18 h. 190

Figure 39. (a) Schematic of the novel PEMEC with coplanar electrodes. (b) schematic of the cross-section of the coplanar electrodes..... 198

Figure 40. Cyclic voltammetrys (CVs) of CMBMCs with 0 (a), 3 (b), 5 (c), 10 (d), 112 (e), and 197 nm (f) scanned from 0.9 V to 1.0 V at different scan rate. 199

Figure 41. Circuit of the electronic resistance on the CL and the protonic resistance on proton membrane 200

Figure 42. Visualization of OER on CMBMC-3AuNL..... 201

Figure 43. LSV of CMBMCs with different loading..... 201

CHAPTER I

INTRODUCTION

1.1 Overview

Today, the world's population is over seven billion and is continuing to increase, which will result in more than doubled energy consumptions[1, 2]. So far, primary energy resources rely on the non-renewable fuels, such as coal, natural gas, and petroleum [3]. Those fossil fuels release hazard products and will be exhausted eventually [4-10]. Therefore, clean renewable energy resources, including solar, wind, and tide, were considered as promising alternatives to achieve a sustainable energy infrastructure[11]. But the intermittence of those sources will cause the destabilization of electricity grids, which require an efficient large-scale energy storage solution to bridge the supply and demand[11, 12]. Hydrogen is considered as an environmentally friendly energy storage medium for renewable energies and has attracted extensive attention, since it can provide 2.5 times more energy per unit mass than fossil energy and provide hazard-free products[4-10].

Nowadays, hydrogen is mainly generated by steam reforming of fossil fuels or coal gasification, but those methods can only produce low purity hydrogen with a high concentration of carbonaceous species while also causing toxic gas emissions[1, 8, 13]. Notably, stream reforming still highly depends on fossil fuels and does not help to establish the "carbon-balanced" energy matrix[8]. Splitting water into hydrogen and oxygen though water electrolysis is one of the most convenient methods for hydrogen production [14-19].

It mainly includes alkaline water electrolysis[20], solid oxide electrolysis (SOEC)[21], and proton exchange membrane or polymer electrolyte membrane water electrolysis (PEMWE)[22]. Alkaline water electrolysis is a commercially mature technology with the advantages of low cost and long-term stability. But its low partial load range, low current density and low operation pressure remain issues. SOEC can work at high current density with good partial load range and high gas purity in compact cells. However, its potential for large scale hydrogen production is hampered by the durability in acidic corrosive environments and the high cost of ceramic material[8]. Among those water splitting methods, the PEMWE developed by Russell in 1973 provides a number of advantages: rapid response to the power input, compact system design, higher purity product (up to 99.995%), high operation current density (above 2 A/cm^2), and high operation pressure (up to 350 bar)[7, 17, 23-28]. The reaction for all different water electrolysis methods is the same[8]:

$$2H_2O_{(l)} + \underbrace{474.4\ kJmol^{-1}}_{electricity} + \underbrace{97.2\ kJmol^{-1}}_{heat} \rightarrow 2H_2 + O_2 \quad (1\text{-}1)$$

But the reactions at cathode and anode are different for different methods. For PEMWE in pure water:

Anode reaction:

$$2H_2O \xrightarrow{Catalyst} 4H^+ + O_2 + 4e^- \quad (1\text{-}2)$$

Cathode reaction:

$$4H^+ + 4e^- \xrightarrow{Catalyst} 2H_2 \quad (1\text{-}3)$$

And the proton exchange membrane electrolyzer cell (PEMEC) for PEMWE typically consists of catalyst coated membrane (CCM), bipolar plates (BPs) and liquid/gas diffusion layers (LGDLs), gaskets, current distributors, and end plates at anode and cathode sides, as shown in Figure 1. And a membrane electrode assembly (CCM) include two LGDLs and CCM. So far, the use of H_2 as large-scale energy storage with PEMWE has not been established due to the high cost of PEMEC stacks and high electrical energy cost [29]. Therefore, low-cost and high-efficiency PEMECs are highly desirable to lower the price of hydrogen production.

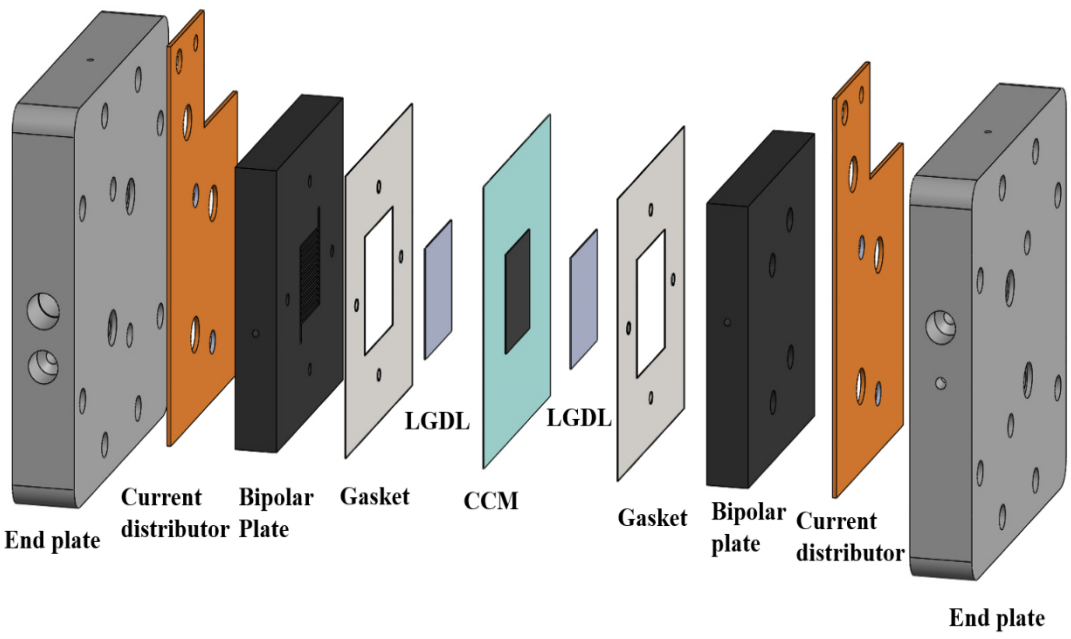

Figure 1. Schematic of a PEMEC.

1.2 Background and literature review

The crucial components in PEMECs include CCM, BP and LGDL, as shown in Figure 2. The CCM is a proton exchange membrane (e.g., Nafion®) coated with two catalyst layers (CLs) for proton/electron transport, oxygen and hydrogen evolution reaction[30, 31]. The LGDLs, mainly made of titanium and carbon fiber, are sandwiched between CLs and BPs, and are expected to function at the minimum voltage, fluidic, and heat losses under a severe electrochemical environment[32, 33]. The BPs, also called flow field plates or separator plates, ensure proper distribution of water and gas, and allow conduction of electrical current through the cell.

At the anode side of PEMECs, the water diffuses from BP to CL through LGDL and then splits into protons, oxygen and electrons (Figure 2). Electrons transport from CL to BP through the LGDL, and protons transport from anode to cathode CL through PEM. At the cathode side, the electrons transport from BP through LGDL to CL and react with protons to form hydrogen. Thus, there is a reducing environment full of hydrogen with a low potential, BPs and LGDLs are seldom corroded[34]. For the anode side, the thermo-neutral voltage of the PEMECs at room temperature is ~1.48 V, while the operating voltage could be over 2.00 V at a high current density and hydrogen-producing rate. And the fluorinated polymer with sulfonic acid side chains in the CCMs will cause a strong acidic environment[29, 35, 36]. Thus, the components in an oxygen rich anodic ambient, where the pH is low and the potential is high, will be easily corroded or oxidized to form oxide layers.

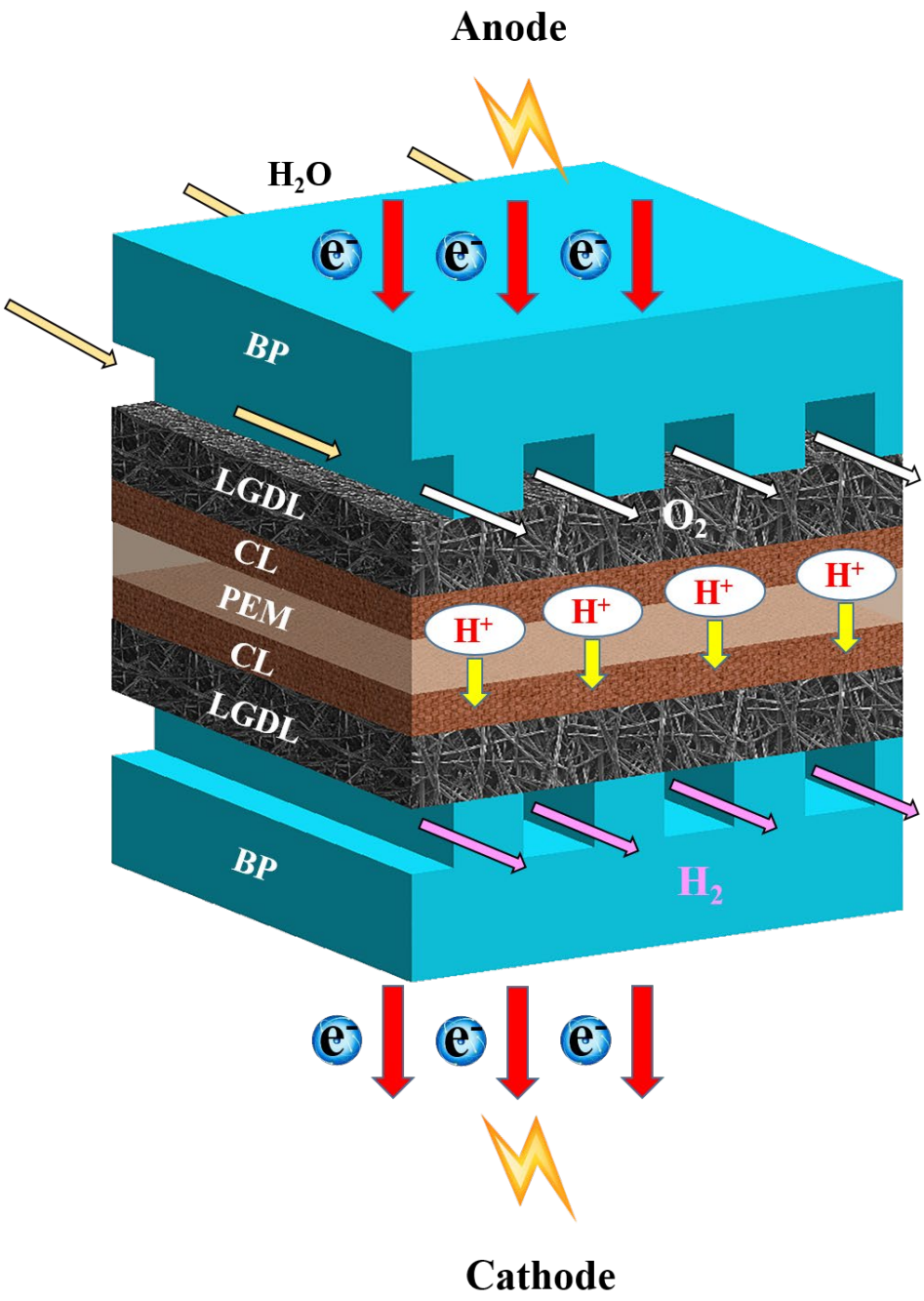

Figure 2. Mass, proton and electron transport path in PEMECs.

BPs usually account for up to 50% of the cost and 60% of the weight of PEMECs [8, 34, 37, 38]. For an electrolyzer with13 kg/day hydrogen production, the stacks account for over half the capital cost, and the BPs represent 48% of the stack cost. For BP manufacturing in large batches, the cost of labor, tooling and machining is almost the same as the material fee, and is even greater in small batches [39]. BPs are typically manufactured from bulk graphite, stainless steel (SS) and Ti [40-42]. SS is considered to be a low-cost material for PEMECs compared with Ti; it has both good mechanical properties and electrical conductivity compared with graphite, but anodic corrosion is problematic [37, 43, 44]. Thus, the cost/time-effective design, manufacturing, and optimization of plates with complex flow channels remain some of the important challenges for the cost reduction of hydrogen energy devices [8, 45, 46]. With the purpose of reducing the cost of BPs, cheaper materials like aluminum, SS and copper were used, but those materials will be easily corroded at a highly oxidative anode environment as mentioned in the previous part [29, 42].

Another possibility to reduce the hydrogen production cost is to improve the performance and efficiency of PEMECs. In PEMECs, the overall overpotential mainly includes activation and ohmic overpotential at the current range of water electrolysis (0 – 2 A/cm^2); the mass transport overpotential can be neglected[47]. Researchers have reported that an ongoing challenge in PEMECs stack design is to reduce or eliminate interfacial contact resistance (ICR) between components such as BPs, LGDLs, CLs, and CDs, in order to reduce the ohmic overpotential and increase the efficiency and performance of stacks

[48-50]. ICR is of great importance for the performance of PEMECs or PEMFCs, and the target of US Department of Energy is 20 $m\Omega \cdot cm^2$ [40, 42, 51]. A higher ICR will lead to a faster increase in working voltage with the increment of working current density, and the efficiency will be reduced [10]. When the aforementioned cheap metal materials are used in PEMECs, the corrosions at acidic environment in PEMECs can not only lead to the damage of the plate structure but can also result in the increase of ICR and contamination of the CCMs, especially for SS materials [8, 40, 52-54]. For instance, SS typically contains Cr, which will be oxidized into a passive layer of Cr_2O_3, particularly at the anode of PEMECs. Then the passive layer will lead to a higher interfacial contact resistance (ICR). Several strategies have been proposed to solve this problem by coating precious metal (Pt, Au et. al) and abundant metal (Ti, Ni, et. al) on the surface of BPs and LGDLs[8, 29, 34]. The coating layers can modify the surface morphology, diminish the ICR between mating parts, and increase the lifetime of BPs [34, 55, 56]. But these coatings increase the cost of PEMECs because of complex deposition processes and expensive materials. Kang et. al developed a novel titanium thin/tunable liquid/gas diffusion layer (TT-LGDL), which also resulted in the reduction of the ohmic and activation losses during water electrolysis [56, 57]. Besides, when cells are scaled up to stacks, assembling the large number of components is very time intensive and requires exacting control. Therefore, simplifying the components design and configuration in PEMECs with low cost and high efficiency is desired.

Researchers are also working on reducing the activation overpotential by developing novel electro-catalysts. The oxygen evolution reaction (OER) at anode in water splitting is a four-electron/four-proton coupled reaction, which requires a higher overpotential, and its slow kinetics greatly limit the hydrogen production [3, 58-60]. At the moment the widely used commercial OER catalysts are still made of precious metals, including Ir and Ru, which provide good OER catalytic activity and stability [3, 59, 61, 62]. Nevertheless, their wide applications for hydrogen economy are limited by the scarcities and the associated high cost. So far, breakthroughs have been made regarding the discovery of perovskites[63], Co, Mo[64], Ni[65] and Fe[60] as the catalyst alternative, which can break the limitation of scarcity of noble metals, but their performances, such as the activation kinetics, overpotential, durability, etc. are still not desirable.

For PEMECs, the OER only occurs on the "triple-phase boundaries" (TPBs), where the electrolyte, water, and electrically connected catalyst are in contact [66, 67]. Furthermore, the in-plane ohmic resistivity of the CL is extremely large (~1000 times) compared to PtB CL for hydrogen evolution reaction (HER) and metal layers, which limit the electrochemical reaction locations to only in 1D sites (at the edge of LGDL), and leads to a waste of the middle regions of the CL and a higher activation overpotential [12, 67]. The 1-dimensional (1D) reaction sites need to be enlarged to 2D in order to increase the volumetric catalyst activity and reduce the cost. Carbon based materials (graphene and carbon nanotubes (CNTs), carbon paper), Ti based particles, and Sn based and W based materials were used as support for catalyst, but most research focused on enhancing the

support–electrocatalyst interaction[25, 68]. Moreover, for a conventional electrochemical catalyst testing, the three electrode assemblies with a thin film rotating disk electrode (RDE) are usually employed. The catalyst is mixed with conductive materials such as carbon particles[63], or the RDE is made of glassy carbon[64]. Those conductive electrodes ignored the impact of resistivity of electrode. But during the real catalytic reaction in full cells, the electrical conductivity of catalyst is essential for their electrochemical performance, and cannot be neglected. Following this line of inquiry, it is necessary to develop and investigate conductive catalysts without sacrificing electrochemical activity. To the best of our knowledge, little research has been done to study the electronic and protonic conductivity of CLs.

Additive manufacturing (AM) technology, also called 3-dimensional (3D) printing, is a process to produce 3D parts layer by layer with freeform fabrication from the late 1980s[69-72]. It is an economical and prompt method in aerospace[73], energy conversion devices[19, 32, 74, 75], automotive[76], medical[77] and other industries manufacturing now[78, 79]. AM can produce parts of anfractuous and complex structures, including intricate internal features, lattice structures, and honeycomb structures, with few post-processing and zero raw material waste from 3D CAD model[70, 80]. Due to those advantages, AM has received significant attentions in electrochemical sciences[32, 81]. Cronin et al. tried to print plastic BP, which is coated with Ag and Au, but the voltage reached 2.5 V at 1 A/cm^2 [12]. Mo et al. fabricated LGDL from Ti using electron beam melting (EBM); however, the pore size and the performance were still not good[32].

Several researchers also tried to fabricate BPs for energy devices from carbon and plastic materials with AM. But dimensional shrinkage and structural inaccuracy as a result of curling, and high voltage at certain current densities remain unsolved issues [82-84]. Based on the current processes on PEMECs discussed above, developing low-cost and high-efficiency PEMECs with AM technologies still remains an unexplored area.

1.3 Motivation and objectives

Low-cost and high-efficiency PEMECs are highly desirable to establish a clean and sustainable energy infrastructure, which serves as the motivation of this work to develop AM PEMECs. The main objectives include:

1. Explore the possibility of application of metallic AM on PEMECs
2. Integrate the components of PEMECs into one part with better performance and compact design by using AM technologies
3. Develop bipolar plates with additive manufacturing and protective coating for durable and high-efficiency PEMECs
4. Combine AM non-conductive bipolar plate with thin film liquid/gas diffusion layers for Low-Cost Hydrogen Production
5. Develop conductive mesoporous bi-material catalyst with ultra-high reaction sites and efficiency for OER in PEMECs by using advanced manufacturing methods

References

[1] S. Y. Tee, K. Y. Win, W. S. Teo, L. D. Koh, S. Liu, C. P. Teng*, et al.*, "Recent Progress in Energy-Driven Water Splitting," *Advanced Science,* 2017.

[2] R. Lee, "The outlook for population growth," *Science,* vol. 333, pp. 569-573, 2011.

[3] N.-T. Suen, S.-F. Hung, Q. Quan, N. Zhang, Y.-J. Xu, and H. M. Chen, "Electrocatalysis for the oxygen evolution reaction: recent development and future perspectives," *Chemical Society Reviews,* vol. 46, pp. 337-365, 2017.

[4] J. A. Turner, "Sustainable hydrogen production," *Science,* vol. 305, pp. 972-974, 2004.

[5] B. Pivovar, N. Rustagi, and S. Satyapal, "Hydrogen at Scale (H2@ Scale): Key to a Clean, Economic, and Sustainable Energy System," *The Electrochemical Society Interface,* vol. 27, pp. 47-52, 2018.

[6] K. E. Ayers, C. Capuano, and E. B. Anderson, "Recent advances in cell cost and efficiency for PEM-based water electrolysis," *ECS Transactions,* vol. 41, pp. 15-22, 2012.

[7] V. R. Stamenkovic, D. Strmcnik, P. P. Lopes, and N. M. Markovic, "Energy and fuels from electrochemical interfaces," *Nature Materials,* vol. 16, pp. 57-69, 2017.

[8] M. Carmo, D. L. Fritz, J. Mergel, and D. Stolten, "A comprehensive review on PEM water electrolysis," *International Journal of Hydrogen Energy,* vol. 38, pp. 4901-4934, 2013.

[9] B. Lee, J. Heo, S. Kim, C. Sung, C. Moon, S. Moon*, et al.*, "Economic feasibility studies of high pressure PEM water electrolysis for distributed H 2 refueling stations," *Energy Conversion and Management,* vol. 162, pp. 139-144, 2018.

[10] U. Babic, M. Suermann, F. N. Büchi, L. Gubler, and T. J. Schmidt, "Critical Review—Identifying Critical Gaps for Polymer Electrolyte Water Electrolysis Development," *Journal of The Electrochemical Society,* vol. 164, pp. F387-F399, 2017.

[11] T. Reier, H. N. Nong, D. Teschner, R. Schlögl, and P. Strasser, "Electrocatalytic oxygen evolution reaction in acidic environments–reaction mechanisms and catalysts," *Advanced Energy Materials,* vol. 7, 2017.

[12] X. Lu, W.-L. Yim, B. H. Suryanto, and C. Zhao, "Electrocatalytic oxygen evolution at surface-oxidized multiwall carbon nanotubes," *Journal of the American Chemical Society,* vol. 137, pp. 2901-2907, 2015.

[13] M. Al-Zareer, I. Dincer, and M. A. Rosen, "Analysis and assessment of a hydrogen production plant consisting of coal gasification, thermochemical water decomposition and hydrogen compression systems," *Energy Conversion and Management,* vol. 157, pp. 600-618, 2018.

[14] R. Bhattacharyya, A. Misra, and K. Sandeep, "Photovoltaic solar energy conversion for hydrogen production by alkaline water electrolysis: conceptual design and analysis," *Energy conversion and management,* vol. 133, pp. 1-13, 2017.

[15] M. A. Pellow, C. J. Emmott, C. J. Barnhart, and S. M. Benson, "Hydrogen or batteries for grid storage? A net energy analysis," *Energy & Environmental Science,* vol. 8, pp. 1938-1952, 2015.

[16] G. Nong, Y. Chen, M. Li, and Z. Zhou, "Generation of hydrogen free radicals from water for fuels by electric field induction," *Energy Conversion and Management,* vol. 105, pp. 545-551, 2015.

[17] A. Sternberg and A. Bardow, "Power-to-What?–Environmental assessment of energy storage systems," *Energy & Environmental Science,* vol. 8, pp. 389-400, 2015.

[18] D. Ferrero and M. Santarelli, "Investigation of a novel concept for hydrogen production by PEM water electrolysis integrated with multi-junction solar cells," *Energy Conversion and Management,* vol. 148, pp. 16-29, 2017.

[19] G. Yang, J. Mo, Z. Kang, Y. Dohrmann, F. A. List, J. B. Green*, et al.*, "Fully printed and integrated electrolyzer cells with additive manufacturing for high-efficiency water splitting," *Applied Energy,* vol. 215, pp. 202-210, 2018.

[20] A. Ursua, L. M. Gandia, and P. Sanchis, "Hydrogen production from water electrolysis: current status and future trends," *Proceedings of the IEEE,* vol. 100, pp. 410-426, 2012.

[21] W. Dönitz and E. Erdle, "High-temperature electrolysis of water vapor—status of development and perspectives for application," *International Journal of Hydrogen Energy,* vol. 10, pp. 291-295, 1985.

[22] J. Russell, L. Nuttall, and A. Fickett, "Hydrogen generation by solid polymer electrolyte water electrolysis," *American Chemical Society Division of Fuel Chemistry Preprints,* vol. 18, p. 24e40, 1973.

[23] S. Siracusano, V. Baglio, N. Van Dijk, L. Merlo, and A. S. Aricò, "Enhanced performance and durability of low catalyst loading PEM water electrolyser based on a short-side chain perfluorosulfonic ionomer," *Applied Energy,* vol. 192, pp. 477-489, 2017.

[24] K. E. Ayers, E. B. Anderson, C. Capuano, B. Carter, L. Dalton, G. Hanlon*, et al.*, "Research advances towards low cost, high efficiency PEM electrolysis," *ECS Transactions,* vol. 33, pp. 3-15, 2010.

[25] T. Reier, H. N. Nong, D. Teschner, R. Schlögl, and P. Strasser, "Electrocatalytic Oxygen Evolution Reaction in Acidic Environments–Reaction Mechanisms and Catalysts," *Advanced Energy Materials,* 2016.

[26] J. Yan, T. Shamim, S. Chou, U. Desideri, and H. Li, "Clean, efficient and affordable energy for a sustainable future," ed: Elsevier, 2017.

[27] G. Cinti, A. Baldinelli, A. Di Michele, and U. Desideri, "Integration of Solid Oxide Electrolyzer and Fischer-Tropsch: A sustainable pathway for synthetic fuel," *Applied Energy,* vol. 162, pp. 308-320, 2016.

[28] Z. Pan, Q. Liu, L. Zhang, J. Zhou, C. Zhang, and S. H. Chan, "Experimental and thermodynamic study on the performance of water electrolysis by solid oxide

electrolyzer cells with Nb-doped Co-based perovskite anode," *Applied Energy,* vol. 191, pp. 559-567, 2017.

[29] P. Lettenmeier, R. Wang, R. Abouatallah, B. Saruhan, O. Freitag, P. Gazdzicki*, et al.*, "Low-Cost and Durable Bipolar Plates for Proton Exchange Membrane Electrolyzers," *Scientific Reports,* vol. 7, p. srep44035, 2017.

[30] S. Park, Y. Shao, J. Liu, and Y. Wang, "Oxygen electrocatalysts for water electrolyzers and reversible fuel cells: status and perspective," *Energy & Environmental Science,* vol. 5, pp. 9331-9344, 2012.

[31] I. E. Stephens, J. S. Elias, and Y. Shao-Horn, "The importance of being together," *Science,* vol. 350, pp. 164-165, 2015.

[32] J. Mo, R. R. Dehoff, W. H. Peter, T. J. Toops, J. B. Green, and F.-Y. Zhang, "Additive manufacturing of liquid/gas diffusion layers for low-cost and high-efficiency hydrogen production," *International Journal of Hydrogen Energy,* 2016.

[33] L. Cindrella, A. Kannan, J. Lin, K. Saminathan, Y. Ho, C. Lin*, et al.*, "Gas diffusion layer for proton exchange membrane fuel cells—A review," *Journal of Power Sources,* vol. 194, pp. 146-160, 2009.

[34] A. Gago, S. Ansar, B. Saruhan, U. Schulz, P. Lettenmeier, N. Cañas*, et al.*, "Protective coatings on stainless steel bipolar plates for proton exchange membrane (PEM) electrolysers," *Journal of Power Sources,* vol. 307, pp. 815-825, 2016.

[35] M. Langemann, D. L. Fritz, M. Müller, and D. Stolten, "Validation and characterization of suitable materials for bipolar plates in PEM water electrolysis," *International journal of hydrogen energy,* vol. 40, pp. 11385-11391, 2015.

[36] J. Mo, Z. Kang, G. Yang, S. T. Retterer, D. A. Cullen, T. J. Toops*, et al.*, "Thin liquid/gas diffusion layers for high-efficiency hydrogen production from water splitting," *Applied Energy,* vol. 177, pp. 817-822, 2016.

[37] P. Lettenmeier, R. Wang, R. Abouatallah, F. Burggraf, A. Gago, and K. Friedrich, "Coated Stainless Steel Bipolar Plates for Proton Exchange Membrane Electrolyzers," *Journal of The Electrochemical Society,* vol. 163, pp. F3119-F3124, 2016.

[38] G. Saur, *Wind-to-hydrogen project: electrolyzer capital cost study*: Citeseer, 2008.

[39] C. Minke, T. Hickmann, A. R. dos Santos, U. Kunz, and T. Turek, "Cost and performance prospects for composite bipolar plates in fuel cells and redox flow batteries," *Journal of Power Sources,* vol. 305, pp. 182-190, 2016.

[40] N. De las Heras, E. Roberts, R. Langton, and D. Hodgson, "A review of metal separator plate materials suitable for automotive PEM fuel cells," *Energy & Environmental Science,* vol. 2, pp. 206-214, 2009.

[41] B. C. Steele and A. Heinzel, "Materials for fuel-cell technologies," *Nature,* vol. 414, pp. 345-352, 2001.

[42] H. Tawfik, Y. Hung, and D. Mahajan, "Metal bipolar plates for PEM fuel cell—a review," *Journal of Power Sources,* vol. 163, pp. 755-767, 2007.

[43] R. Tian, "Chromium nitride/Cr coated 316L stainless steel as bipolar plate for proton exchange membrane fuel cell," *Journal of Power Sources,* vol. 196, pp. 1258-1263, 2011.

[44] M. Li, S. Luo, C. Zeng, J. Shen, H. Lin, and C. n. Cao, "Corrosion behavior of TiN coated type 316 stainless steel in simulated PEMFC environments," *Corrosion science,* vol. 46, pp. 1369-1380, 2004.

[45] S. Karimi, N. Fraser, B. Roberts, and F. R. Foulkes, "A review of metallic bipolar plates for proton exchange membrane fuel cells: materials and fabrication methods," *Advances in Materials Science and Engineering,* vol. 2012, 2012.

[46] X. Li and I. Sabir, "Review of bipolar plates in PEM fuel cells: Flow-field designs," *International Journal of Hydrogen Energy,* vol. 30, pp. 359-371, 2005.

[47] R. García-Valverde, N. Espinosa, and A. Urbina, "Simple PEM water electrolyser model and experimental validation," *international journal of hydrogen energy,* vol. 37, pp. 1927-1938, 2012.

[48] S. Siracusano, V. Baglio, A. Di Blasi, N. Briguglio, A. Stassi, R. Ornelas*, et al.*, "Electrochemical characterization of single cell and short stack PEM electrolyzers based on a nanosized IrO 2 anode electrocatalyst," *International journal of hydrogen energy,* vol. 35, pp. 5558-5568, 2010.

[49] P. Millet, D. Dragoe, S. Grigoriev, V. Fateev, and C. Etievant, "GenHyPEM: a research program on PEM water electrolysis supported by the European

Commission," *International Journal of Hydrogen Energy,* vol. 34, pp. 4974-4982, 2009.

[50] P. Liang, D. Qiu, L. Peng, P. Yi, X. Lai, and J. Ni, "Contact resistance prediction of proton exchange membrane fuel cell considering fabrication characteristics of metallic bipolar plates," *Energy Conversion and Management,* vol. 169, pp. 334-344, 2018.

[51] L. Lei, Y. Wang, S. Fang, C. Ren, T. Liu, and F. Chen, "Efficient syngas generation for electricity storage through carbon gasification assisted solid oxide co-electrolysis," *Applied Energy,* vol. 173, pp. 52-58, 2016.

[52] J. Park, H. Oh, T. Ha, Y. I. Lee, and K. Min, "A review of the gas diffusion layer in proton exchange membrane fuel cells: durability and degradation," *Applied Energy,* vol. 155, pp. 866-880, 2015.

[53] C. Wang and Y. Tao, "Coatings for Robust Metal Bipolar Plates," *ECS Transactions,* vol. 64, pp. 909-915, 2014.

[54] H. Wang, M. A. Sweikart, and J. A. Turner, "Stainless steel as bipolar plate material for polymer electrolyte membrane fuel cells," *Journal of Power Sources,* vol. 115, pp. 243-251, 2003.

[55] D. Prasai, J. C. Tuberquia, R. R. Harl, G. K. Jennings, and K. I. Bolotin, "Graphene: corrosion-inhibiting coating," *ACS nano,* vol. 6, pp. 1102-1108, 2012.

[56] Z. Kang, J. Mo, G. Yang, Y. Li, D. A. Talley, S. T. Retterer*, et al.*, "Thin film surface modifications of thin/tunable liquid/gas diffusion layers for high-efficiency

proton exchange membrane electrolyzer cells," *Applied Energy,* vol. 206, pp. 983-990, 2017.

[57] Z. Kang, J. Mo, G. Yang, S. T. Retterer, D. A. Cullen, T. J. Toops*, et al.*, "Investigation of thin/well-tunable liquid/gas diffusion layers exhibiting superior multifunctional performance in low-temperature electrolytic water splitting," *Energy & Environmental Science,* 2017.

[58] X. Yang, H. Li, A.-Y. Lu, S. Min, Z. Idriss, M. N. Hedhili*, et al.*, "Highly acid-durable carbon coated Co 3 O 4 nanoarrays as efficient oxygen evolution electrocatalysts," *Nano Energy,* vol. 25, pp. 42-50, 2016.

[59] O. Diaz-Morales, S. Raaijman, R. Kortlever, P. J. Kooyman, T. Wezendonk, J. Gascon*, et al.*, "Iridium-based double perovskites for efficient water oxidation in acid media," *Nature communications,* vol. 7, p. 12363, 2016.

[60] R. D. Smith, M. S. Prévot, R. D. Fagan, Z. Zhang, P. A. Sedach, M. K. J. Siu*, et al.*, "Photochemical route for accessing amorphous metal oxide materials for water oxidation catalysis," *Science,* p. 1233638, 2013.

[61] Z. W. Seh, J. Kibsgaard, C. F. Dickens, I. Chorkendorff, J. K. Nørskov, and T. F. Jaramillo, "Combining theory and experiment in electrocatalysis: Insights into materials design," *Science,* vol. 355, p. eaad4998, 2017.

[62] C. C. McCrory, S. Jung, J. C. Peters, and T. F. Jaramillo, "Benchmarking heterogeneous electrocatalysts for the oxygen evolution reaction," *Journal of the American Chemical Society,* vol. 135, pp. 16977-16987, 2013.

[63] Y. Zhu, W. Zhou, Y. Zhong, Y. Bu, X. Chen, Q. Zhong, *et al.*, "A Perovskite Nanorod as Bifunctional Electrocatalyst for Overall Water Splitting," *Advanced Energy Materials,* vol. 7, 2017.

[64] H. Li, S. Chen, X. Jia, B. Xu, H. Lin, H. Yang, *et al.*, "Amorphous nickel-cobalt complexes hybridized with 1T-phase molybdenum disulfide via hydrazine-induced phase transformation for water splitting," *Nature Communications,* vol. 8, 2017.

[65] S. Zhao, Y. Wang, J. Dong, C.-T. He, H. Yin, P. An, *et al.*, "Ultrathin metal–organic framework nanosheets for electrocatalytic oxygen evolution," *Nature Energy,* vol. 1, p. 16184, 2016.

[66] R. O'Hayre and F. B. Prinz, "The air/platinum/nafion triple-phase boundary: characteristics, scaling, and implications for fuel cells," *Journal of The Electrochemical Society,* vol. 151, pp. A756-A762, 2004.

[67] J. Mo, Z. Kang, S. T. Retterer, D. A. Cullen, T. J. Toops, J. B. Green, *et al.*, "Discovery of true electrochemical reactions for ultrahigh catalyst mass activity in water splitting," *Science Advances,* vol. 2, p. e1600690, 2016.

[68] R. I. Jafri, N. Rajalakshmi, and S. Ramaprabhu, "Nitrogen doped graphene nanoplatelets as catalyst support for oxygen reduction reaction in proton exchange membrane fuel cell," *Journal of Materials Chemistry,* vol. 20, pp. 7114-7117, 2010.

[69] G. Tapia and A. Elwany, "A review on process monitoring and control in metal-based additive manufacturing," *Journal of Manufacturing Science and Engineering,* vol. 136, p. 060801, 2014.

[70] G. N. Levy, R. Schindel, and J.-P. Kruth, "Rapid manufacturing and rapid tooling with layer manufacturing (LM) technologies, state of the art and future perspectives," *CIRP Annals-Manufacturing Technology,* vol. 52, pp. 589-609, 2003.

[71] E. C. Santos, M. Shiomi, K. Osakada, and T. Laoui, "Rapid manufacturing of metal components by laser forming," *International Journal of Machine Tools and Manufacture,* vol. 46, pp. 1459-1468, 2006.

[72] D. Gu, W. Meiners, K. Wissenbach, and R. Poprawe, "Laser additive manufacturing of metallic components: materials, processes and mechanisms," *International materials reviews,* vol. 57, pp. 133-164, 2012.

[73] S. Marimuthu, D. Clark, J. Allen, A. Kamara, P. Mativenga, L. Li*, et al.*, "Finite element modelling of substrate thermal distortion in direct laser additive manufacture of an aero-engine component," *Proceedings of the Institution of Mechanical Engineers, Part C: Journal of Mechanical Engineering Science,* vol. 227, pp. 1987-1999, 2013.

[74] G. Yang, J. Mo, Z. Kang, F. A. List, J. B. Green, S. S. Babu*, et al.*, "Additive manufactured bipolar plate for high-efficiency hydrogen production in proton exchange membrane electrolyzer cells," *International Journal of Hydrogen Energy,* vol. 42, pp. 14734-14740, 2017.

[75] G. Yang, S. Yu, J. Mo, Z. Kang, Y. Dohrmann, F. A. List*, et al.*, "Bipolar plate development with additive manufacturing and protective coating for durable and

high-efficiency hydrogen production," *Journal of Power Sources,* vol. 396, pp. 590-598, 2018.

[76] L. J. Love, "Utility of big area additive manufacturing (BAAM) for the rapid manufacture of customized electric vehicles," Oak Ridge National Laboratory (ORNL); Manufacturing Demonstration Facility (MDF)2015.

[77] B. Mueller, "Additive manufacturing technologies–Rapid prototyping to direct digital manufacturing," *Assembly Automation,* vol. 32, 2012.

[78] G. Yang, J. Mo, Z. Kang, Y. Dohrmann, F.-Y. Zhang, S. Eilbeigi*, et al.*, "Additive manufactured micro-sensor from silver nanoparticles for measuring shear stress and pressure," in *Nano/Micro Engineered and Molecular Systems (NEMS), 2017 IEEE 12th International Conference on*, 2017, pp. 164-168.

[79] Q. Yang, J. Y. Andrew, J. Simonton, G. Yang, Y. Dohrmann, Z. Kang*, et al.*, "An inkjet-printed capacitive sensor for water level or quality monitoring: investigated theoretically and experimentally," *Journal of Materials Chemistry A,* vol. 5, pp. 17841-17847, 2017.

[80] K. V. Wong and A. Hernandez, "A review of additive manufacturing," *ISRN Mechanical Engineering,* vol. 2012, 2012.

[81] W. E. Frazier, "Metal additive manufacturing: a review," *Journal of Materials Engineering and Performance,* vol. 23, pp. 1917-1928, 2014.

[82] K. Alayavalli and D. L. Bourell, "Fabrication of modified graphite bipolar plates by indirect selective laser sintering (SLS) for direct methanol fuel cells," *Rapid prototyping journal,* vol. 16, pp. 268-274, 2010.

[83] G. Chisholm, P. J. Kitson, N. D. Kirkaldy, L. G. Bloor, and L. Cronin, "3D printed flow plates for the electrolysis of water: an economic and adaptable approach to device manufacture," *Energy & Environmental Science,* vol. 7, pp. 3026-3032, 2014.

[84] J. R. Hudkins, D. G. Wheeler, B. Peña, and C. P. Berlinguette, "Rapid prototyping of electrolyzer flow field plates," *Energy & Environmental Science,* 2016.

CHAPTER II

ADDITIVE MANUFACTURED BIPOLAR PLATE FOR HIGH-EFFICIENCY HYDROGEN PRODUCTION IN PROTON EXCHANGE MEMBRANE ELECTROLYZER CELLS

A version of this chapter was originally published by Gaoqiang Yang:

Gaoqiang Yang, Jingke Mo, Zhenye Kang, Frederick A. List, Johney B. Green, Sudarsanam S. Babu, and Feng-Yuan Zhang. "Additive manufactured bipolar plate for high-efficiency hydrogen production in proton exchange membrane electrolyzer cells." *International Journal of Hydrogen Energy* 42, no. 21 (2017): 14734-14740.

I am fully responsible for the work submitted in these publications.

2.1 Abstract

Additive manufacturing (AM) technology is capable of fast and low-cost prototyping from complex 3D digital models. To take advantage of this technology, a stainless steel (SS) plate with parallel flow field served as a combination of a cathode bipolar plate and a current distributor; it was fabricated using selective laser melting (SLM) techniques and investigated in a proton exchange membrane electrolyzer cell (PEMEC) in-situ for the first time. The experimental results show that the PEMEC with an AM SS cathode bipolar plate can achieve an excellent performance for hydrogen production for a voltage of 1.779 V and a current density of 2.0 A/cm^2. The AM SS cathode bipolar plate was also characterized by SEM and EDS, and the results show a uniform elemental distribution across the plate with very limited oxidization. This research demonstrates that AM method could be a route to aid cost-effective and rapid development of PEMECs.

2.2 Introduction

Hydrogen is playing an increasingly crucial role as an energy carrier in the near future economy, due to its high energy density and environment-friendly product [1-7]. However, more than 90% of the world's hydrogen is produced from fossil fuels, including petroleum and coal, which would lead to the increase of greenhouse gases [8]. Water electrolysis is considered an efficient and promising alternative to the conventional reformulation method for hydrogen production, and proton exchange membrane electrolyzer cells (PEMECs) offer a number of advantages for this process including higher purity of hydrogen, high working current, capability of producing compressed gases (>200 bar) for direct using or storage, quick response to current change, and easy maintenance[1, 9-13]. Due to these advantages, PEMECs have attracted significant attention for electrolysis of water recently.

However, there are several key challenges for the wide commercialization of PEMECs, including cost, performance, and durability [3, 14, 15]. Bipolar plates with flow channels, which distribute the reactants/products and conduct the current, are indispensable components in PEMECs. It has been estimated that the bipolar plates account for 40%-51% of the overall cost of the PEMECs [16-18]. The electric contact resistance between the bipolar plates and current distributors also contributes to the overall performance of the cells [19]. And the time required for designing/manufacturing new bipolar plates with complex flow channels is another challenge for PEMECs, due to the difficulty of managing the mass transport through the bipolar plate[20, 21]. Furthermore, the mechanical properties, weight and volume of bipolar plates are also influenced by the manufacturing

process. Thus, the development of low-mass, cost-effective bipolar plates s has been desired focus for PEMECs.

Additive manufacturing is an emerging manufacturing technology, which can rapidly produce items with anfractuous and complex structures, such as intricate internal features (lattice structures and honeycomb structures), with little post-processing and nearly zero raw material waste from 3D CAD models [4, 22]. For some special remote locations, including aircraft carriers, submarines and space stations, AM offers the option for site-made components. The nature of AM allows fast fabrication of lighter weight, lower cost PEMECs for future developments. Due to its relatively low cost and moderate mechanical strength, stainless steel (SS) is considered an alternative to other materials, such as titanium and graphite in PEMFC/EC applications [23]. For SS bipolar plates at the anode side of a PEMEC, a high corrosion-resistant protective layer may need to be applied by chemical vapor deposition, physical vapor deposition, or chemical and electrochemical techniques due to the harsh environment; possible coatings for this application include Au, Au/Ni, TiN, Ti/Pt, SnO_2, and CrN[15, 24-26]. Researchers have shown that the corrosion of untreated SS bipolar plate at the cathode side is much less intense than that at the anode side, so it is suitable to use SS at cathode side [12, 25]. In this paper, the SLM approach was used to co-manufacture the bipolar plate and current distributor as a single part with SS 316L. Both in-situ and ex-situ investigations of the AM metallic bipolar plates in PEMECs were performed. Uniform element distributions of AM metallic components and

excellent PEMEC performances demonstrated the AM technique could be used as an alternative, low-cost, and rapid approach for PEMEC developments.

2.3 Experimental details

The AM SS plate was designed by SolidWorks 2016 software, and the design was exported as a .STL file. The resulting model was sliced and processed for building by Materialise Magics 20. A Renishaw AM250 laser powder bed printer was used to fabricate the cathode bipolar plate with the SLM technique. And the schematic of the SLM technique is shown in Figure 3a, the roller carried SS powders from the powder delivery system to form a powder bed at the platform, and the laser selectively melted the powder. This process was repeated layer-by-layer until the bipolar plate was completed. The spherical 316L powder used for the build was supplied by Renishaw and had a size range of 15-45 μm diameter. The specified elemental composition of the powder, as shown in Figure 5, is 18 wt.% Cr, 12.9 wt.% Ni, 2.4 wt.% Mo, 1.45 wt.% Mn, 0.75 wt.% Si, 0.1 wt.% Cu, 0.1 wt.% N, 0.04 wt. % O, 0.03 wt.% C, 0.02 wt.% P, 0.009 wt. %S, balance Fe. The surface of additive manufactured plates was rough due to the printing trace and the melt pool. In order to accomplish a better plate performance, the plate was mechanically polished with different grades of grinding papers (SiC grindings paper #250-1200, BUEHLER).

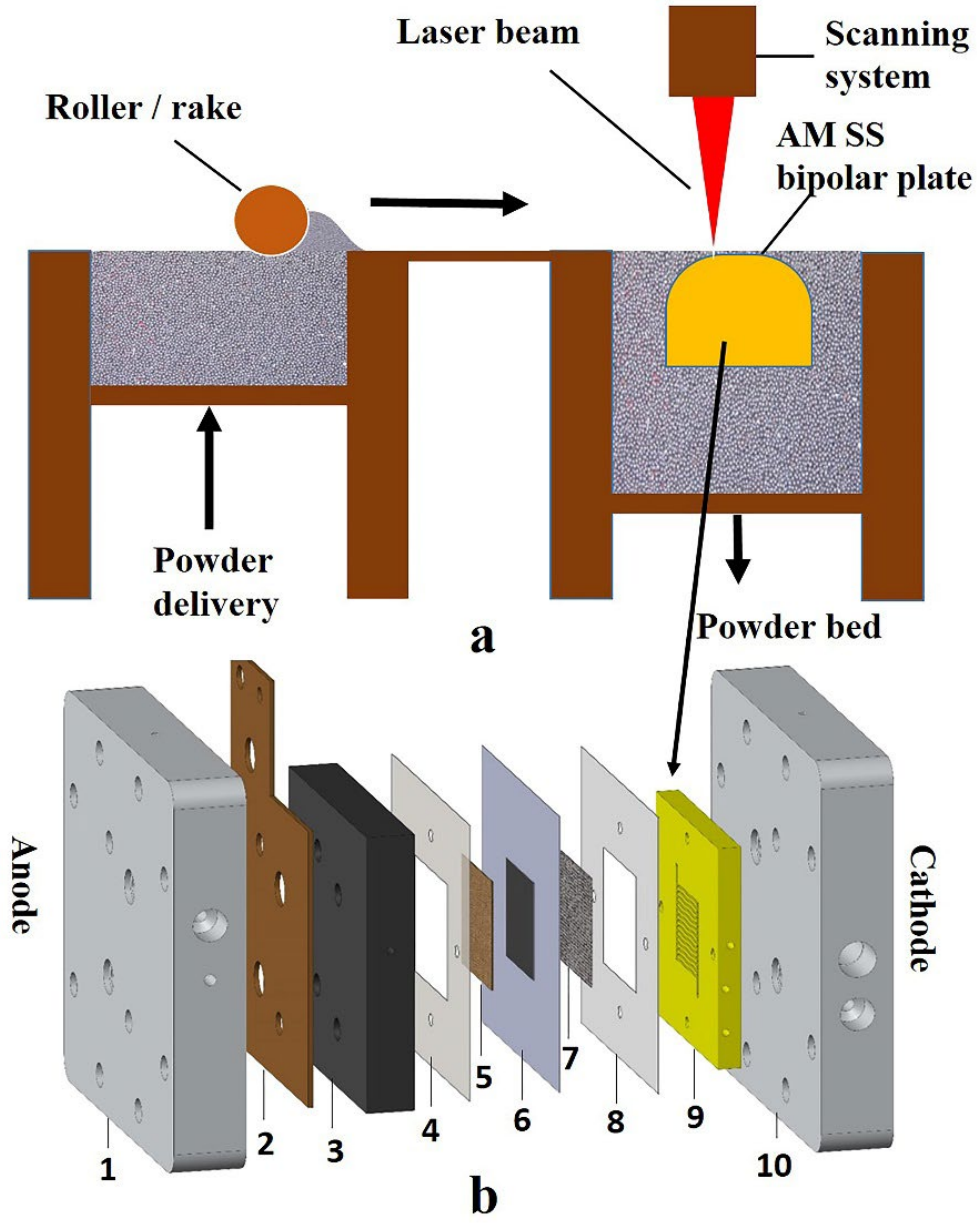

Figure 3. (a). Schematic of SLM technology. (b) Configuration of AM PEMEC, 1- anode end plate, 2- anode current distributor, 3- graphite bipolar plate, 4- anode gasket, 5- Ti felt LGDL, 6- CCM, 7- carbon paper LGDL, 8- cathode gasket, 9- AM SS bipolar plate, 10- cathode end plate.

The AM SS bipolar plate was characterized by Scanning Electron Microscopy (SEM) and Energy Dispersive Spectrometry (EDS). The surface morphologies of the bipolar plate before and after polishing were identified by using a field emission SEM JEOL JSM-6320F with an accelerating voltage of 0.5 – 30 kV, a magnification of 130 x~650,000 x and a 5-axis specimen mount. The element distribution spectrum was recorded by the EDS detector. The EDS detector is an EDAX Octane plus Silicon Drift Detector that works in tandem with EDAX's TEAM EDS software analysis system.

The configuration of the AM PEMEC in this study is shown in Figure 3(b). A commercial catalyst coated membrane (CCM) from FuelCellsEtc contains a Nafion® 115 membrane, 3.0 mg/cm^2 $IrRuO_x$ - Iridium Ruthenium Oxide loading at the anode and 3.0 mg/cm^2 Pt - Platinum Black loading at the cathode with an active area of 5 cm^2. The AM SS bipolar plate served as the cathode bipolar plate and distributor, the anode bipolar plate was machined from a graphite plate, and a copper plate functioned as a current distributor that was incorporated into the cell between anode bipolar plate and end plate. Titanium felt (GDL7, Bekaert Corporation) with thickness of 0.35 mm and porosity of 75% and carbon paper (Toray 090) with thickness of 0.28 mm and porosity of 78% were used as anode and cathode LGDLs, respectively. There are PVC gaskets between bipolar plates and CCM. The cell was compressed by eight evenly distributed bolts (thread is ¼-20 SS insert) with 4.52 N·m of torque. Tests were controlled and characterized by a potentiostat SP-300 chassis with a 5 V/10 A booster from Bio-Logic to get polarization curves and electrochemical impedance spectroscopy (EIS). Deionized water was supplied to the anode

by a diaphragm liquid pump from KNF Neuberger with a flow rate of 20 ml/min, and was preheated by a water bath from Polyscience. Two heaters and two thermocouples connected to a Multi-Zone controller from OMEGA were used to control the cell temperature. The cell was evaluated at temperatures of 20, 40, 60 and 80 °C and a pressure of 1 atm.

2.4 Results and discussion

Figure 4 shows the photographic and SEM images of the AM cathode bipolar plate before and after polishing. All SEM images of the land edge of the flow channel were taken with 200 μm scale bar. Figure 4a and Figure 4c show the land edge of flow channel and whole area of the AM cathode bipolar plate before polishing, respectively. Without polishing, the plate surface is rough, and the printing track, shape of melt pool on the land of the flow channel, and SS powders at the side walls of the land can be seen clearly in the SEM image. Figure 4b and d show the land edge of flow channel and whole area of the AM cathode bipolar plate after polishing and ultrasonic cleaning, respectively. The polished land is smooth, and most of the SS powder is removed.

The weight of the polished AM SS plate is 147.5g, which is much lighter than that of the conventional graphite plate and copper current distributor, 265.5g. The volume of the plate is 5.4 × 60.7 × 60.7 mm, whereas the total volume of conventional graphite plate and copper current distributor is 21.0 × 76.2 × 76.2 mm.

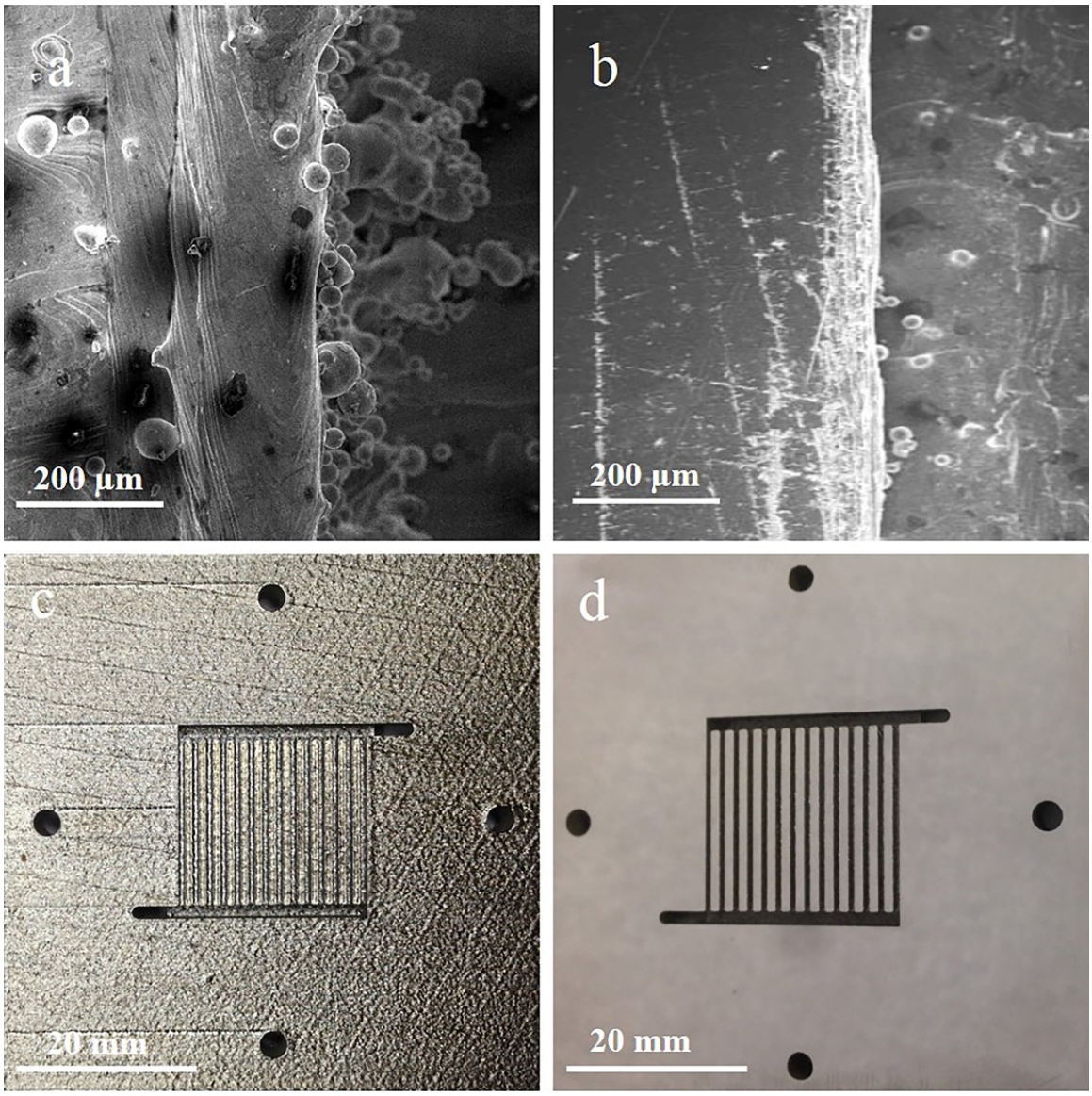

Figure 4. Photographic and SEM images of the AM cathode bipolar plate before and after polishing. (a) SEM image of land before polishing. (b) SEM image of land after polishing. (c) Photo before polishing. (d) Photo after polishing.

Those points are of importance when large numbers of plates are stacked. Although the active area of this AM PEMEC is only 5 cm^2, areas up to nearly 0.3 m^2 can be presently achieved for a single plate with even larger areas possible as the AM technology develops.

The EDS analyses of the AM cathode bipolar plate, as shown in Figure 5, indicate that the weight percentages of the elements deviate only slightly from the specification of raw material after the additive manufacturing process. Studies of SS 316L parts processed by SLM show that the strength properties of these AM parts can be better than those of the wrought products, which is attributed to the additive manufacturing process and changes in microstructures and elemental compositions [27]. EDS results for different spots on the plate surface indicate that the distribution of elements on the AM cathode bipolar plate is uniform. The change of mechanical properties of the AM cathode bipolar plate may have an impact on the performance of the cell as well, and will be investigated in our future studies.

Polarization curves are to evaluate the performance of a PEMEC, and they show the change of the sum of different polarization losses as function of current density. Polarization curves are drawn by recording the cell voltage respected to current density changing from 0 to 2.0 A/cm^2 for a step rate of 10 mA/s, and are compared at different temperatures of 20, 40, 60 and 80 °C, as shown in Figure 6a. The cell voltage gradually decreases as the temperature increasing, and the performances under the current density of 2.0 A/cm^2 are 2.081 V, 1.935 V and 1.850 V at 20 °C, 40 °C and 60 °C, respectively. The best performance the cell achieves is 1.779V at 80 °C.

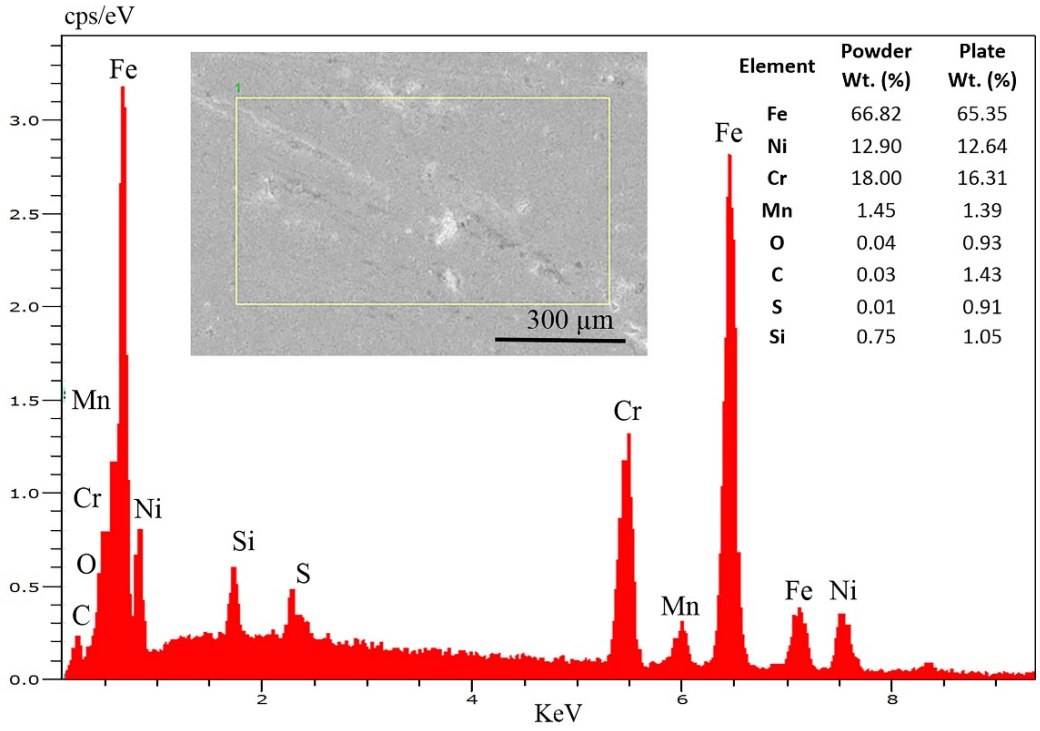

Figure 5. EDS spectrum of AM SS 316L cathode bipolar plate.

These results indicate that the better performance of the cell can be achieved at higher temperature, because the higher temperature could benefit the kinetics and interfacial contacts between each parts, strengthen the proton transportation through the Nafion® membrane, and enhance the mass transportation of the reactants and products [4, 28, 29].

From the literature [11], the voltage of the conventional PEMEC with graphite bipolar plates at both the anode and the cathode sides is 1.880 V under the same operating conditions of 80 °C and 2 A/cm^2, while that of PEM electrolyzer with AM SS cathode bipolar plate is 1.779 V.

The PEMEC efficiency (η) is determined using the following equation (1):

$$\eta = \frac{V_{thermal}}{V_{PEMEC}} \quad (2\text{-}1)$$

Where $V_{thermal}$ and V_{PEMEC} are the thermoneutral voltage and voltage of PEMECs, respectively, and $V_{thermal}$ is about 1.484 V under normal operating conditions [11, 30]. Based on this calculation, the PEMEC with AM SS cathode bipolar plate provides a significantly higher efficiency (83.4%) compared to the conventional components (78.9%). The improvement might be due to the elimination of contact resistance between the bipolar plate and current distributor at cathode side. The AM SS cathode plate with parallel flow field serves as both cathode bipolar plate and current distributor simultaneously, thus improve the overall performance.

For a better understanding, electrochemical impedance spectroscopy (EIS) was used during testing. The ohmic resistance and the total resistance of the cell are measured from the leftmost and rightmost intersections of the Nyquist EIS curve with X-axis at a high frequency and low frequency, respectively. The EIS measurements are carried out for a current density of 0.2 A/cm^2 at different temperatures for frequencies from 200 kHz to 30 mHz. Figure 6b shows the ohmic resistance reduces significantly while increasing the temperature. The ohmic resistance varies from 0.229 Ω·cm^2 at 20 °C to 0.129 Ω·cm^2 at 80 °C. These data demonstrate a relatively low ohmic resistance with the AM cathode bipolar plate which can improve the performance of PEMECs.

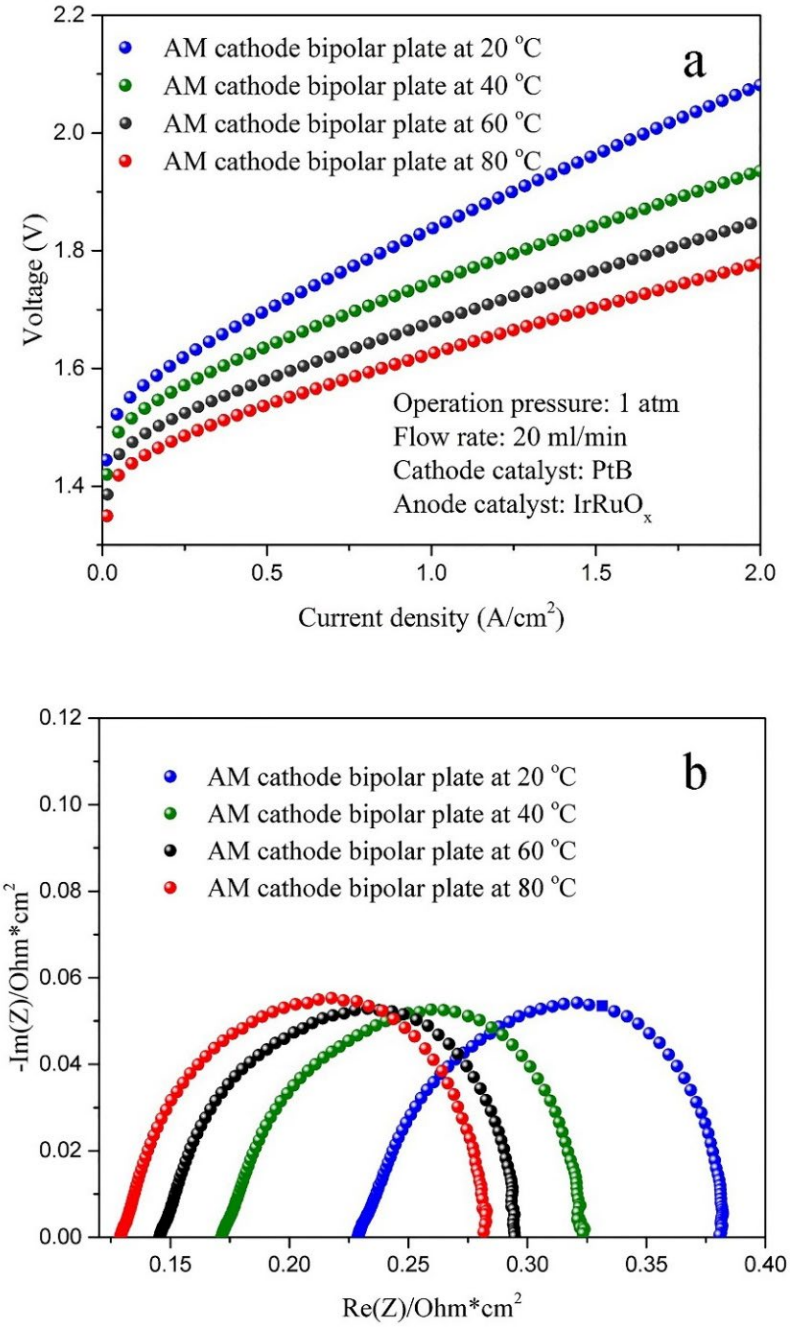

Figure 6. (a). Polarization curves of PEMEC with AM SS cathode bipolar plate at different temperatures. (b). EIS results of PEMECs with AM SS cathode bipolar plates at different temperatures.

The EIS results agree with the performance results from polarization curves of the PEMEC. The changes of ohmic resistances in the EIS are reflected as changes of slope in the polarization curves. The ohmic resistances include ionic resistance of the CCM, electrical resistance of other components, and contact resistance between mating surface [11, 31]. As temperature increases, the proton conductivity of CCMs increases which will reduce the ohmic resistance. The interfacial resistance between mating components decreases at higher temperature due to thermal expansions; components expand with increasing temperature, which in turn leads to higher compression pressure and lower contact resistance. But the electrical resistances of bipolar plate, LGDLs and current distributor remain almost constant within the aforementioned temperature range [7, 10]. For conventional PEMEC with graphite bipolar plates at both sides, the ohmic resistance and total resistance are 0.203 ohm·cm^2 and 0.340 ohm·cm^2, respectively, which are larger than those of AM PEMEC under the same operation conditions of 80 °C and 0.2 A/cm^2. And the reduction of the resistances leads to the better performance for the AM PEMEC than for the conventional PEMEC.

2.4 Summary

In this research, a SS 316L cathode bipolar plate with parallel flow channels is fabricated with the SLM technique, and *in-situ* characterized in a PEMEC for the first time. The experimental results demonstrate the viability of additive manufacturing of prototype metallic cathode bipolar plates for PEMECs starting from a 3-D digital model. Meanwhile, the performance of the cell with a AM SS cathode bipolar plate is excellent, and the

operation voltage can reach 1.779 V at 2.0 A/cm^2. Furthermore, the AM SS cathode bipolar plate is also characterized by SEM and EDS *ex-situ*, and the results show the weight percentages of the elements deviate only slightly from those of the raw powder with very limited oxidization. The elemental distribution is uniform across the plate. This study demonstrates an alternative, low-cost, and rapid approach to develop prototype devices for renewable hydrogen production.

References

[1] M. Carmo, D. L. Fritz, J. Mergel, and D. Stolten, "A comprehensive review on PEM water electrolysis," *International Journal of Hydrogen Energy,* vol. 38, pp. 4901-4934, 2013.

[2] M. D. Symes and L. Cronin, "Decoupling hydrogen and oxygen evolution during electrolytic water splitting using an electron-coupled-proton buffer," *Nature chemistry,* vol. 5, pp. 403-409, 2013.

[3] S. A. Grigoriev, V. I. Porembsky, and V. N. Fateev, "Pure hydrogen production by PEM electrolysis for hydrogen energy," *International Journal of Hydrogen Energy,* vol. 31, pp. 171-175, Feb 2006.

[4] J. Mo, R. R. Dehoff, W. H. Peter, T. J. Toops, J. B. Green, and F.-Y. Zhang, "Additive manufacturing of liquid/gas diffusion layers for low-cost and high-efficiency hydrogen production," *International Journal of Hydrogen Energy,* 2016.

[5] H. Tsuchiya and O. Kobayashi, "Mass production cost of PEM fuel cell by learning curve," *International Journal of Hydrogen Energy,* vol. 29, pp. 985-990, 2004.

[6] L. Ma, S. Sui, and Y. Zhai, "Investigations on high performance proton exchange membrane water electrolyzer," *International Journal of Hydrogen Energy,* vol. 34, pp. 678-684, 2009.

[7] Z. Kang, J. Mo, G. Yang, S. T. Retterer, D. A. Cullen, T. J. Toops*, et al.*, "Investigation of thin/well-tunable liquid/gas diffusion layers exhibiting superior

multifunctional performance in low-temperature electrolytic water splitting," *Energy & Environmental Science,* 2017.

[8] S. J. Davis, K. Caldeira, and H. D. Matthews, "Future CO2 emissions and climate change from existing energy infrastructure," *Science,* vol. 329, pp. 1330-1333, 2010.

[9] G. Chisholm, P. J. Kitson, N. D. Kirkaldy, L. G. Bloor, and L. Cronin, "3D printed flow plates for the electrolysis of water: an economic and adaptable approach to device manufacture," *Energy & Environmental Science,* vol. 7, pp. 3026-3032, 2014.

[10] B. Han, J. Mo, Z. Kang, and F.-Y. Zhang, "Effects of membrane electrode assembly properties on two-phase transport and performance in proton exchange membrane electrolyzer cells," *Electrochimica Acta,* vol. 188, pp. 317-326, 2016.

[11] J. Mo, Z. Kang, G. Yang, S. T. Retterer, D. A. Cullen, T. J. Toops*, et al.*, "Thin liquid/gas diffusion layers for high-efficiency hydrogen production from water splitting," *Applied Energy,* vol. 177, pp. 817-822, 2016.

[12] Ö. F. Selamet, F. Becerikli, M. D. Mat, and Y. Kaplan, "Development and testing of a highly efficient proton exchange membrane (PEM) electrolyzer stack," *International Journal of hydrogen energy,* vol. 36, pp. 11480-11487, 2011.

[13] P. Millet, N. Mbemba, S. Grigoriev, V. Fateev, A. Aukauloo, and C. Etiévant, "Electrochemical performances of PEM water electrolysis cells and perspectives," *International Journal of Hydrogen Energy,* vol. 36, pp. 4134-4142, 2011.

[14] A. T. Marshall, S. Sunde, M. Tsypkin, and R. Tunold, "Performance of a PEM water electrolysis cell using IrxRuyTazO2 electrocatalysts for the oxygen evolution electrode," *International Journal of Hydrogen Energy,* vol. 32, pp. 2320-2324, 2007.

[15] T.-H. Huang, H.-L. Shen, T.-C. Jao, F.-B. Weng, and A. Su, "Ultra-low Pt loading for proton exchange membrane fuel cells by catalyst coating technique with ultrasonic spray coating machine," *international journal of hydrogen energy,* vol. 37, pp. 13872-13879, 2012.

[16] K. E. Ayers, C. Capuano, and E. B. Anderson, "Recent advances in cell cost and efficiency for PEM-based water electrolysis," *ECS Transactions,* vol. 41, pp. 15-22, 2012.

[17] L. Bertuccioli, A. Chan, D. Hart, F. Lehner, B. Madden, and E. Standen, "Study on development of water electrolysis in the EU," *Fuel cells and hydrogen joint undertaking,* vol. 114, 2014.

[18] X. Li and I. Sabir, "Review of bipolar plates in PEM fuel cells: Flow-field designs," *International Journal of Hydrogen Energy,* vol. 30, pp. 359-371, 2005.

[19] R. Hornung and G. Kappelt, "Bipolar plate materials development using Fe-based alloys for solid polymer fuel cells," *Journal of Power Sources,* vol. 72, pp. 20-21, 1998.

[20] I. U. Hwang, H. N. Yu, S. S. Kim, J. Do Suh, S. H. Lee, B. K. Ahn*, et al.*, "Bipolar plate made of carbon fiber epoxy composite for polymer electrolyte membrane fuel cells," *Journal of Power Sources,* vol. 184, pp. 90-94, 2008.

[21] E. Kumbur, K. Sharp, and M. Mench, "Liquid droplet behavior and instability in a polymer electrolyte fuel cell flow channel," *Journal of Power Sources,* vol. 161, pp. 333-345, 2006.

[22] K. V. Wong and A. Hernandez, "A review of additive manufacturing," *ISRN Mechanical Engineering,* vol. 2012, 2012.

[23] A. Gago, S. Ansar, B. Saruhan, U. Schulz, P. Lettenmeier, N. Cañas*, et al.*, "Protective coatings on stainless steel bipolar plates for proton exchange membrane (PEM) electrolysers," *Journal of Power Sources,* vol. 307, pp. 815-825, 2016.

[24] Y.-H. Yun, "Deposition of gold–titanium and gold–nickel coatings on electropolished 316L stainless steel bipolar plates for proton exchange membrane fuel cells," *international journal of hydrogen energy,* vol. 35, pp. 1713-1718, 2010.

[25] J. Mo, S. M. Steen, F.-Y. Zhang, T. J. Toops, M. P. Brady, and J. B. Green, "Electrochemical investigation of stainless steel corrosion in a proton exchange membrane electrolyzer cell," *International Journal of Hydrogen Energy,* vol. 40, pp. 12506-12511, 2015.

[26] M. M. Mench, E. C. Kumbur, and T. N. Veziroglu, *Polymer electrolyte fuel cell degradation*: Academic Press, 2011.

[27] I. Tolosa, F. Garciandía, F. Zubiri, F. Zapirain, and A. Esnaola, "Study of mechanical properties of AISI 316 stainless steel processed by “selective laser melting”, following different manufacturing strategies," *The International Journal of Advanced Manufacturing Technology,* vol. 51, pp. 639-647, 2010.

[28] J. P. Owejan, T. A. Trabold, and M. M. Mench, "Oxygen transport resistance correlated to liquid water saturation in the gas diffusion layer of PEM fuel cells," *International Journal of Heat and Mass Transfer,* vol. 71, pp. 585-592, 2014.

[29] E. Kumbur, K. Sharp, and M. Mench, "On the effectiveness of Leverett approach for describing the water transport in fuel cell diffusion media," *Journal of Power Sources,* vol. 168, pp. 356-368, 2007.

[30] C. M. Hwang, M. Ishida, H. Ito, T. Maeda, A. Nakano, Y. Hasegawa*, et al.*, "Influence of properties of gas diffusion layers on the performance of polymer electrolyte-based unitized reversible fuel cells," *International journal of hydrogen energy,* vol. 36, pp. 1740-1753, 2011.

[31] M. M. Mench, *Fuel cell engines*: John Wiley & Sons, 2008.

CHAPTER III

FULLY PRINTED AND INTEGRATED ELECTROLYZER CELLS WITH ADDITIVE MANUFACTURING FOR HIGH-EFFICIENCY WATER SPLITTING

A version of this chapter was originally published by Gaoqiang Yang:

Yang, Gaoqiang, Jingke Mo, Zhenye Kang, Yeshi Dohrmann, Frederick A. List, Johney B. Green, Sudarsanam S. Babu, and Feng-Yuan Zhang. "Fully printed and integrated electrolyzer cells with additive manufacturing for high-efficiency water splitting." *Applied Energy* 215 (2018): 202-210.

I am fully responsible for the work submitted in these publications.

3.1 Graphical Abstract

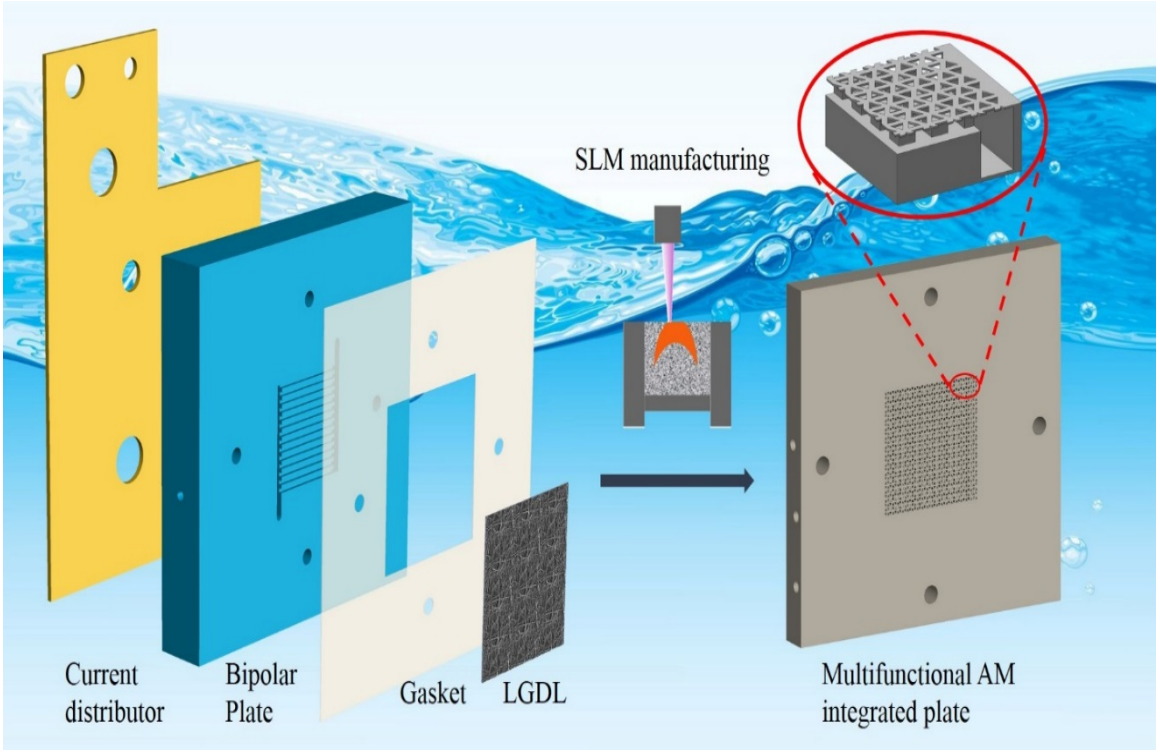

3.2 Abstract

Using additive manufacturing (AM) technology, a fundamental material and structure innovation was proposed to significantly increase the energy efficiency and to reduce the weight, volume and component number of proton exchange membrane electrolyzer cells (PEMECs). Four conventional parts (liquid/gas diffusion layer, bipolar plate, gasket, and current distributor) in a PEMEC were integrated into one multifunctional AM plate without committing to tools or molds for the first time. In addition, since the interfacial contact resistances between those parts were eliminated, the comprehensive *in-situ* characterizations of AM cells show an excellent energy efficiency of up to 86.48 % is achieved at 2 A/cm^2 and 80 ºC, and the hydrogen generation rate is increased by 61.81% compared to the conventional cell. More importantly, the highly complex inner structures of the AM integrated multifunctional plates also exhibit the potential to break limitations of conventional manufacture methods for hydrogen generation and to open a door for the development of other energy conversion devices, including fuel cells, solar cells and batteries.

3.3 Highlights

- Integrated electrolyzer cells with complex inner structure were fully printed with additive manufacturing.
- Four components in PEMECs were integrated into one part.
- An ultralow electrical resistance of electrodes was achieved.

- AM PEMECs provide an energy efficiency of up to 86.48 % at 2 A/cm^2 and 80 ^{o}C.
- AM PEMECs open a door for developing other energy conversion devices.

3.4 Introduction

Hydrogen is considered as one of the best vectors/carriers for storing renewable and intermittent energy from sources including wind and solar, or off-peak energy from the grid[1-9]. Water electrolysers, especially proton exchange membrane electrolyzer cells (PEMECs), provide a sustainable method for producing hydrogen from water splitting with rapid response to the power input, higher purity product (up to 99.995%), high operation current density (above 2 A/cm^2), and high operation pressure (up to 350 bar)[4, 10-16]. A PEMEC typically consists of a catalyst-coated membrane (CCM), sandwiched by two liquid/gas diffusion layers (LGDLs), two bipolar plates (BPs), two gaskets, and two current distributors at anode and cathode sides. Nevertheless, the relatively low efficiency and high complexity have retarded its wider commercialization [3, 12, 17, 18] .

To reduce the cost and promote performance of PEMECs, some efforts are focusing on reducing the use of the precious catalysts (e.g., Pt and Ir), or exploring the alternatives, such as Fe, Co, Cu, Ni, Mo, and W-based nonprecious catalysts, while another approach is to optimize other components and the whole system[11, 19-21]. BPs and LGDLs significantly affect the performance of PEMECs especially at the high current density, where the ohmic overpotential and concentration overpotential become the dominant factors for total cell voltage[22, 23]. BPs usually account for 30% - 48% of the cost and 60% of the weight of PEMECs [3, 24]. The cost of labor, tooling, and machining for large-

volume BP manufacturing is almost the same as that of the materials, and the cost even become much higher for small batches[25]. Furthermore, the LGDLs are expected to simultaneously transport electrons, reactants and products at minimum voltage, fluidic, and heat losses in a severe electrochemical environment, and they mainly made of titanium and carbon by using weaving, sintering or etching processes. But the woven and sintered felt LGDLs will result in nonuniform interfacial contacts and random pore morpohologies. And the etching method involves several complicated processes, and the chemical and disposal costs will limit its application [3, 26, 27].

Researchers have recently reported to improve the PEMEC performance by reducing or eliminating contact resistances between mating components such as the BPs, LGDLs, CLs, and current distributors[28, 29]. Several strategies have been proposed to solve this problem, by coating precious metals (Pt, Au, etc.) and abundant metals (Ti, Ni, etc.) on the surface of BPs and LGDLs[30, 31], or by optimizing the components properties and structures[32, 33]. Coatings increase the cost of PEMECs because of the complex chemical processes and expensive materials. Structures and morphologies of BPs and LGDLs are optimized by changing the channel shape and the pore size [3, 32, 34, 35]. But the interfacial contact resistance has not been eliminated, and the optimization of PEMEC materials and structures for better performance reaches a bottleneck. Furthermore, when cells are scaled up to stacks, assembling the large number of components is very time intensive, and requires exacting control. Therefore, simplifying the components design and

configuration with low cost and high efficiency remains an important challenge for the commercial application of PEM energy devices.

Additive manufacturing (AM) technology, also called rapid prototyping, freeform fabrication, or 3D printing, allows material to "print" three-dimensionally from three-dimensional (3D) digital models instead of cutting materials from an initial bulk[36, 37]. Due to its potential to offer cost and time-efficient parts with complex 3D structure, AM has received significant attention in electrochemical sciences. Cronin et al. tried to print a plastic BP, which was coated with Ag and Au, but the voltage in the PEMEC reached 2.5 V at 1 A/cm^2[38]. Mo et al. fabricated LGDLs from Ti using electron beam melting (EBM), however the performance was not good compared with conventional PEMECs[26]. Several researchers also tried to fabricated BPs for energy devices from carbon and plastic materials with AM, but dimensional shrinkage and structure inaccuracy as a result of curling and high voltage at certain current density remain unresolved issues[18, 38, 39]. Nevertheless, none of those efforts has been devoted to integrate components in the energy devices into one part, and the devices' performances in those publications are not comparable to that of conventional one. Therefore, the integration of different parts for low-cost and high-efficiency water electrolyzers is unexplored and highly desired.

Herein, one of the AM technologies, selective laser melting (SLM), is used to meet the aforementioned challenges, and to develop novel multifunctional AM integrated plates that serve as BPs, LGDLs, gaskets and current distributors simultaneously, shown in Figure 7. Both ex-situ and in-situ characterizations of the AM integrated plates are comprehensively

conducted, and the equivalent electrochemical circuits (EECs) are introduced to quantify the AM plates for PEMEC performance. The integration of several conventional components into one multifunctional AM part not only significantly improves the performance of PEMECs with lower resistances, but also greatly simplify the configuration and reduce the weight and volume. The study also indicates AM can accomplish radical structure changes for electrolyzer and other energy conversion devices.

3.5 Experimental

3.5.1 Fabrication of AM plates

Using AM technology, the conventional BP, LGDL, gasket, and current distributor were integrated into one part, as shown in Figure 7. The patterns of AM SS plates were designed using SOLIDWORKS 2016, then solid models were sliced and converted for building using Materialise Magics 20. A Renishaw AM250 laser powder bed printer was employed to build the plates. Parameters during manufacturing included laser power of 200 W, focus offset of 0 mm, layer thickness of 50 μm, point spacing of 60 μm, exposure time of 80 μs, hatch spacing of 110 μm, average beam velocity of 0.64 m/s, and a stripe melting mode of 5 mm. Three printed plates: AM plate with parallel flow channel, AM plate with pin flow channel, and AM integrated plate with pin flow channel and LGDL, were fabricated simultaneously in the printer. The approximate building time was ~1.6 h, and the mass of the single plate is ~148 g. Due to the large surface roughness after printing, the AM plates were milled and polished to improve the surface smoothness. The plates were milled with

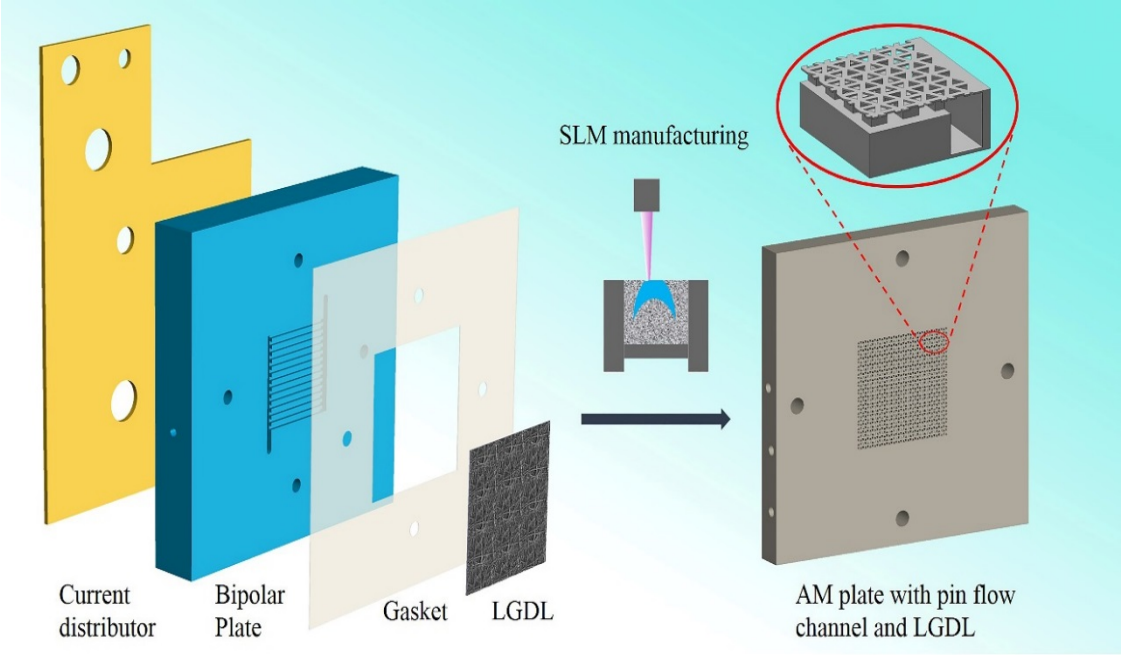

Figure 7. Schematic illustration of the integration of current distributor, bipolar plate, gasket, and LGDL into one AM plate via additive manufacturing.

sand paper (SiC grindings paper #250-1200, BUEHLER) gradually, and polished with a polishing machine, then ultrasonically cleaned for 15 min in both methanol and acetone.

3.5.2 Characterization and testing system

The ohmic resistance of the cathode was measured ex-situ using an AEMC Micro-Ohmmeter when assembling in the PEMEC. The crystal structure was identified by XRD using a Philips X'Pert materials research diffractometer operating at 45 kV and 40 mA with Cu Kα (λ = 1.5418 Å) as a radiation source. The surface morphologies of the AM plates were characterized by SEM performed by a field emission SEM JEOL JSM-6320F. EDS was performed using an EDAX Octane plus Silicon Drift Detector with EDAX's TEAM EDS analysis system. To in-situ evaluate performance, AM plates were incorporated into PEMECs. The detailed characteristics and working conditions of AM PEMECs are given in Table 1**.** Characteristics and working conditions of AM PEMECsTable 1 .

The CCM (Electrolyzer CCM from FuelCellsEtc, EZ-CCM) contained a Nafion 115 membrane with a thickness of 125 μm, an anode CL made of Iridium Ruthenium Oxide ($IrRuO_x$) with loading of 3 mg/cm^2, and a cathode CL made of platinum black (PtB) with loading of 3 mg/cm^2. The anode LGDL was Ti felt (from Bekaert) with a thickness of 0.35mm and a porosity of 75%. Toray Carbon Paper 090 (from FuelCellStore) with a thickness of 280 μm and a porosity of 78% was used as the cathode LGDL, except for the PEMEC with AM plate with pin flow channel and LGDL. The gasket was polyvinyl chloride (PVC). The anode BP was made of graphite with a parallel flow channel for all

Table 1. Characteristics and working conditions of AM PEMECs.

Materials and conditions	Details
PEM Type	Nafion® 115
Reaction Area	5 cm^2
PEM Thickness	125 μm
Catalyst at Anode Side	IrRuOx (3.0 mg/cm^2)
Catalyst at Cathode Side	PtB (3.0 mg/cm^2)
LGDL at Anode Side	Titanium felt
LGDL at Cathode Side	Toray carbon paper 090 except for the PEMECs with AM plate with pin flow channel and LGDL
Gasket	Polyamide chloride
BP at Anode Side	Graphite
BP at Cathode Side	AM plates for AM PEMECs, while graphite plate for conventional cell
PEMEC Temperature	20, 40, 60, and 80 °C
PEMEC Pressure	1 atm
DI Water Flow Rate at Anode Side	20 ml/min

cells, and the cathode BPs were AM plates for AM PEMECs and graphite BP for conventional PEMEC.

Two end plates were machined from commercial grade aluminum bulk to provide structure support and compression pressure; these end plates provide outlet and inlet for deionized (DI) water and gas. *In-situ* electrochemical measurements of the polarization curves and EIS were recorded using a Bio-Logic SP-300 potentiostat with a 5V / 10A booster, and all tests all repeated to make sure the reliability. All cells were tested at 1 atmosphere pressure. The PEMEC temperature was controlled at 20, 40, 60, and 80 °C by two heaters and two thermocouples connected to a Multi-Zone controller from OMEGA. The DI water was maintained at a flow rate of 20 ml/min by a KNF Neuberger diagram liquid pump, and heated by a PolyScience WB05 water bath. The polarization curves of all cells were recorded from 0 to 10 A with a scan rate of 100 mA/s; the EIS scans were swept from 200 kHz to 30 mHz at 1 A/cm^2, and then the results were fitted by using ZFit BIO-Logic to identify each the resistance and capacitance in the cell. The stability test of the cell with AM plate with pin flow channel and LGDL was carried out with a chronopotentiometry at current density of 0.2 A/cm^2 for 120 h at 80 °C.

3.6 Results and discussion

3.6.1 Ex-situ measurements

The AM plates are designed and manufactured to be 0.5 cm (thick) × 6.0 cm (long) × 6.0 cm (wide) with an active area of 5 cm^2. The spherical 316L powders (Renishaw) used for

the building have a diameter range of 15 - 45 μm, and an elemental composition is shown in Figure 8a. Energy dispersive spectrometry (EDS) and X-ray diffraction (XRD) images (Figure 8) show the element distributions at the plate surface are uniform and are almost the same as those of the raw powder. And XRD result of the AM plates is consistent with that of standard SS 316L, which means the crystal structure is not changed during AM process[40].

Figure 9a – c show the schematics of parallel flow channel, pin flow channel, and pin flow channel with LGDL, respectively. The parallel flow channels are 1 mm in width, and the lands are 1.5 mm in width and 1 mm in height. Pin flow channels are 1mm in width, and the cubic pins are 1 mm of side length. For AM integrated plate with pin flow channel and LGDL, the LGDL with a thickness of 150 μm is deposited onto pin flow channel directly. Its printed pore shape is equilateral triangle with a 1 mm of side length, and the width of land between two pores is about 0.25 mm. Figure 9d shows the photographic image of AM plates immediately after the printing process. The plate surfaces and lands are very rough and full of printing tracks due to the rapid melting and solidification process during printing. Photographic images of AM plates (Figure 9d – f) after polishing and cleaning indicate the surfaces are much smoother and better for assembling. Note that the raw powder particles at the sidewall are also removed. Figure 9g – i show the scanning electron microscopy (SEM) images of the flow channels and pore morphologies of AM plates after polishing and cleaning, which indicate a smooth microscale surface finish.

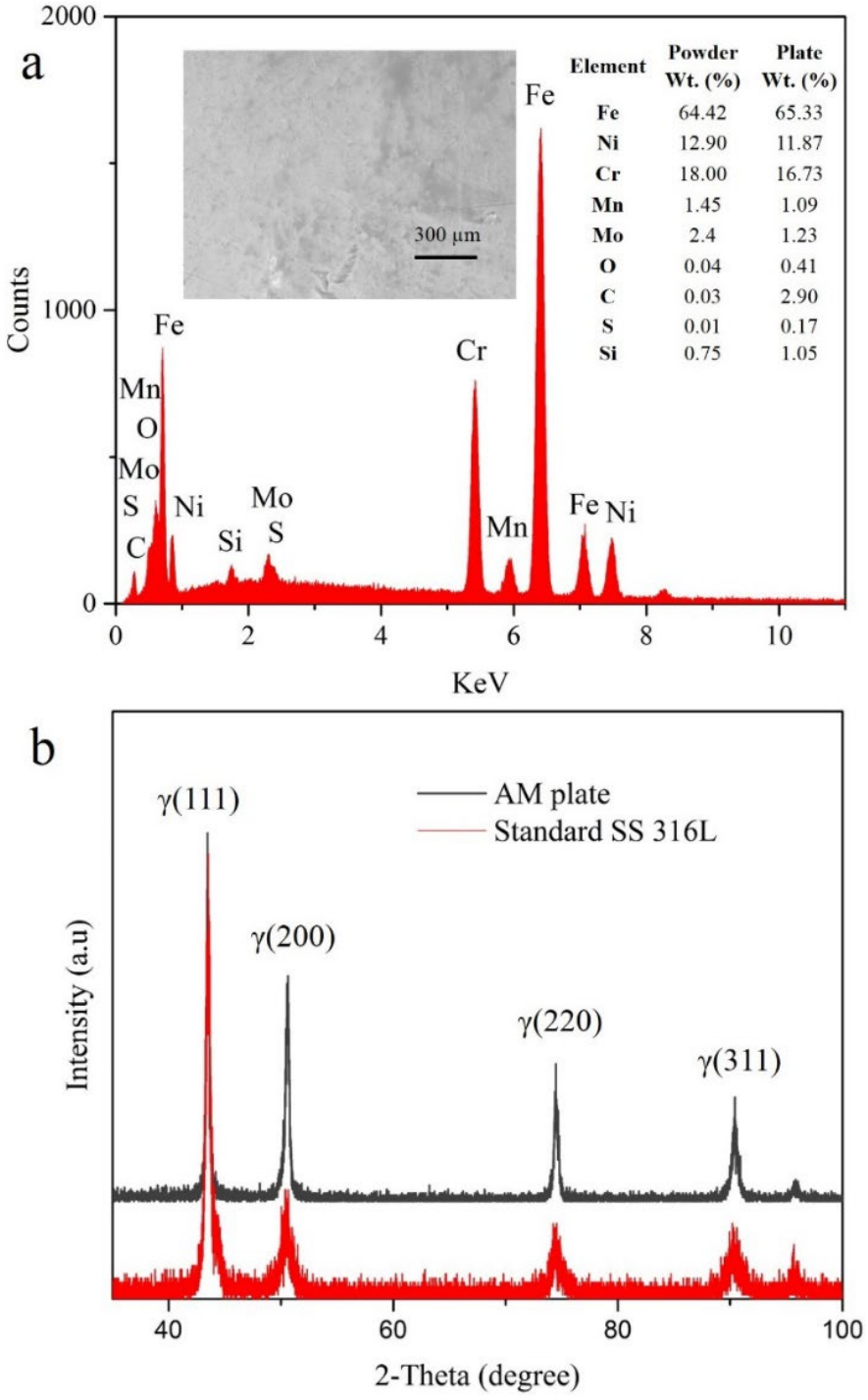

Figure 8. (a). EDS analysis of AM plates. (b). XRD analysis of AM plates.

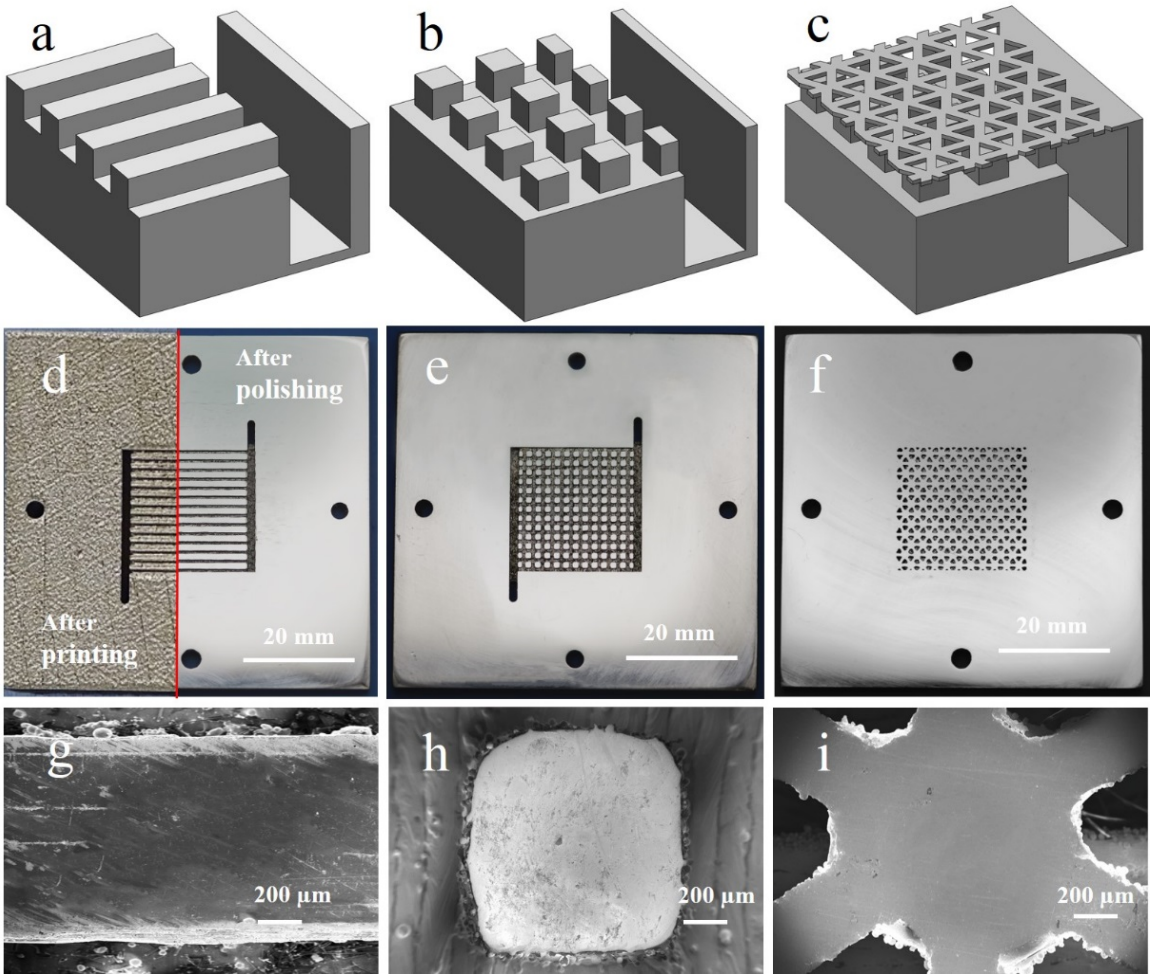

Figure 9. Schematics of (a) parallel flow channel, (b) pin flow channel, and (c) pin flow channel with LGDL; Photographs of (d) AM plate with parallel flow channel after printing and polishing, (e) AM plate with pin flow channel after polishing, and (f) AM integrated plate with pin flow channel with LGDL after polishing; SEM images of (g) parallel flow channel of AM plate, (h) pin flow channel of AM plate, and (i) LGDL of AM plate.

The details with different plates in each PEMEC are provided in Table 2. SS is considered to be a low-cost material for PEMECs compared to Ti; but anodic corrosion might be problematic, so the AM plates are only used at the cathode side for the feasibility study[41]. The conventional cathode in Cell 1 usually includes the BP, current distributor, LGDL, and gasket, while the AM plates with parallel and pin flow channels in Cells 2 and 3, respectively, can serve as the BP and current distributor, and the AM integrated plate with pin flow channel and LGDL in Cell 4 can function as a whole cathode. Thus, the number of cathode components can reduce from 4 to 1 in the AM single cell. In addition, the weight and volume of cathode greatly reduces from 266.90 g to 144.15 g, and from 122.83 cm^2 to 19.39 cm^2, respectively. If the AM integrated plates are used in PEMEC stacks that contain hundreds or thousands of cells, the configuration of PEMEC stacks will be greatly simplified, and the assembling cost and maintenance fee will also be reduced.

More importantly, the ohmic resistances of Cells 1, 2, 3, and 4 decrease from 6.52 to 0.10 mΩ, which means the integration of the BP, LGDL, gasket, and current distributor into one part (Cell 4) results in an extremely low overall ohmic resistance. The total ohmic resistances of the cathode electrode include electronic resistance of each component and interfacial contact resistances between two matting parts. When the electronic resistances of components are low, and the interfacial contact resistances will become dominant[42]. There is only one part at the cathode of Cell 4, so its interfacial contact resistances are eliminated, which results in the lowest ohmic resistance. The weights and volumes of these

AM electrodes are also relatively small compared with the conventional cathode components, as shown in Table 2, and the savings are more significant when considering PEMEC stacks powered in MW.

3.6.2 Polarization curves and EIS

The polarization curves reflect the PEMEC voltage-current relationship, and a lower voltage at a certain current density implies a better electrochemical performance[43, 44]. The total cell voltage can be defined according to Equation 1:

$$V = E + V_{act} + V_{ohm} + V_{trans} \quad (3\text{-}1)$$

where V is the operation cell voltage, E is the reversible voltage required for free energy difference between reactants and products. V_{act} is the activation loss. V_{trans} is concentration loss. V_{ohm} is caused by ohmic loss associated with ohmic resistance through the whole cell, resulting in a linear increase of voltage with current density[38]. The increases of voltage at low current density are dominated by activation loss; the increases at intermediate current density are dominated by ohmic polarization; while the increases at higher current density are dominated by concentration polarization.

A series of PEMEC polarization curves were recorded at 80 °C with a current density up to 2.0 A/cm^2 under one atmosphere air pressure, and the results are shown graphically in Figure 10a. The performances of the PEMECs with different cathode AM plates were gradually improved in the following order: conventional BP < AM plate with parallel channel < AM plate with pin channel < AM integrated plate with pin channel and LGDL, which are 1.887 V, 1.779 V, 1.773 V, and 1.716 V at 2.0 A/cm^2, respectively. The

Table 2. Evaluation of different cathodes.

Cell	Cathode	Component number	Weight [g]	Volume [cm^3]	Electrical resistance [mΩ]
1	graphite plate/carbon paper LGDL/current distributor/gasket	4	266.90	122.83	6.52
2	AM plate with parallel flow channel/carbon paper LGDL/gasket	3	227.10	29.55	5.61
3	AM plate with pin flow channel/carbon paper LGDL/gasket	3	219.04	28.46	3.35
4	AM integrated plate with pin flow channel and LGDL	1	144.15	19.39	0.10

performances of these PEMECs exceed with pin channel < AM integrated plate with pin channel and most of those found in the literatures[3, 18, 30, 38]. The PEMEC with AM integrated plate with pin channel and LGDL reaches the highest efficiency of 86.48%, and the efficiency is calculated with the thermo-neutral voltage of 1.484 V at 80 ^{o}C[45, 46]. The superior performance of the AM integrated plate with pin channel and LGDL can be rationalized by the lowest ohmic resistance, which is illustrated by the lowest gradient on the polarization curves at higher current density. And the gradient also reflect the ultralow ohmic resistance at the cathode, 0.1 mΩ in Table 2. The other two AM PEMECs almost share the same performance, which is also better than the conventional cell. It could be mentioned that the AM plate with pin channel would reduce the weight of raw material compared to the AM plate with parallel channel, especially when larger active area and scale are considered, since the volume of the pin lands is only half that of the parallel lands. Moreover, at the same voltage of 1.715 V, the hydrogen generation rate of the conventional cell is 115.29 ml/h, while those of the PEMECs are 147.29, 151.02 and 186.56 ml/h calculated from the current density, respectively (Figure 10a). The hydrogen generation rates in the three AM PEMECs are significantly increased by 27.75%, 30.99%, and 61.81% compared with the conventional cell, respectively. In the long term, the performance improvement in AM PEMEC can save the feedstock and energy which account for 71.9% of the total hydrogen levelized cost based on DOE's report[47]. When considering the larger industrial scale with 1,000 kg/day or more, the improvement in performance is of great influence on the cost saving of hydrogen production.

The results of electrochemical impedance spectroscopy (EIS) are organized in Nyquist plots. The left-most intersection of the Nyquist plot with the X-axis represents the ohmic resistance, and the right-most intersection represents the total resistance of the cell. From the Nyquist plots in Figure 10b, the ohmic resistances of PEMECs with the conventional graphite BP and AM plates with parallel flow channel, pin flow channel, pin flow channel with LGDL are 0.1948, 0.1286, 0.1295, 0.0919 $\Omega \cdot cm^2$, respectively, and the AM integrated plates with pin flow channel and LGDL shows the lowest ohmic resistance in the operating PEMEC. And those ohmic resistances are consistent with the gradients of the polarization curves. As aforementioned, the ohmic resistance includes electronic and ionic resistance of each component, and interfacial contact resistances between two mating parts.

All the PEMECs with different plates share the same CCMs which means the ionic resistance is constant , and the electronic resistance is relatively small compared to interfacial contact resistance and ionic resistance[43]. Thus, the reduction of ohmic resistance should mainly be due to the elimination of interfacial contact resistance between BPs, LGDLs, and current distributors[48]. The sum of activation and concentration losses can be calculated from the difference of total resistance and ohmic resistance. The change of activation and concentration losses of different PEMECs is relatively small only 0.002 $\Omega \cdot cm^2$ (Figure 10b). It should be mentioned that the PEMECs with AM plates with parallel flow channel and pin flow channel almost share the same ohmic resistance and total resistance, which means the patterns of flow channel will not have much influence on the performance of PEMECs when the current density is below 2 A/cm^2. Although the flow

patterns mainly affect the mass flow distribution and concentration polarization, those effects appear to be negligible at intermediate current density in this study.

The effect of temperature on the PEMECs was studied in a range from 20 ºC to 80 ºC (Figure 10c). The Tafel slope at low current density indicates the activation loss, and Figure 10c shows increasing temperature gives rise to a decrease of the activation loss. Molecules participating in the reaction of water splitting have higher kinetic energy and probability of molecular collisions when the temperature increases, which results in a lower activation loss[43, 49].

In addition, Figure 10c also shows that elevated temperatures result in smaller gradients on linear polarization curves at higher current densities. This indicates smaller ohmic losses, which agree with the EIS results in Figure 10d. The ionic resistance of the electrolyte and the interfacial contact resistance between mating components mainly contribute to the total ohmic resistance. The proton conductivity of CCM will be promoted as the temperature is elevated, which will lower the ohmic resistance and enhance the performance[32].

The electrical conductivity of metal and graphite parts is nearly constant for this temperature range, but thermal expansion of components may contribute to the decrease of interfacial ohmic resistance[50]. Due to the thermal expansion, the interfacial contact compression pressure of components of PEMECs will be enhanced, and the interfacial contact resistance will be diminished[51].

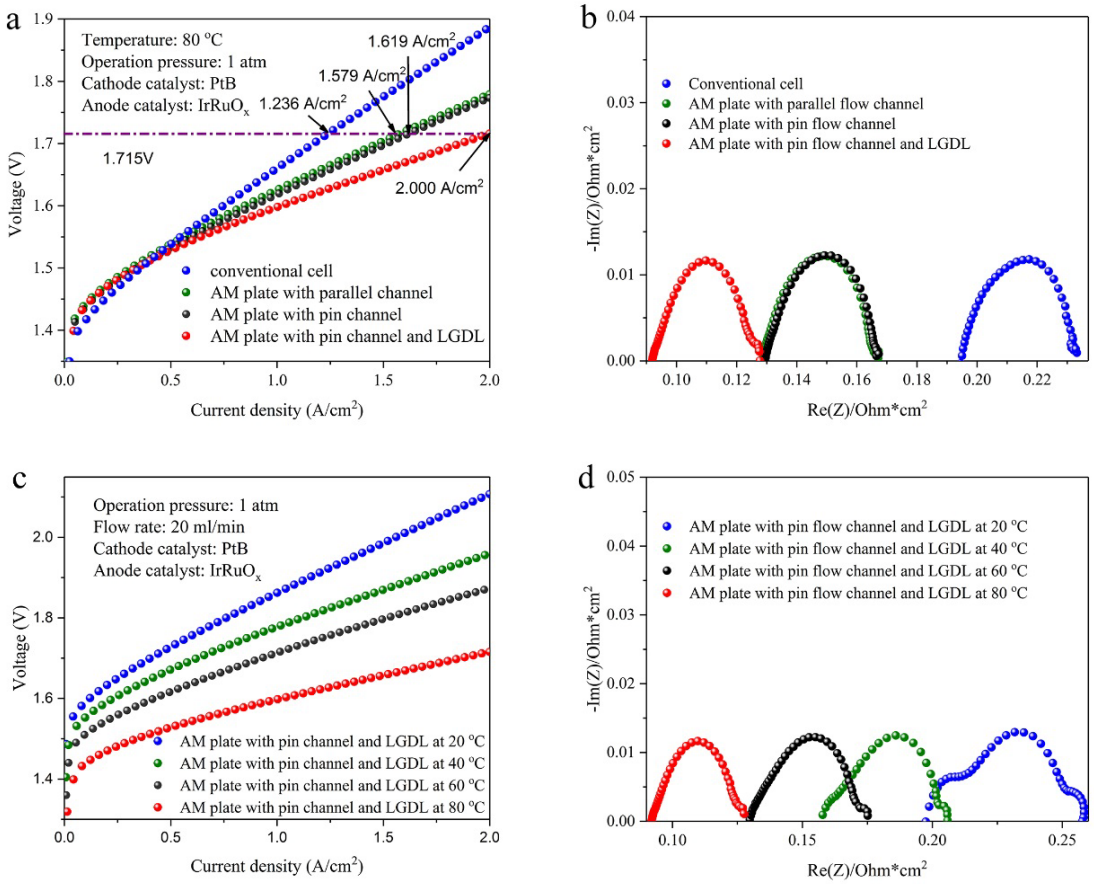

Figure 10. (a) Polarization curves and (b) EIS results of PEMECs with different cathode plates. (c) Polarization curves and (d) EIS results of PEMECs AM integrated plate with pin flow channel and LGDL at different temperatures.

3.6.3 Quantifications of AM plates on PEMEC performance

In order to further quantify the different voltage losses, an EEC is employed to model the EIS curves and to estimate each loss, and the results are shown in Figure 11 and Figure 11a represents the simplified illustration of ion and electron transport processes across a PEMEC, and Figure 11b is an associated EEC model[43]. An electrical double layer exists at the interface between the electrolyte and adjacent electrode, then a buildup of charge comes out in this layer, and the voltage difference needed to overcome the buildup of charge results in the activation loss[52]. R_{CL}, Z_{diff} and C_{DL} are the activation resistance, diffusion impedance, and capacitor associated with the electrical double layer, respectively. R_{mem} is the ionic resistance of the PEM with CLs. R_a and R_c represent the ohmic resistances associated with BPs, LGDLs, and current distributors at the anode and cathode sides, respectively.

The R_s in Table 3 is the sum of R_a, R_{mem}, and R_c. The diffusion impedance (Z_{diff}) associated with the diffusion transporting of mass into and out of the reacting surface is modelled by the Warburg element (W_d), and the Z_{diff} is given as Equation 2:[32, 53]

$$Z_{diff} = R_d \frac{\tanh\sqrt{it_d 2\pi f}}{\sqrt{it_d 2\pi f}} \tag{3-2}$$

where t_d is the time constant needed for mass diffussion, i is the imaginary number, f is the scanning frequency, and R_d is the diffusion resistance.

Figure 11c shows the EIS fitting result for the AM integrated plate with pin and LGDL at 1 A/ cm^2 and 80 °C, the blue dots are the EIS experimental result, and the red line show EEC fitting result. The EEC fitting results of all three AM PEMECs are listed in Table 3.

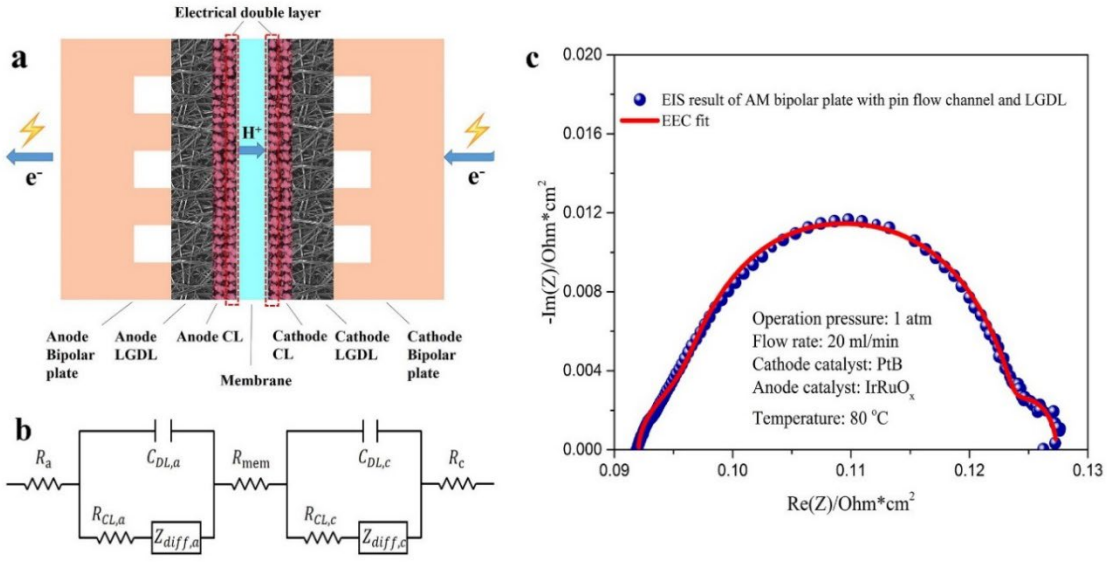

Figure 11. (a) Simplified illustration of ion and electron exchange processes across PEMECs. (b) Equivalent electrical circuit. (c) In-situ EIS results and the EEC fitting of AM PEMECs with pin flow channel and LGDL.

Table 3. The EEC fitting parameters of EIS of different cells at 1.0 A/cm2 and 80 °C (A1 – cell with AM plate with parallel flow channel; A2 – cell with AM plate with pin flow channel; A3 – cell with AM integrated plate with pin flow channel and LGDL.).

Cell	R_s [Ohm]	$R_{CL,a}$ [Ohm]	Rd_1 [Ohm]	$C_{DL,a}$ [F]	t_d (S)	$R_{CL,c}$ [Ohm]	Rd_2 [Ohm]	$C_{DL,c}$ [F]	Error [%]
A1	0.0258	$3.439e^{-3}$	$0.4579e^{-3}$	2.657	0.724	$0.817e^{-3}$	$2.738e^{-3}$	0.159	0.22
A2	0.0259	$3.533e^{-3}$	$0.5021e^{-3}$	2.492	0.853	$0.742e^{-3}$	$2.763e^{-3}$	0.132	0.06
A3	0.0183	$2.821e^{-3}$	$0.935e^{-3}$	2.350	2.058	$0.574e^{-3}$	$2.812e^{-3}$	0.273	0.17

and the fitting error is less than 0.3%, which confirm a good coincidence with the experimental results. The results of R_s show Cell A3 with the integrated AM plate with pin and LGDL obtains the smallest ohmic resistance, which result in the best performance compared with other two cells. R_{CL} represents the activation resistance, and $R_{CL,a}$ is greater than $R_{CL,c}$ in every cell, which is corresponded to the fact that activation overpotential of oxygen evolution reaction is higher than that of hydrogen evolution reaction[54]. The time constant, t_d, is the sum of time constant at both side, which indicates the mass diffusion process in the cell with AM plate with pin and LGDL is not as good as that in cells with the other two plates. This may due to lower porosity and larger pore size of printed LGDL that lead to diminished mass transporting [32, 46, 55]. However, the increase of time constant results in few changes of concentration overpotential when current density is below 2 A/cm^2.

3.6.4 Stability

Stability of materials and components is one of the principal concerns for PEMECs, since the harsh environment within the cell promotes corrosion and degradation, the stability can also provide evidence about if the AM SS plate is suitable for PEMECs for a long run[38, 56]. In order to evaluate the stability of the AM SS plate, a test was conducted on the cell with the AM integrated plate with pin and LGDL at a constant current density of 0.2 A/cm^2 at 80 °C for a period of 120 h, and other parts are identical to those employed in previous *in-situ* tests. The results of E_{cell} vs. t are presented in Figure 12a. During the initial 10 h, there is a rapid increase of voltage, 1.375 mV/h; this is likely associated with the loss of a

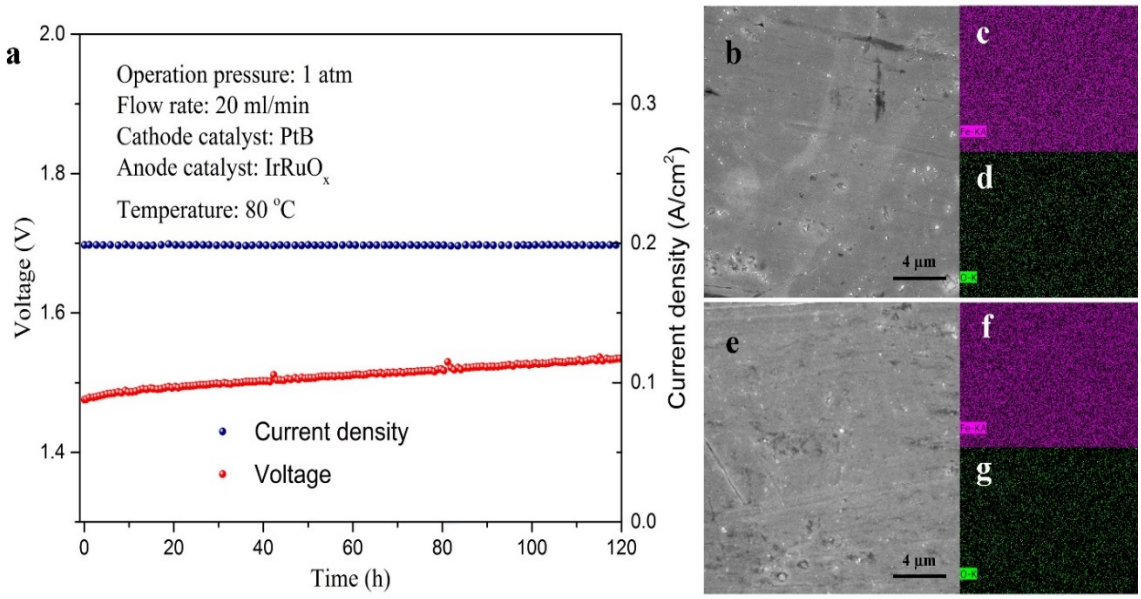

Figure 12. (a) Stability test of PEMECs with AM plate with pin and LGDL. (b) SEM image of AM plate before stability test and its corresponding (c) Fe and (d) O EDS mappings. (d) SEM image of AM plate after stability test and its corresponding (f) Fe and (g) O EDS mappings.

minor amount of the catalyst and the degradation of the membrane, and not caused by the degradation of AM plates, since the stainless steels are resistant to hydrogen embrittlement [41, 57].

After the initial degradation, the rate of change of voltage decreases from 1.375 mV/h to 0.466 mV/h gradually, which indicates a comparatively good stability[30, 38]. SEM images of AM plate before and after stability test (Figure 12b, e) indicate the surface structure did not change much. Corresponding Fe and O EDS mapping images, as shown in Figure 12c, d, f, g, respectively, also show the element distributions of AM SS plate after test are uniform and almost remain the same as that before test, which indicate the AM SS plate are not corroded during working, and the AM plate is durable at the cathode side.

3.7 Conclusions

The multifunctional and integrated cells with highly complex inner structures, which served as a combination of several components in PEMECs, were developed from stainless steel powders with AM technology. To the best of our knowledge, it is the first time that the PEMEC parts are integrated into one plate for water splitting and hydrogen production. The structural innovations of the plates provide a fundamental development for the simplification of PEMECs, which significantly reduce its part number and weight. Moreover, an excellent performance of 1.716 V is achieved at 80 °C and 2 A/cm^2, which leads to the superior efficiency of 86.48% due to the ultralow ohmic resistance. Then EIS

results are modelled with equivalent electrochemical circuits (EECs) to characterize the resistance, impedance, and capacitance in AM PEMECs, which provides insight, analysis, and detailed information that contribute to a better performance. These results demonstrate the viability of efficient PEMECs with ultralow ohmic resistances for hydrogen production. The AM technology opens the opportunity for optimal configurations of PEMECs, as well as marks a new step to the development of other energy conversion devices.

References

[1] J. A. Turner, "Sustainable hydrogen production," *Science,* vol. 305, pp. 972-974, 2004.

[2] M. Budt, D. Wolf, R. Span, and J. Yan, "A review on compressed air energy storage: Basic principles, past milestones and recent developments," *Applied Energy,* vol. 170, pp. 250-268, 2016.

[3] M. Carmo, D. L. Fritz, J. Mergel, and D. Stolten, "A comprehensive review on PEM water electrolysis," *International Journal of Hydrogen Energy,* vol. 38, pp. 4901-4934, 2013.

[4] V. R. Stamenkovic, D. Strmcnik, P. P. Lopes, and N. M. Markovic, "Energy and fuels from electrochemical interfaces," *Nature Materials,* vol. 16, pp. 57-69, 2017.

[5] N. Duić, Z. Guzović, V. Kafarov, J. J. Klemeš, B. vad Mathiessen, and J. Yan, "Sustainable development of energy, water and environment systems," *Applied energy,* vol. 101, pp. 3-5, 2013.

[6] M. A. Pellow, C. J. Emmott, C. J. Barnhart, and S. M. Benson, "Hydrogen or batteries for grid storage? A net energy analysis," *Energy & Environmental Science,* vol. 8, pp. 1938-1952, 2015.

[7] X. Tong, Y. Zhou, L. Jin, K. Basu, R. Adhikari, G. S. Selopal*, et al.*, "Heavy metal-free, near-infrared colloidal quantum dots for efficient photoelectrochemical hydrogen generation," *Nano Energy,* vol. 31, pp. 441-449, 2017.

[8] U. Desideri, F. Zepparelli, V. Morettini, and E. Garroni, "Comparative analysis of concentrating solar power and photovoltaic technologies: technical and environmental evaluations," *Applied energy,* vol. 102, pp. 765-784, 2013.

[9] U. Desideri and P. E. Campana, "Analysis and comparison between a concentrating solar and a photovoltaic power plant," *Applied Energy,* vol. 113, pp. 422-433, 2014.

[10] A. Sternberg and A. Bardow, "Power-to-What?–Environmental assessment of energy storage systems," *Energy & Environmental Science,* vol. 8, pp. 389-400, 2015.

[11] S. Siracusano, V. Baglio, N. Van Dijk, L. Merlo, and A. S. Aricò, "Enhanced performance and durability of low catalyst loading PEM water electrolyser based on a short-side chain perfluorosulfonic ionomer," *Applied Energy,* vol. 192, pp. 477-489, 2017.

[12] K. E. Ayers, E. B. Anderson, C. Capuano, B. Carter, L. Dalton, G. Hanlon*, et al.*, "Research advances towards low cost, high efficiency PEM electrolysis," *ECS Transactions,* vol. 33, pp. 3-15, 2010.

[13] T. Reier, H. N. Nong, D. Teschner, R. Schlögl, and P. Strasser, "Electrocatalytic Oxygen Evolution Reaction in Acidic Environments–Reaction Mechanisms and Catalysts," *Advanced Energy Materials,* 2016.

[14] J. Yan, T. Shamim, S. Chou, U. Desideri, and H. Li, "Clean, efficient and affordable energy for a sustainable future," ed: Elsevier, 2017.

[15] G. Cinti, A. Baldinelli, A. Di Michele, and U. Desideri, "Integration of Solid Oxide Electrolyzer and Fischer-Tropsch: A sustainable pathway for synthetic fuel," *Applied Energy,* vol. 162, pp. 308-320, 2016.

[16] Z. Pan, Q. Liu, L. Zhang, J. Zhou, C. Zhang, and S. H. Chan, "Experimental and thermodynamic study on the performance of water electrolysis by solid oxide electrolyzer cells with Nb-doped Co-based perovskite anode," *Applied Energy,* vol. 191, pp. 559-567, 2017.

[17] J. Russell, L. Nuttall, and A. Fickett, "Hydrogen generation by solid polymer electrolyte water electrolysis," *American Chemical Society Division of Fuel Chemistry Preprints,* vol. 18, p. 24e40, 1973.

[18] J. R. Hudkins, D. G. Wheeler, B. Peña, and C. P. Berlinguette, "Rapid prototyping of electrolyzer flow field plates," *Energy & Environmental Science,* 2016.

[19] S. Zhao, Y. Wang, J. Dong, C.-T. He, H. Yin, P. An*, et al.*, "Ultrathin metal–organic framework nanosheets for electrocatalytic oxygen evolution," *Nature Energy,* vol. 1, p. 16184, 2016.

[20] M. Chhowalla, H. S. Shin, G. Eda, L.-J. Li, K. P. Loh, and H. Zhang, "The chemistry of two-dimensional layered transition metal dichalcogenide nanosheets," *Nature chemistry,* vol. 5, pp. 263-275, 2013.

[21] A. Bergmann, E. Martinez-Moreno, D. Teschner, P. Chernev, M. Gliech, J. F. De Araújo*, et al.*, "Reversible amorphization and the catalytically active state of crystalline Co3O4 during oxygen evolution," *Nature communications,* vol. 6, 2015.

[22] B. C. Steele and A. Heinzel, "Materials for fuel-cell technologies," *Nature,* vol. 414, pp. 345-352, 2001.

[23] H. Tawfik, Y. Hung, and D. Mahajan, "Metal bipolar plates for PEM fuel cell—a review," *Journal of Power Sources,* vol. 163, pp. 755-767, 2007.

[24] G. Yang, J. Mo, Z. Kang, F. A. List, J. B. Green, S. S. Babu*, et al.*, "Additive manufactured bipolar plate for high-efficiency hydrogen production in proton exchange membrane electrolyzer cells," *International Journal of Hydrogen Energy,* vol. 42, pp. 14734-14740, 2017.

[25] C. Minke, T. Hickmann, A. R. dos Santos, U. Kunz, and T. Turek, "Cost and performance prospects for composite bipolar plates in fuel cells and redox flow batteries," *Journal of Power Sources,* vol. 305, pp. 182-190, 2016.

[26] J. Mo, R. R. Dehoff, W. H. Peter, T. J. Toops, J. B. Green, and F.-Y. Zhang, "Additive manufacturing of liquid/gas diffusion layers for low-cost and high-efficiency hydrogen production," *International Journal of Hydrogen Energy,* 2016.

[27] Z. Kang, J. Mo, G. Yang, Y. Li, D. A. Talley, S. T. Retterer*, et al.*, "Thin film surface modifications of thin/tunable liquid/gas diffusion layers for high-efficiency proton exchange membrane electrolyzer cells," *Applied Energy,* vol. 206, pp. 983-990, 2017.

[28] P. Millet, D. Dragoe, S. Grigoriev, V. Fateev, and C. Etievant, "GenHyPEM: a research program on PEM water electrolysis supported by the European

Commission," *International Journal of Hydrogen Energy,* vol. 34, pp. 4974-4982, 2009.

[29] R. Taspinar, S. Litster, and E. Kumbur, "A computational study to investigate the effects of the bipolar plate and gas diffusion layer interface in polymer electrolyte fuel cells," *International Journal of Hydrogen Energy,* vol. 40, pp. 7124-7134, 2015.

[30] P. Lettenmeier, R. Wang, R. Abouatallah, B. Saruhan, O. Freitag, P. Gazdzicki*, et al.*, "Low-Cost and Durable Bipolar Plates for Proton Exchange Membrane Electrolyzers," *Scientific Reports,* vol. 7, p. srep44035, 2017.

[31] A. Gago, S. Ansar, B. Saruhan, U. Schulz, P. Lettenmeier, N. Cañas*, et al.*, "Protective coatings on stainless steel bipolar plates for proton exchange membrane (PEM) electrolysers," *Journal of Power Sources,* vol. 307, pp. 815-825, 2016.

[32] Z. Kang, J. Mo, G. Yang, S. T. Retterer, D. A. Cullen, T. J. Toops*, et al.*, "Investigation of thin/well-tunable liquid/gas diffusion layers exhibiting superior multifunctional performance in low-temperature electrolytic water splitting," *Energy & Environmental Science,* 2017.

[33] B. Han, J. Mo, Z. Kang, G. Yang, W. Barnhill, and F.-Y. Zhang, "Modeling of two-phase transport in proton exchange membrane electrolyzer cells for hydrogen energy," *International Journal of Hydrogen Energy,* vol. 42, pp. 4478-4489, 2017.

[34] J. Mo, Z. Kang, G. Yang, S. T. Retterer, D. A. Cullen, T. J. Toops*, et al.*, "Thin liquid/gas diffusion layers for high-efficiency hydrogen production from water splitting," *Applied Energy,* vol. 177, pp. 817-822, 2016.

[35] S. M. Steen III, J. Mo, Z. Kang, G. Yang, and F.-Y. Zhang, "Investigation of titanium liquid/gas diffusion layers in proton exchange membrane electrolyzer cells," *International Journal of Green Energy,* vol. 14, pp. 162-170, 2017.

[36] S. M. Thompson, L. Bian, N. Shamsaei, and A. Yadollahi, "An overview of Direct Laser Deposition for additive manufacturing; Part I: Transport phenomena, modeling and diagnostics," *Additive Manufacturing,* vol. 8, pp. 36-62, 2015.

[37] W. E. Frazier, "Metal additive manufacturing: a review," *Journal of Materials Engineering and Performance,* vol. 23, pp. 1917-1928, 2014.

[38] G. Chisholm, P. J. Kitson, N. D. Kirkaldy, L. G. Bloor, and L. Cronin, "3D printed flow plates for the electrolysis of water: an economic and adaptable approach to device manufacture," *Energy & Environmental Science,* vol. 7, pp. 3026-3032, 2014.

[39] K. Alayavalli and D. L. Bourell, "Fabrication of modified graphite bipolar plates by indirect selective laser sintering (SLS) for direct methanol fuel cells," *Rapid prototyping journal,* vol. 16, pp. 268-274, 2010.

[40] Y. Wang and D. O. Northwood, "An investigation into TiN-coated 316L stainless steel as a bipolar plate material for PEM fuel cells," *Journal of Power Sources,* vol. 165, pp. 293-298, 2007.

[41] P. Lettenmeier, R. Wang, R. Abouatallah, F. Burggraf, A. Gago, and K. Friedrich, "Coated Stainless Steel Bipolar Plates for Proton Exchange Membrane Electrolyzers," *Journal of The Electrochemical Society,* vol. 163, pp. F3119-F3124, 2016.

[42] W. Yoon, X. Huang, P. Fazzino, K. L. Reifsnider, and M. A. Akkaoui, "Evaluation of coated metallic bipolar plates for polymer electrolyte membrane fuel cells," *Journal of Power Sources,* vol. 179, pp. 265-273, 2008.

[43] M. M. Mench, *Fuel cell engines*: John Wiley & Sons, 2008.

[44] B. Bensmann, R. Hanke-Rauschenbach, G. Müller-Syring, M. Henel, and K. Sundmacher, "Optimal configuration and pressure levels of electrolyzer plants in context of power-to-gas applications," *Applied Energy,* vol. 167, pp. 107-124, 2016.

[45] E. Zoulias, E. Varkaraki, N. Lymberopoulos, C. N. Christodoulou, and G. N. Karagiorgis, "A review on water electrolysis," *TCJST,* vol. 4, pp. 41-71, 2004.

[46] C. M. Hwang, M. Ishida, H. Ito, T. Maeda, A. Nakano, Y. Hasegawa*, et al.*, "Influence of properties of gas diffusion layers on the performance of polymer electrolyte-based unitized reversible fuel cells," *International journal of hydrogen energy,* vol. 36, pp. 1740-1753, 2011.

[47] (2016). *DOE Technical Targets for Hydrogen Production from Electrolysis*. Available: https://energy.gov/eere/fuelcells/doe-technical-targets-hydrogen-production-electrolysis

[48] S. Siracusano, V. Baglio, A. Di Blasi, N. Briguglio, A. Stassi, R. Ornelas*, et al.*, "Electrochemical characterization of single cell and short stack PEM electrolyzers based on a nanosized IrO 2 anode electrocatalyst," *International journal of hydrogen energy,* vol. 35, pp. 5558-5568, 2010.

[49] W. T. Hong, M. Risch, K. A. Stoerzinger, A. Grimaud, J. Suntivich, and Y. Shao-Horn, "Toward the rational design of non-precious transition metal oxides for oxygen electrocatalysis," *Energy & Environmental Science,* vol. 8, pp. 1404-1427, 2015.

[50] B. Han, J. Mo, Z. Kang, and F.-Y. Zhang, "Effects of membrane electrode assembly properties on two-phase transport and performance in proton exchange membrane electrolyzer cells," *Electrochimica Acta,* vol. 188, pp. 317-326, 2016.

[51] J. Ge, A. Higier, and H. Liu, "Effect of gas diffusion layer compression on PEM fuel cell performance," *Journal of Power Sources,* vol. 159, pp. 922-927, 2006.

[52] M. A. Modestino, S. M. H. Hashemi, and S. Haussener, "Mass transport aspects of electrochemical solar-hydrogen generation," *Energy & Environmental Science,* vol. 9, pp. 1533-1551, 2016.

[53] F. Köleli, T. Röpke, and C. H. Hamann, "Electrochemical impedance spectroscopic investigation of CO 2 reduction on polyaniline in methanol," *Electrochimica acta,* vol. 48, pp. 1595-1601, 2003.

[54] N.-T. Suen, S.-F. Hung, Q. Quan, N. Zhang, Y.-J. Xu, and H. M. Chen, "Electrocatalysis for the oxygen evolution reaction: recent development and future perspectives," *Chemical Society Reviews,* vol. 46, pp. 337-365, 2017.

[55] L. Cindrella, A. Kannan, J. Lin, K. Saminathan, Y. Ho, C. Lin*, et al.*, "Gas diffusion layer for proton exchange membrane fuel cells—A review," *Journal of Power Sources,* vol. 194, pp. 146-160, 2009.

[56] X. Wang, W. Li, D. Xiong, and L. Liu, "Fast fabrication of self-supported porous nickel phosphide foam for efficient, durable oxygen evolution and overall water splitting," *Journal of Materials Chemistry A,* vol. 4, pp. 5639-5646, 2016.

[57] J. Xu, D. Aili, Q. Li, E. Christensen, J. O. Jensen, W. Zhang*, et al.*, "Oxygen evolution catalysts on supports with a 3-D ordered array structure and intrinsic proton conductivity for proton exchange membrane steam electrolysis," *Energy & Environmental Science,* vol. 7, pp. 820-830, 2014.

CHAPTER IV

BIPOLAR PLATE DEVELOPMENT WITH ADDITIVE MANUFACTURING AND PROTECTIVE COATING FOR DURABLE AND HIGH-EFFICIENCY HYDROGEN PRODUCTION

A version of this chapter was originally published by Gaoqiang Yang:

Yang, Gaoqiang, Shule Yu, Jingke Mo, Zhenye Kang, Yeshi Dohrmann, Frederick A. List, Johney B. Green, Sudarsanam S. Babu, and Feng-Yuan Zhang. "Bipolar plate development with additive manufacturing and protective coating for durable and high-efficiency hydrogen production." *Journal of Power Sources* 396 (2018): 590-598.

I am fully responsible for the work submitted in these publications.

4.1 Abstract

Additive manufacturing (AM) of the complex devices for energy application remains an almost unexplored area, and the harsh acidic environment also limits the application of AM parts in water splitting for hydrogen production. Here, bipolar plates (BPs), which are used to transport reactants/products and conduct electrons in proton exchange membrane electrolyzer cells (PEMECs), are printed from stainless steel (SS) with selective laser melting (SLM). Then surface treatments are employed on those BPs by thin film electroplating with Au, and the protective thin layer enables the utilization of AM SS parts to both cathode and anode sides of water electrolyzer cells and exhibits superior corrosion resistances and electronic conductivities. The Au-coated AM SS BPs deliver a low interfacial contact resistance (6.4 $m\Omega \cdot cm^2$ under 1.45 MPa) and an excellent performance in PEMECs (1.71 V at 2 A/cm^2), and maintain a remarkable durability in the simulated anode environment compared with the uncoated AM SS BPs and conventional graphite BPs. This approach demonstrates the possibility of 3-dimentional printing fully integrated water electrolyzer cells at both anode and cathode sides.

4.2 Highlights

- Additive manufacturing and electroplating technologies are incorporated.
- Gold electroplating enables the using of 3D printed stainless steel BP at anode and cathode in electrolyzer.
- An ultralow interfacial contact resistance is achieved
- Au-coated AM BPs provide a low voltage, 1.71 V at 2 A/cm^2 and 80 ^{o}C.
- A route for the development of energy conversion devices working at harsh conditions with cheap material is offered.

4.3 Introduction

Due to the requirement for a cleaner environment, renewable and green energy, such as wind and solar, is considered a promising alternative to fossil fuels for electricity production [1-13]. Because these energy sources are intermittent and unpredictable, a highly efficient and quickly responsive energy conversion system needs to be developed to store the energy as electricity. With the capability of handling the fluctuations of intermitted energy, proton exchange membrane electrolyzer cells (PEMECs) are attracting significant attentions [2, 4, 14-18]. But the relatively low performance and high cost limit their wide commercialization [4, 5, 15, 19-23].

In a single conventional PEMEC, a catalyst coated membrane (CCM) is sandwiched by two liquid/gas diffusion layers (LGDLs), two bipolar plates (BPs), and two current distributors (CDs), as shown in Figure 13a. At the anode side, water is split into oxygen,

electrons, and protons, as in equation (1), then the protons transport from the anode to the cathode through the proton exchange membrane, and react with electrons to form hydrogen at the cathode catalyst layer (CL), as shown in equation (2)[24]:

$$2H_2O \rightarrow 4H^+ + O_2 + 4e^- \quad (4\text{-}1)$$

$$4H^+ + 4e^- \rightarrow 2H_2 \quad (4\text{-}2)$$

At the cathode side, there is a reducing environment full of hydrogen with a low potential, so BPs and LGDLs are seldom corroded[25]. For the anode side, the thermo-neutral voltage of the PEMECs at room temperature is ~1.48 V, while the operating voltage could be over 2.00 V at a high current density and hydrogen producing rate, and the fluorinated polymer with sulfonic acid side chains in the CCMs will cause a strong acidic environment[26-28]. Thus, the components in an oxygen rich anodic ambient, where the pH is low and the potential is high, will be easily corroded.

Most recent researches on PEMECs have focused on catalyst developments for the hydrogen evolution reaction (HER) and oxygen evolution reaction (OER) [29-36]. Few improvements have been realized for other components, such as the LGDLs and BPs[37, 38]. The BPs distribute mass and electron and should provide good mechanical support for the PEMECs. They are expensive components, which account for ~ 48 % of the cost of the PEMEC stacks [5, 6, 39-41]. Stainless steel (SS), titanium (Ti) and graphite are the most widely used materials for BPs [42-46]. Ti has good electrical conductivity, corrosion resistance and mechanical strength, but it is very expensive and difficult to machine due to its hardness [5, 25, 26, 46-48]. Even graphite is widely used due to its high electrical

conductivity, but its brittleness leads to high machining cost. For SS, the electrical conductivity and mechanical strength are good, but it can easily corrode at the anode where there is an acidic environment and a high electrical potential.

To improve the efficiency and reduce the cost of PEMECs, either simplifying the manufacturing process, or using cheap materials like SS and plastic materials could be effective[25, 49-51]. However, traditional moulding and cutting processes cannot provide many improvements due to material waste and challenging machining to produce complex flow channels. As an alternative to traditional manufacturing, additive manufacturing (AM) technology is a revolutionary approach to fabricate complex structures with nearly zero waste of material. Several researchers have tried to print bipolar plates with plastic and SS materials using AM to improve the performance and reduce the cost of PEMECs or proton exchange membrane fuel cells (PEMFCs). Scotti et al. tried to print SS micro flow field plates for fuel cell, but measurements of corrosion resistance and durability were not provided[49]. Conductive polylactic acid (PLA) was also used to print BPs for water electrolysis, but the performance of the cells was neither acceptable nor practical[20, 51]. Our group used the AM SS BPs at the cathode side where a reducing environment occurs, those AM SS plates served as serval parts in the PEMEC, which reduce the weight and cost, and also improved the performance. But the SS bipolar plates have not been incorporated into the anode side due to the high potential and acidic environment, and the using of AM SS plats at anode side of PEMEC need to be explored[21, 52].

The corrosions of BPs at acidic environment in PEMECs can not only lead to the damage of the plate structure, but also result in the increase of contact resistance and contamination of the CCMs, especially for SS material [5, 43, 53-55]. Meanwhile, SS typically contains Cr which will be oxidized into a passive layer of Cr_2O_3, particularly at the anode of PEMECs; then the passive layer will lead to a higher interfacial contact resistance (ICR). ICR is of great importance for the performance of PEMECs or PEMFCs, and the target of US Department of Energy is 20 $m\Omega \cdot cm^2$[53, 56, 57]. A higher ICR will lead to a faster increasing in working voltage with the increment of working current density, and the efficiency will be reduced, and the electricity costs will be increased[47].

Herein, in order to use AM parts at both the anode and cathode sides in PEMECs, we proposed a protective coating on AM SS BPs for high-efficiency and low-cost PEMECs. The BPs were firstly printed using selective laser melting (SLM) technologies, then the BPs were coated with gold by electroplating to form a protecting layer, as shown in Figure 13b. Compared with traditional BPs, the AM plates not only have a greatly simplified fabrication processes, but also help to lower the cost and provide a rapid prototyping process. In *ex-situ* tests, the Au-coated AM SS BPs show a very low ICR, 6.4 $m\Omega \cdot cm^2$ under 1.4 MPa, compared with the bare AM SS BPs and graphite BPs. In *in-situ* tests, those AM SS BPs are incorporated into both the anode and cathode sides in PEMECs, and an excellent performance is achieved even at a high current density. The durability test also indicates the Au-coated AM SS BPs are suitable for highly corrosive environment. The results suggest that AM technologies combined with protective coatings have a potential

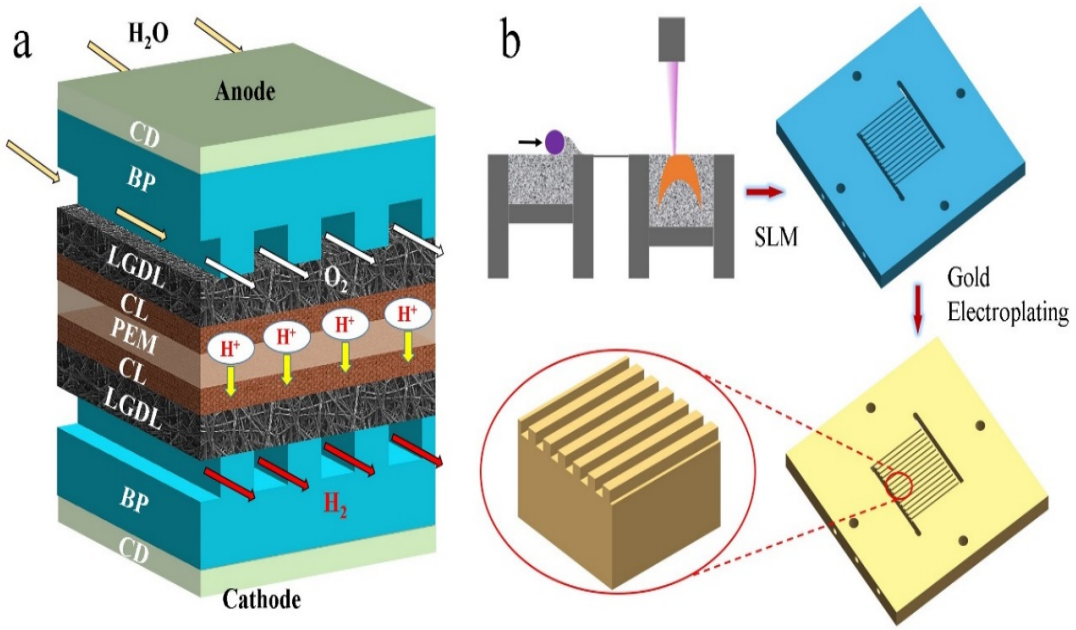

Figure 13. Schematic of (a) the internal structure of a PEMEC, (b) manufacturing processes of Au-coated AM SS BPs.

to rapidly produce high-efficiency and low-cost integrated energy conversion devices with better performance, and will facilitate the design and improvement of those devices.

4.4 Experimental details

4.4.1 Additive manufacturing of BPs

The BPs were designed using SOLIDWORKS 2016, and exported as *.STL files that were sliced for printing by Materialise Magics 20. The printing process was conducted in a laser powder bed Renishaw AM250 printer with SS 316L powder. During printing, a roller or wiper spread the SS powder uniformly over the build platform to form a powder bed, then the laser will selectively irradiate and melt the powder layer by layer (Figure 13b). This process took approximate only 1.4 h for 5 BPs. Conditions used during printing include laser power (200 W), focus offset (0 mm), layer thickness (50 μm), point spacing (60 μm), exposure time (80 μs), and hatch spacing (110 μm). The average beam velocity was 0.64 m/s, and a stripe melting mode (5 mm) was used. The BP surface was rough right after printing, and needed to be ground with grinding papers (SiC grindings paper #150-2400, BUEHLER).

4.4.2 Gold protective coating

For the gold electroplating on stainless steels, there are 3 steps, including electro-cleaning, electro-striking, and electro-plating. And the AM SS BPs received the negative charges during all the steps. During electro-cleaning, 4% solution of sodium hydroxide was heated to 60 ^{o}C to remove the contamination and oxide, and the SS BPs were immersed in the

solution as a cathode at 6 V and 60 ºC for 30 s. The surfaces of SS plates were totally hydrophilic with no water beads or breaks after the first step.

For electro-striking, TriVal - 24K Acid Gold Strike solution (TV128, Gold Plating Services) was used to pre-treat the SS surface at 7 V and 25 ºC for 45 s, shown in Figure 14a. In the solution, the pH was lower than 1, and the effective component was $KAu(CN)_4$, which allowed the electroreduction of gold occurred directly on the bare AM SS BP cathode electrode when the current was applied, and the reaction was as follows:

$$Au(CN)_4^- + 3e^- + 4H^+ \rightarrow Au + 4HCN \quad (4\text{-}3)$$

Then a thin gold layer with very faint yellow tint was adhesive to the AM SS BP surface, and it would be allowed to plate 24karat gold directly during electro-plating. For the next step, 24K Bright Gold Plating Solution (IG128, Gold Plating Services) was used to immerse the pre-treated plates and produce thicker gold layer on the previous mentioned thin layer at 2.7 V and 38 ºC for about 5 minutes, shown in Figure 13b. During this process, the pH was about 4 – 5, and the effective component was $KAu(CN)_2$ without free cyanide, which can produce the uniform deposit distribution, the reaction was as follows[58]:

$$Au(CN)_2^- + e^- + 2H^+ \rightarrow Au + 2HCN \quad (4\text{-}4)$$

4.4.3 Characterization and testing system

Scanning electron microscopy (SEM) was conducted with a field emission SEM JEOLJSM-6320F with an accelerating voltage of 0.5 – 30 kV, a magnification of 130 x~650,000 x and a 5-axis specimen mount. Energy-dispersive X-ray spectroscopy (EDS)

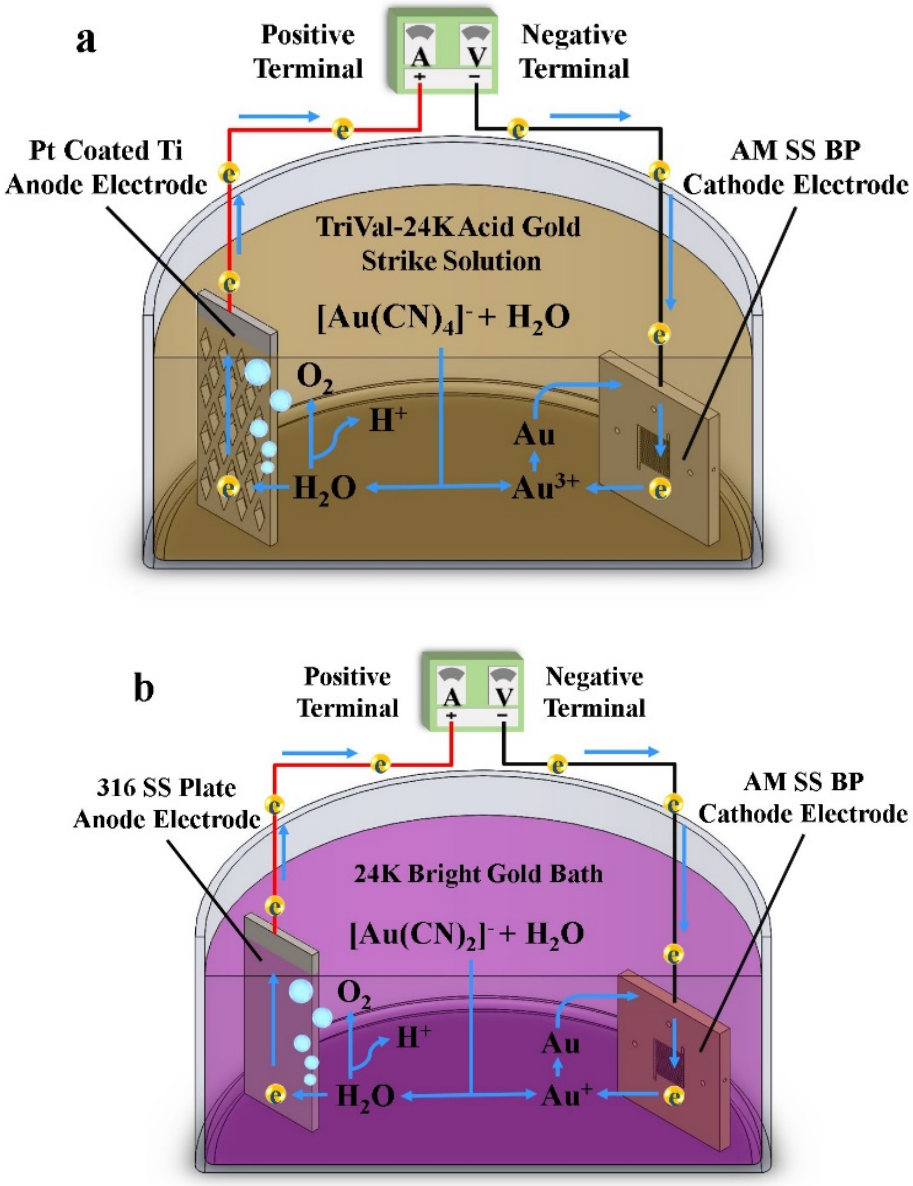

Figure 14. Schematics of (a) Gold striking on AM SS BP. (b) Gold plating on AM SS BP.

was performed with an EDAX Octane plus Silicon Drift Detector in tandem, which equipped with EDAX's TEAM EDS analysing software. X-ray diffraction (XRD) patterns were recorded with the Philips X'Pert materials research diffractometer with a 45 kV accelerating voltage and a 40 mA tube current with Cu Kα (λ = 1.5418 Å) as a radiation source. The scanning angle ranges from 20 ^{o} to 100 ^{o}.

ICR test was performed by using a test bed with Wang's method[43]. A hydraulic press (3912, CARVER INC.) was used to provide compression pressure which range from 0.7-2.4 MPa. A micro-ohmmeter (6250, AEMC INSTRUMENTS) with a resolution of 1μΩ was employed to record the total resistance of the set up. Toray 090 from FuelCellStore with a thickness of 280 μm and an electrical resistivity of 80 mΩ·cm was used as LGDLs. Copper plates were used to connect with CPs.

For all the PEMECs during the *in-situ* experiments, the CCMs were purchased from FuelCellsEtc, which contains a membrane made from Nafion® 115, with a 3.0 mg/cm^2 Iridium Ruthenium Oxide loaded anode CL, and a 3.0 mg/cm^2 Platinum Black loaded cathode CL. Titanium felts with the thickness of 350 μm and the porosity of 75% were used as LGDL at the anode side, while Toray 090 carbon papers (CPs) with thickness of 280 μm and porosity of 78% were employed at the cathode side. Machined polyvinyl chloride (PVC) sheets were used as gasket to seal LGDLs, and two end-plates were machined from commercial grade aluminium bulk. For the conventional PEMEC (cell 1), the graphite BPs were used at both the anode and cathode sides, since the anodic environment is too harsh for SS material, and two machined copper plates were used as

CD to distribute current to the graphite BPs. The Au-coated AM SS BPs were mounted into the anode side in AM PEMECs (cell 2 and cell 3), while the cell 2 and cell 3 have the bare AM SS BP and Au-coated AM SS BP at the cathode side, respectively. It should be mentioned CDs were not used in AM PEMECs, since the AM SS BPs can serve as both conventional BPs and CDs. Eight evenly distributed bolts compressed the cell with a torque of 4.52 N·m. Performance of the cells was carried out using a potentiostat SP-300 chassis with a 5 V/10 A booster from Bio-Logic.

The corrosion resistances of the Au-coated AM SS and AM SS samples were evaluated in a three-electrode assembly. The AM SS samples were printed with the same procedures mentioned before, then polished and amounted by epoxy resin to expose only one side of the samples, and the active area is 0.4 cm^2. Then one sample went through the electroplating procedures to form a gold protective layer. For the three-electrode assembly, the sample, a Pt foil, and a reversible hydrogen electrode (RHE) from BASInc served as the working electrode, counter electrode, and reference electrode, respectively. Both potentiodynamic and potentiostatic characteristics were gathered using a SP-300 chassis with a 5 V/10 A booster from Bio-Logic in pH2 H_2SO_4 solution bubbled with O_2 at 22 ^oC to simulate the anodic environment in PEMECs.

4.5 Results and discussion

4.5.1 Ex-situ measurements

The BPs right after printing are rough and full of tracks because of the melting pool

occurred during laser scanning, shown in Figure 15a and Figure 15d. Therefore, a polishing process is necessary, and the polished surface is smooth as shown in Figure 15b. To use the SS BP in an anodic environment, the polished BPs are coated with a thin layer of gold by electroplating to increase the corrosion resistance and the electrical conductivity, shown in Figure 15c. The Au-coated AM SS BPs are 0.5 cm (thick) × 6.0 cm (long) × 6.0 cm (wide) with an active area of 5 cm^2 after electroplating. The flow channel has a width of 1 mm, and the land has a width of 1 mm and a height of 1 mm. The cross-section of Au-coated AM SS BP is shown in Figure 15e with the corresponding EDS mapping in Figure 15f, which verify the gold-layer thickness of 1 um. The EDS result of AM SS BPs is shown in Figure 16a, which suggests the iron is the major element, and the element distribution is almost the same with the standard SS 316 L. Figure 16b shows the EDS of Au-coated AM SS BPs, and gold accounts for 94.13% of all the elements, which also agree with the mapping in Figure 16f. Besides, the EDS results of AM SS BPs and Au-coated AM SS BPs at different spots are consistent, respectively, which means the element distribution in the BPs are uniform. The XRD patterns of the standard 316L and AM SS BPs are shown in Figure 16c. Peaks in the Figure 16c indicate there is only SS 316L structure, which is the same with standard SS 316L, and the metal crystal structure does not change during laser melting process[59]. In addition, crystal structure of the gold layer by electroplating is shown in Figure 16d, which demonstrate the peak of Fe is comparatively small compared to that of Au which also shows the uniformity of Au throughout the surface of Au-coated AM SS plate, and the amount of Fe is small compared with Au.

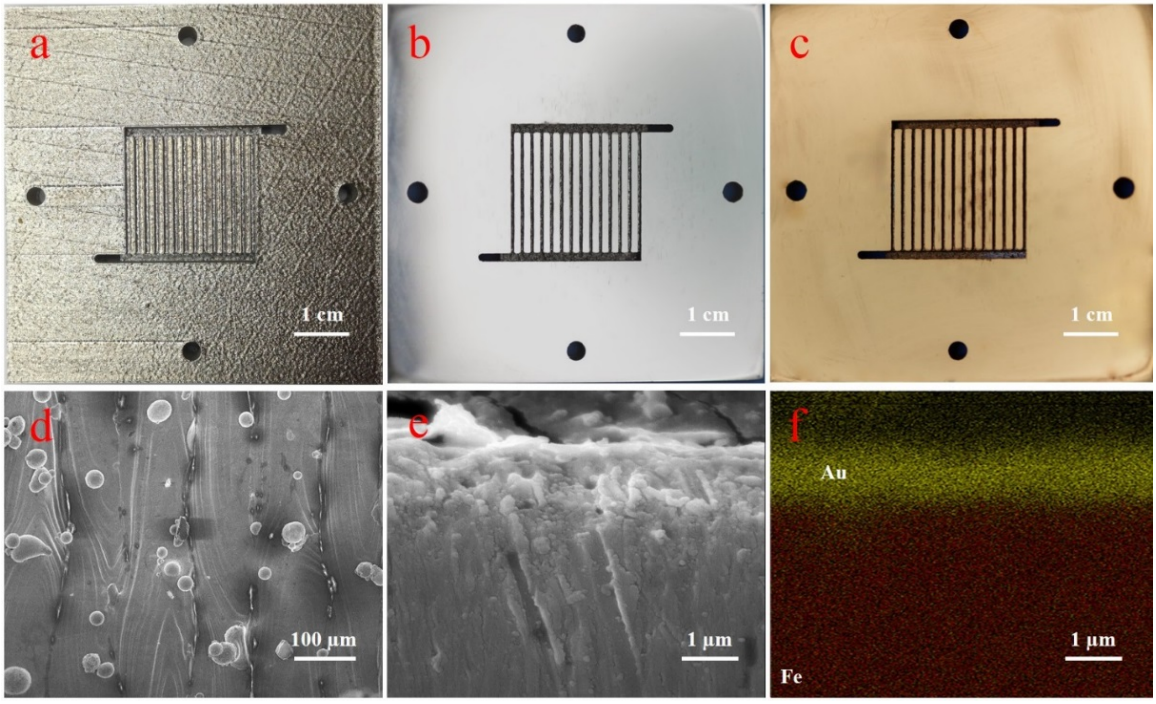

Figure 15. Photos of AM SS BPs (a) after printing, (b) after polishing, (c) and after electroplating. SEM images of AM SS BPs (d) after printing, (e) cross section of Au-coated AM SS BPs, and (f) the corresponding EDS mapping.

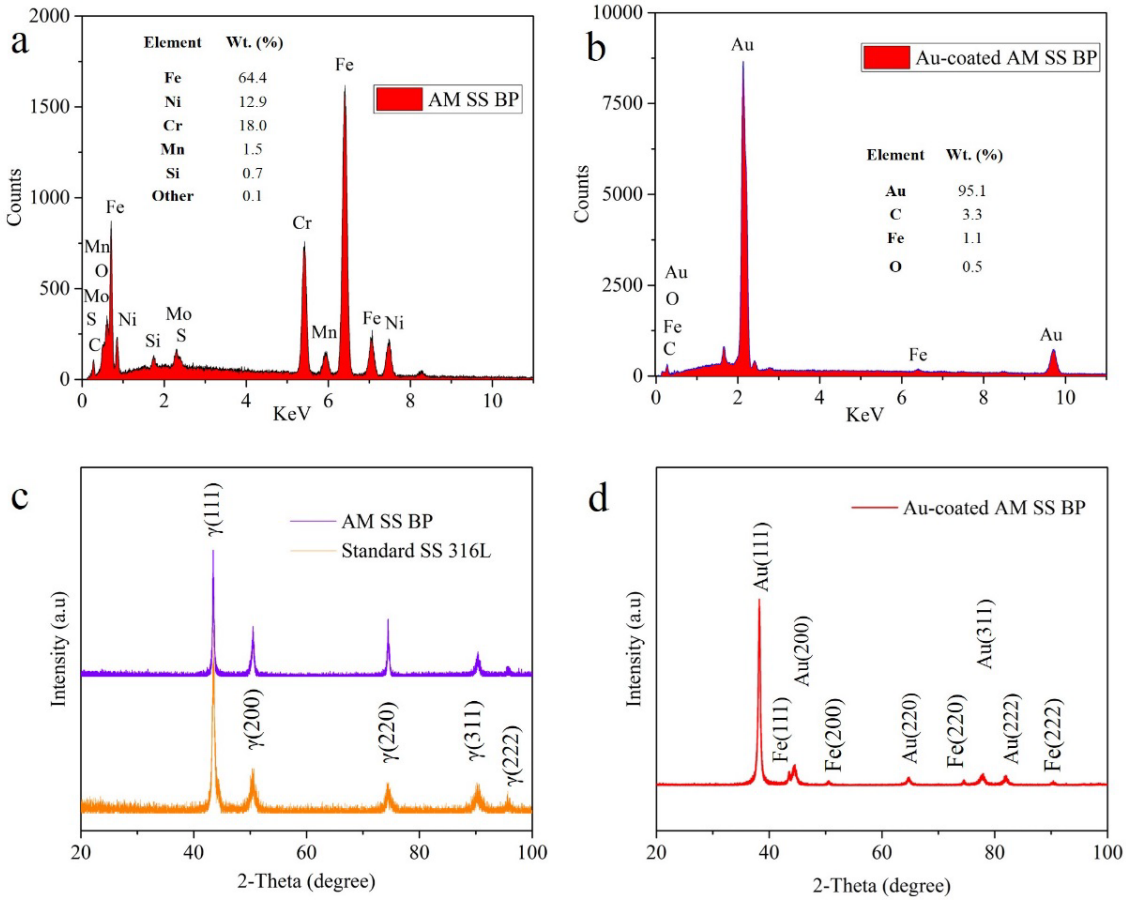

Figure 16. EDS of AM BP (a) before and (b) after electroplating. XRD images of (c) AM SS BP and standard SS 316L, and (d) AM SS BP after electroplating.

During ex-situ ICR tests, the total ohmic resistance includes the ICRs between mating parts and electronic resistance of each material. For AM SS PEMECs, the CD was excluded because of the multifunction of AM SS BPs, and the setup of ICR test is shown in Figure 17a. The total resistances in Setups 1 and 2 can be described as:

$$R_1 = R_{BP} + ICR_{BP\text{-}CP} + R_{CP} + ICR_{CP\text{-}Cu} + R_{Cu} \quad (4\text{-}5)$$

$$R_2 = R_{CP} + 2ICR_{CP\text{-}Cu} + 2R_{Cu} \quad (4\text{-}6)$$

Where R_1 and R_2 are the measured resistances of Setups 1 and 2, respectively, R_{BP}, R_{Cu} , R_{CP} are the electronic resistances of BP, copper electrode, and CP LGDL, respectively, $ICR_{BP\text{-}CP}$ and $ICR_{CP\text{-}Cu}$ are the ICR between BP and CP and ICR between CP and copper electrode, respectively. Then the ICR between BP and CP can be expressed as:

$$ICR_{BP\text{-}CP} = R_1 - R_{BP} - \frac{R_{CP}}{2} - \frac{R_2}{2} \quad (4\text{-}7)$$

Because the electronic resistance of the CP is relatively small compared with the ICR, R_{BP} and R_{CP} are neglected [60]. Equation (7) can be reduced to:

$$ICR_{BP\text{-}CP} \approx R_1 - \frac{R_2}{2} \quad (4\text{-}8)$$

Since there is a CD at each side of conventional PEMEC, and one electrode of the ohm-meter is connected with the CD, based on the same procedure we can calculate the total resistance of CD, graphite BP and CP with the equation:

$$R_{CD\text{-}BP\text{-}CP} \approx R_1 - \frac{R_2}{2} \quad (4\text{-}9)$$

Then the ICRs of different BPs with the increase of compression pressure are plotted in Figure 17b. ICR decreases with increasing compression pressure, which is due to the increase of effective contact area with the increasing pressure ICR is less sensitive to

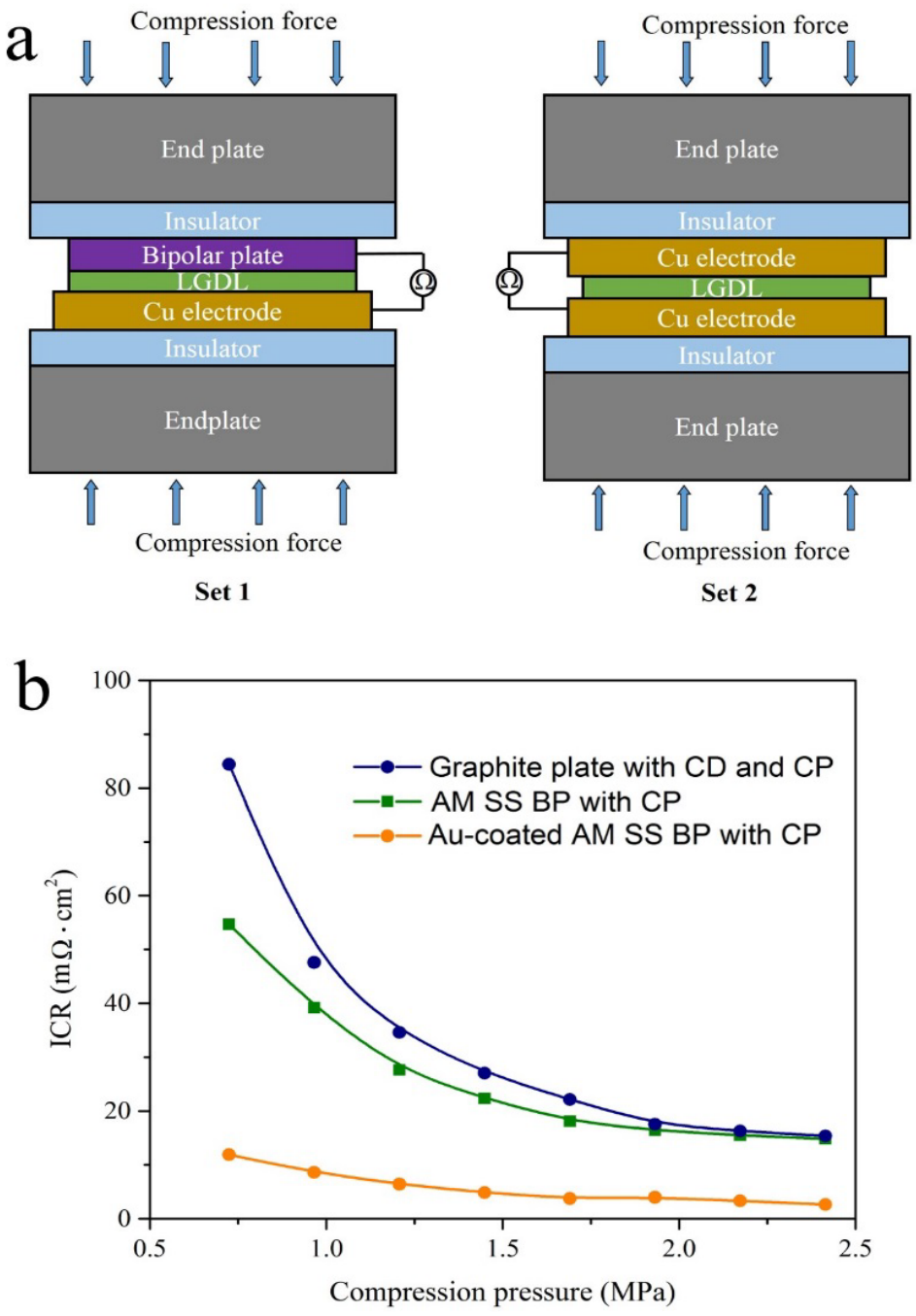

Figure 17. Setup schematics for ohmic resistance measurements (Set 1) and ICR measurements (Set 2). (b) Results of ICR measurements.

pressure when the pressure is high, because the effective contact area reaches a limit at high pressure. This also indicates a limit to using pressure to reduce ICR [61]. Most importantly, the Au-coated SS BPs show much lower IRC than bare AM SS BPs owing to the softness and high electrical conductivity of Au layer, which offer more effective contact area with CPs and less oxide scale compared with the SS materials[61, 62]. From the Au-coated AM SS result, the ICR using the Toray CP is about 6.4 $m\Omega \cdot cm^2$ under 1.45 MPa, which is much lower than the technical target of DOE: 20.0 $m\Omega \cdot cm^2$, while that of the bare SS BPs with CP and graphite BP with CD and CP are 22.3 and 27.0 $m\Omega \cdot cm^2$, respectively. [63] These results indicate that the Au layer can greatly decrease the ICR between the AM SS BP and CP, which will benefit the performance of PEMECs.

4.5.2 Polarization curves and EIS

To test the overall water splitting performance, the BPs are mounted in PEMECs to record the polarization curves and electrochemical impedance spectroscopy (EIS). For cell 1 (conventional PEMEC), the graphite BPs were used at both the anode and cathode sides, and two machined copper plates were used as the CDs. For cell 2 and cell 3, Au-coated AM SS BPs were mounted to the anode side, while the cell 2 and cell 3 have the bare AM SS BP and Au-coated AM SS BP at the cathode side, respectively. The polarization curves for current density from 0 to 2 A/cm^2 in Figure 18 are recorded for a scan rate of 100 mA/s at different temperatures, and the EIS results are scanned from 200 kHz to 30 mHz at 0.2 A/cm^2. As expected, the AM PEMECs (cells 2 and 3) show a pronounced improvement of performance compared with cell 1 in Figure 18a, and the working voltages of cell 1, 2, and

3 are 1.887 V, 1.752 V, and 1.707 V at 2 A/cm^2, respectively. Based on literatures, the total working voltage of PEMEC consists of theoretical equilibrium open circuit potential, activation overpotential to overcome the activation energy of the OER and HER on the catalyst surface, ohmic polarization to overcome the ohmic resistance through the PEMECs, and concentration polarization to overcome the mass transport limitation between CCMs and BPs[16, 64, 65]. In Figure 18a, the polarization curves at low current density region are almost the same for the three cells, which means those PEMECs share the similar activation overpotential with the same CCMs under same working conditions. But for 0.3 – 2 A/cm^2, the increase in voltage shows a nearly linear behavior, which indicates the ohmic potential dominates this region, so this improvement in performance is mainly due to a reduction of ohmic resistance. This reduction of ohmic resistance arises because the CDs were eliminated and Au layer were added to the AM PEMECs (cells 2 and 3).

Supporting evidence for a reduction of ohmic resistance is found in the EIS plots in Figure 18c. The leftmost intersection of the EIS curves at high frequency zone (2 kHz) is the ohmic resistance in the cell, and the rightmost intersection at low frequency zone (~38 mHz) is the total resistance. The difference between ohmic resistance and total resistance is the sum of activation resistance and concentration resistance[21, 37]. From Figure 18c, the sum of activation resistance and concentration resistance changes little for different PEMECs, while the ohmic resistance decreases from 0.198 mΩ·cm^2 for cell 3 to 0.095. mΩ·cm^2 for cell 1. This suggests that the reduction of ohmic resistance is a significant

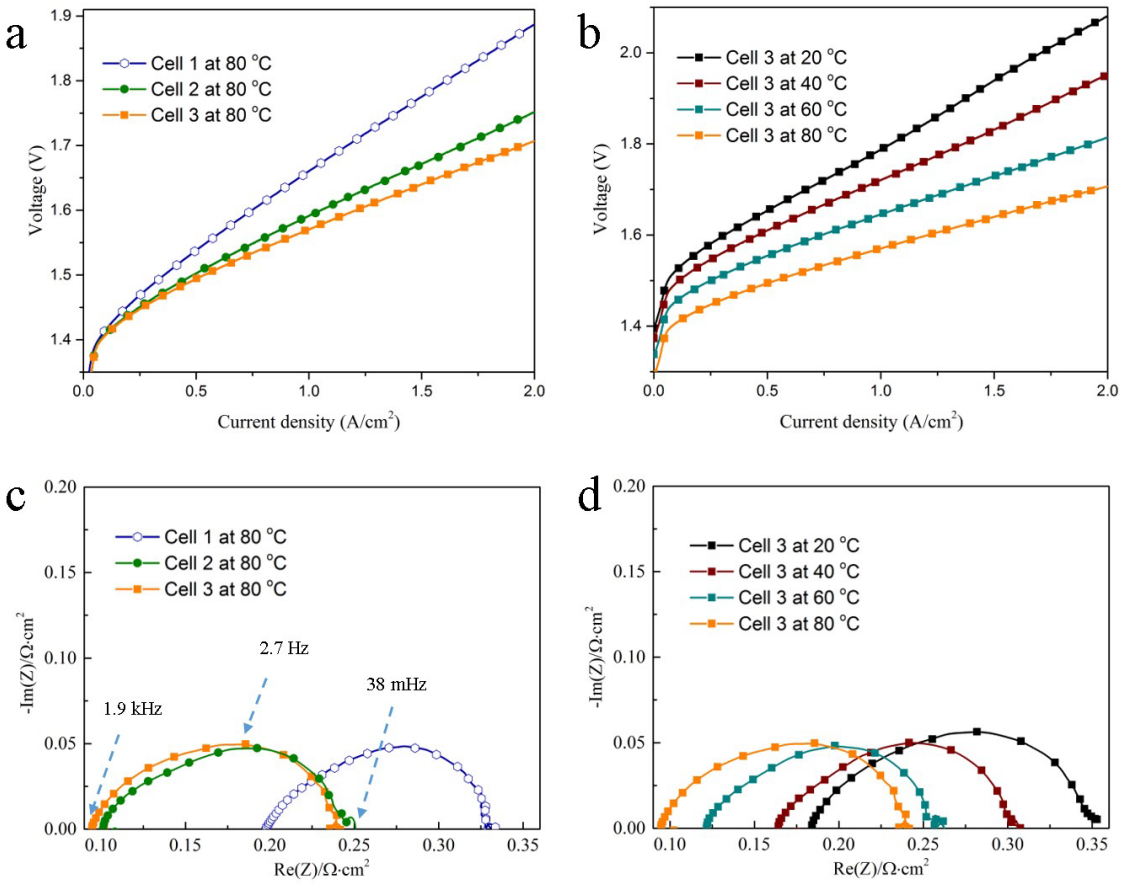

Figure 18. (a) Polarization curves and (c) EIS results of PEMECs with different cathode plates. (b) Polarization curves and (d) EIS results of PEMECs with AM integrated plates at different temperatures. The EIS results are recorded at the frequency range of 200 kHz to 30 mHz.

contributor to better performance for AM PEMECs

Moreover, cell 3 with Au-coated AM SS BPs at both sides shows a better performance than that of cell 2 with only an Au-coated BPs at the anode side. This might be because the Au coating layer reduces the ICR between AM SS BPs and CPs. Although the Au layer is not required to protect the material from corrosion at the cathode, it can increase the performance of PEMECs, and will save the feedstock and energy input during large scale hydrogen production[21]. Thus, the Au coating may be beneficial for the cathode BPs.

The influence of temperature on performance of cell 3 is investigated in Figure 18b, which shows the cell exhibits a lower voltage at higher temperature. The polarization curves at low current density region are lower for higher temperature, which suggests a smaller activation overpotential for higher temperature; at higher temperature, molecules have higher kinetic energies, and higher catalytic activity[5, 16, 21, 64]. Furthermore, the smaller slopes of the polarization curves at higher temperature and higher current density indicate smaller ohmic overpotential and resistances. With the increase of temperature, the proton conductivity of catalyst layer and Nafion membrane is improved, but also the components will have a greater thermal expansion, which will lead to higher compression pressure and lower ICR[48, 66, 67]. And the decease of ohmic resistance is also clearly shown as the left shift of intersection of EIS curves with X-axis in Figure 18.

4.5.3 Stability

The electrochemical behaviour of the AM SS BPs has been tested in a three-electrode assembly under simulated situations to investigate the corrosion resistance and stability of

the Au-coated AM SS BPs. The pH of the working environment of the anode BPs in PEMECs is about 2, hence, the tests have been performed under acidic (pH = 2) conditions at 20 ^{o}C bubbled with pure O_2. The tested samples are the AM SS cuboids with and without Au coating layers for comparisons. The inserted graph in Figure 19a shows the AM SS cuboid without Au coating at the center of a cylinder (plastic sample holder).. The potentiodynamic polarization curves of AM SS cubes are recorded with a scan rate of 1 mV/s. The corrosion potential of the AM SS sample is -0.25 V *vs.* reversible hydrogen electrode (RHE) in Figure 19a, followed by a steady passivation due to the oxide layer. While the Au coating layer provide a remarkable effect on the corrosion performance of the BPs, the corrosion potential of Au-coated AM SS sample is 0.13 V vs. RHE, which is much higher than that of bare AM SS sample. Since Au is one of the best corrosion resistance materials, it can passivate the AM SS substrate and moves the potential towards close to 0.13 V vs. RHE [60, 68]. The results indicate the Au coating layer provide a good corrosion resistance for the AM SS samples at high potential in the potentiodynamic tests.

To further evaluate the feasibility of Au-coating on the AM SS plate, potentiostatic measurements at 1.6 V *vs.* RHE were conducted to investigate the stability of Au-coated AM SS sample in a simulated anodic environment for 100 h, as shown in Figure 19b. From the potentiostatic polarization curves, the current density reduces fast in the initial 1 h followed by a slight increase and reaches a steady current finally. The initial decrease might due to the oxidation of other elements on the surface or the dissolution of iron in the acidic solution, because there are C and Fe in the coated layers, as shown in Figure 19b. Then the

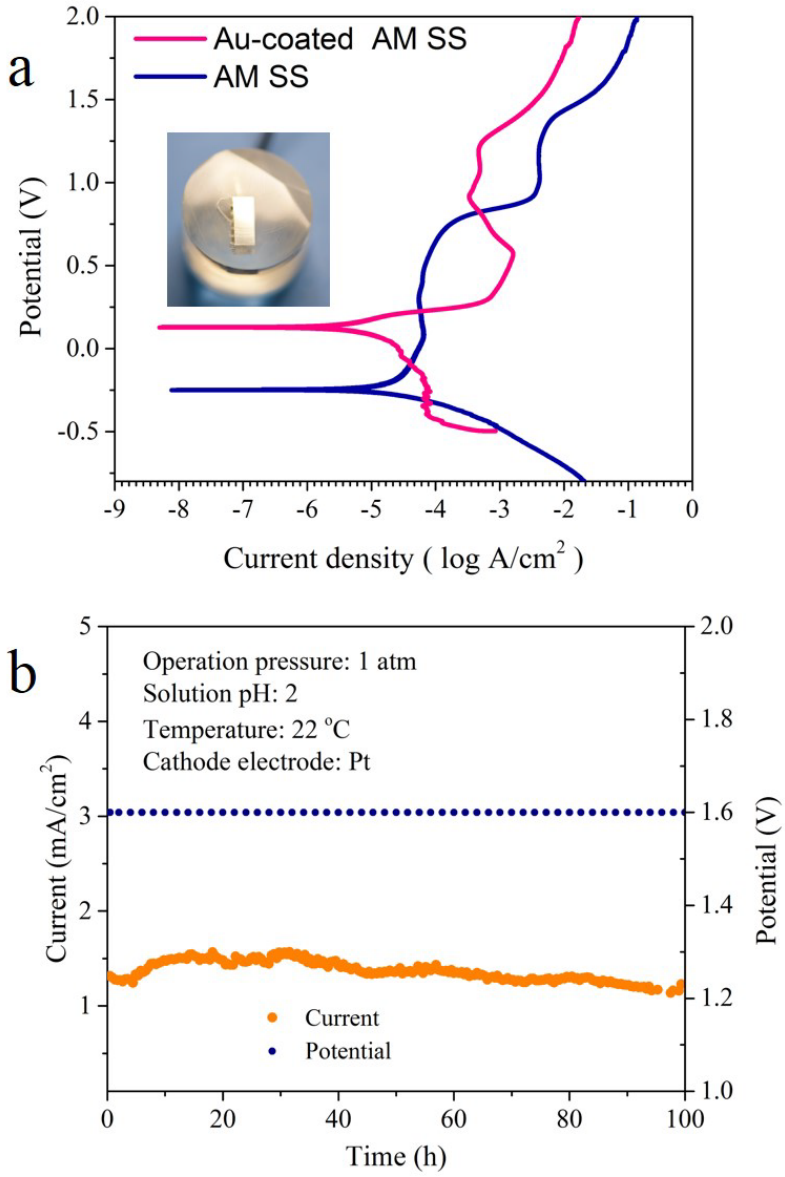

Figure 19. (a) Potentiodynamic polarization curves of AM SS BPs with and without Au-coating at a scanning rate of 50 mV/s. And (b) potentiostatic polarization curves of AM SS BPs with Au-coating over 100 h. Those tests are in pH2 H_2SO_4 solution bubbled with O_2 at 22 °C.

Au-coated AM SS sample presents a good stability. Therefore, the Au coating layer can enhance the corrosion resistance remarkably.

4.6 Conclusions

In summary, stainless steel bipolar plates are printed with the selective laser melting (SLM), then coated with thin film Au by an electroplating process to promote the corrosion resistance in an oxygen rich anodic ambient. To the best of our knowledge, this is the first time that AM SS BPs were used at both the cathode and anode sides for water splitting in PEMECs. The electrodes with SS BPs printed by AM at both sides possess a much lower ICR, 6.4 $m\Omega \cdot cm^2$ under 1.45 MPa, and a much lower voltage (higher efficiency), 1.71 V at 2 A/cm^2, compared to conventional electrodes with ohmic resistance of 17.0 $m\Omega \cdot cm^2$ and voltage of 1.887 V under the same operating conditions. The corrosion tests, conducted in a three-electrode assembly, demonstrate that the Au electroplated AM SS BPs have good corrosion resistance and good durability for 100 h under simulated acidic and high-voltage conditions. This research demonstrates that a protective coating enables the application of additively manufacturing of inexpensive materials on highly integrated PEMECs for low cost and efficient water splitting and hydrogen production. This approach can also be applied to other energy conversion devices.

References

[1] J. A. Turner, "Sustainable hydrogen production," *Science,* vol. 305, pp. 972-974, 2004.

[2] V. R. Stamenkovic, D. Strmcnik, P. P. Lopes, and N. M. Markovic, "Energy and fuels from electrochemical interfaces," *Nature Materials,* vol. 16, pp. 57-69, 2017.

[3] R. Hornung and G. Kappelt, "Bipolar plate materials development using Fe-based alloys for solid polymer fuel cells," *Journal of Power Sources,* vol. 72, pp. 20-21, 1998.

[4] T. Reier, H. N. Nong, D. Teschner, R. Schlögl, and P. Strasser, "Electrocatalytic Oxygen Evolution Reaction in Acidic Environments–Reaction Mechanisms and Catalysts," *Advanced Energy Materials,* 2016.

[5] M. Carmo, D. L. Fritz, J. Mergel, and D. Stolten, "A comprehensive review on PEM water electrolysis," *International Journal of Hydrogen Energy,* vol. 38, pp. 4901-4934, 2013.

[6] C. Minke, T. Hickmann, A. R. dos Santos, U. Kunz, and T. Turek, "Cost and performance prospects for composite bipolar plates in fuel cells and redox flow batteries," *Journal of Power Sources,* vol. 305, pp. 182-190, 2016.

[7] M. A. Pellow, C. J. Emmott, C. J. Barnhart, and S. M. Benson, "Hydrogen or batteries for grid storage? A net energy analysis," *Energy & Environmental Science,* vol. 8, pp. 1938-1952, 2015.

[8] L. Cindrella, A. Kannan, J. Lin, K. Saminathan, Y. Ho, C. Lin*, et al.*, "Gas diffusion layer for proton exchange membrane fuel cells—A review," *Journal of Power Sources,* vol. 194, pp. 146-160, 2009.

[9] H.-Y. Jung, S.-Y. Huang, P. Ganesan, and B. N. Popov, "Performance of gold-coated titanium bipolar plates in unitized regenerative fuel cell operation," *Journal of Power Sources,* vol. 194, pp. 972-975, 2009.

[10] B. Martindale and E. Reisner, "Bi-Functional Iron-Only Electrodes for Efficient Water Splitting with Enhanced Stability through In Situ Electrochemical Regeneration," *Advanced Energy Materials,* vol. 6, 2016.

[11] B. Pivovar, N. Rustagi, and S. Satyapal, "Hydrogen at Scale (H2@Scale) Key to a Clean, Economic, and Sustainable Energy System," *The Electrochemical Society Interface,* vol. 27, pp. 67-72, 2018.

[12] S. Grigoriev, P. Millet, and V. Fateev, "Evaluation of carbon-supported Pt and Pd nanoparticles for the hydrogen evolution reaction in PEM water electrolysers," *Journal of Power Sources,* vol. 177, pp. 281-285, 2008.

[13] L. Timperman, A. S. Gago, and N. Alonso-Vante, "Oxygen reduction reaction increased tolerance and fuel cell performance of Pt and RuxSey onto oxide–carbon composites," *Journal of Power Sources,* vol. 196, pp. 4290-4297, 2011.

[14] A. Sternberg and A. Bardow, "Power-to-What?–Environmental assessment of energy storage systems," *Energy & Environmental Science,* vol. 8, pp. 389-400, 2015.

[15] K. E. Ayers, E. B. Anderson, C. Capuano, B. Carter, L. Dalton, G. Hanlon*, et al.*, "Research advances towards low cost, high efficiency PEM electrolysis," *ECS Transactions,* vol. 33, pp. 3-15, 2010.

[16] Z. Kang, J. Mo, G. Yang, S. T. Retterer, D. A. Cullen, T. J. Toops*, et al.*, "Investigation of thin/well-tunable liquid/gas diffusion layers exhibiting superior multifunctional performance in low-temperature electrolytic water splitting," *Energy & Environmental Science,* vol. 10, pp. 166-175, 2017.

[17] G. Yang, J. Mo, Z. Kang, Y. Dohrmann, F. A. List, J. B. Green*, et al.*, "Fully printed and integrated electrolyzer cells with additive manufacturing for high-efficiency water splitting," *Applied Energy,* vol. 215, pp. 202-210, 2018.

[18] Z. Kang, G. Yang, J. Mo, Y. Li, S. Yu, D. A. Cullen*, et al.*, "Novel Thin/Tunable Gas Diffusion Electrodes with Ultra-Low Catalyst Loading for Hydrogen Evolution Reactions in Proton Exchange Membrane Electrolyzer Cells," *Nano Energy,* 2018.

[19] J. Russell, L. Nuttall, and A. Fickett, "Hydrogen generation by solid polymer electrolyte water electrolysis," *American Chemical Society Division of Fuel Chemistry Preprints,* vol. 18, p. 24e40, 1973.

[20] J. R. Hudkins, D. G. Wheeler, B. Peña, and C. P. Berlinguette, "Rapid prototyping of electrolyzer flow field plates," *Energy & Environmental Science,* 2016.

[21] G. Yang, J. Mo, Z. Kang, F. A. List, J. B. Green, S. S. Babu*, et al.*, "Additive manufactured bipolar plate for high-efficiency hydrogen production in proton

exchange membrane electrolyzer cells," *International Journal of Hydrogen Energy,* vol. 42, pp. 14734-14740, 2017.

[22] J. W. Pratt, L. E. Klebanoff, K. Munoz-Ramos, A. A. Akhil, D. B. Curgus, and B. L. Schenkman, "Proton exchange membrane fuel cells for electrical power generation on-board commercial airplanes," *Applied energy,* vol. 101, pp. 776-796, 2013.

[23] B. Yang, M. P. Brady, H. Wang, J. Turner, K. L. More, D. J. Young*, et al.*, "Protective nitride formation on stainless steel alloys for proton exchange membrane fuel cell bipolar plates," *Journal of Power Sources,* vol. 174, pp. 228-236, 2007.

[24] Z. Kang, J. Mo, G. Yang, Y. Li, D. A. Talley, B. Han*, et al.*, "Performance Modeling and Current Mapping of Proton Exchange Membrane Electrolyzer Cells with Novel Thin/Tunable Liquid/Gas Diffusion Layers," *Electrochimica Acta,* vol. 255, pp. 405-416, 2017.

[25] A. Gago, S. Ansar, B. Saruhan, U. Schulz, P. Lettenmeier, N. Cañas*, et al.*, "Protective coatings on stainless steel bipolar plates for proton exchange membrane (PEM) electrolysers," *Journal of Power Sources,* vol. 307, pp. 815-825, 2016.

[26] M. Langemann, D. L. Fritz, M. Müller, and D. Stolten, "Validation and characterization of suitable materials for bipolar plates in PEM water electrolysis," *International journal of hydrogen energy,* vol. 40, pp. 11385-11391, 2015.

[27] J. Mo, Z. Kang, G. Yang, S. T. Retterer, D. A. Cullen, T. J. Toops, *et al.*, "Thin liquid/gas diffusion layers for high-efficiency hydrogen production from water splitting," *Applied Energy,* vol. 177, pp. 817-822, 2016.

[28] P. Lettenmeier, R. Wang, R. Abouatallah, B. Saruhan, O. Freitag, P. Gazdzicki, *et al.*, "Low-Cost and Durable Bipolar Plates for Proton Exchange Membrane Electrolyzers," *Scientific Reports,* vol. 7, p. srep44035, 2017.

[29] X. Li, X. Hao, A. Abudula, and G. Guan, "Nanostructured catalysts for electrochemical water splitting: current state and prospects," *Journal of Materials Chemistry A,* vol. 4, pp. 11973-12000, 2016.

[30] J. Mo, R. R. Dehoff, W. H. Peter, T. J. Toops, J. B. Green, and F.-Y. Zhang, "Additive manufacturing of liquid/gas diffusion layers for low-cost and high-efficiency hydrogen production," *International Journal of Hydrogen Energy,* 2016.

[31] J. Mo, Z. Kang, S. T. Retterer, D. A. Cullen, T. J. Toops, J. B. Green Jr, *et al.*, "Discovery of true electrochemical reactions for ultrahigh catalyst mass activity in water splitting," *Science Advances,* 2016.

[32] J. Xu, D. Aili, Q. Li, E. Christensen, J. O. Jensen, W. Zhang, *et al.*, "Oxygen evolution catalysts on supports with a 3-D ordered array structure and intrinsic proton conductivity for proton exchange membrane steam electrolysis," *Energy & Environmental Science,* vol. 7, pp. 820-830, 2014.

[33] N. Li, W.-Y. Xia, J. Wang, Z.-L. Liu, Q.-Y. Li, S.-Z. Chen, *et al.*, "Manganese oxides supported on hydrogenated TiO 2 nanowire array catalysts for the

electrochemical oxygen evolution reaction in water electrolysis," *Journal of Materials Chemistry A,* vol. 3, pp. 21308-21313, 2015.

[34] B. H. Suryanto, X. Lu, and C. Zhao, "Layer-by-layer assembly of transparent amorphous Co 3 O 4 nanoparticles/graphene composite electrodes for sustained oxygen evolution reaction," *Journal of Materials Chemistry A,* vol. 1, pp. 12726-12731, 2013.

[35] A. Gago, D. Morales-Acosta, L. Arriaga, and N. Alonso-Vante, "Carbon supported ruthenium chalcogenide as cathode catalyst in a microfluidic formic acid fuel cell," *Journal of Power Sources,* vol. 196, pp. 1324-1328, 2011.

[36] W. A. Rigdon and X. Huang, "Carbon monoxide tolerant platinum electrocatalysts on niobium doped titania and carbon nanotube composite supports," *Journal of Power Sources,* vol. 272, pp. 845-859, 2014.

[37] Z. Kang, J. Mo, G. Yang, Y. Li, D. A. Talley, S. T. Retterer*, et al.*, "Thin film surface modifications of thin/tunable liquid/gas diffusion layers for high-efficiency proton exchange membrane electrolyzer cells," *Applied Energy,* vol. 206, pp. 983-990, 2017.

[38] Y. Qin, Q. Du, Y. Yin, K. Jiao, and X. Li, "Numerical investigation of water dynamics in a novel proton exchange membrane fuel cell flow channel," *Journal of Power Sources,* vol. 222, pp. 150-160, 2013.

[39] L. Bertuccioli, A. Chan, D. Hart, F. Lehner, B. Madden, and E. Standen, "Study on development of water electrolysis in the EU," *Final report in fuel cells and hydrogen joint undertaking,* 2014.

[40] X. Li and I. Sabir, "Review of bipolar plates in PEM fuel cells: Flow-field designs," *International Journal of Hydrogen Energy,* vol. 30, pp. 359-371, 2005.

[41] J. Park and X. Li, "Effect of flow and temperature distribution on the performance of a PEM fuel cell stack," *Journal of Power Sources,* vol. 162, pp. 444-459, 2006.

[42] H. Wang, M. P. Brady, G. Teeter, and J. Turner, "Thermally nitrided stainless steels for polymer electrolyte membrane fuel cell bipolar plates: Part 1: Model Ni–50Cr and austenitic 349™ alloys," *Journal of Power Sources,* vol. 138, pp. 86-93, 2004.

[43] H. Wang, M. A. Sweikart, and J. A. Turner, "Stainless steel as bipolar plate material for polymer electrolyte membrane fuel cells," *Journal of Power Sources,* vol. 115, pp. 243-251, 2003.

[44] B. Cunningham and D. G. Baird, "The development of economical bipolar plates for fuel cells," *Journal of Materials Chemistry,* vol. 16, pp. 4385-4388, 2006.

[45] G. Scotti, V. Matilainen, P. Kanninen, H. Piili, A. Salminen, T. Kallio*, et al.*, "Laser additive manufacturing of stainless steel micro fuel cells," *Journal of Power Sources,* vol. 272, pp. 356-361, 2014.

[46] P. Lettenmeier, R. Wang, R. Abouatallah, F. Burggraf, A. Gago, and K. Friedrich, "Coated Stainless Steel Bipolar Plates for Proton Exchange Membrane

Electrolyzers," *Journal of The Electrochemical Society,* vol. 163, pp. F3119-F3124, 2016.

[47] U. Babic, M. Suermann, F. N. Büchi, L. Gubler, and T. J. Schmidt, "Critical Review—Identifying Critical Gaps for Polymer Electrolyte Water Electrolysis Development," *Journal of The Electrochemical Society,* vol. 164, pp. F387-F399, 2017.

[48] Y. Wang, K. S. Chen, J. Mishler, S. C. Cho, and X. C. Adroher, "A review of polymer electrolyte membrane fuel cells: technology, applications, and needs on fundamental research," *Applied energy,* vol. 88, pp. 981-1007, 2011.

[49] G. Scotti, P. Kanninen, V.-P. Matilainen, A. Salminen, and T. Kallio, "Stainless steel micro fuel cells with enclosed channels by laser additive manufacturing," *Energy,* vol. 106, pp. 475-481, 2016.

[50] M. Li, S. Luo, C. Zeng, J. Shen, H. Lin, and C. n. Cao, "Corrosion behavior of TiN coated type 316 stainless steel in simulated PEMFC environments," *Corrosion science,* vol. 46, pp. 1369-1380, 2004.

[51] G. Chisholm, P. J. Kitson, N. D. Kirkaldy, L. G. Bloor, and L. Cronin, "3D printed flow plates for the electrolysis of water: an economic and adaptable approach to device manufacture," *Energy & Environmental Science,* vol. 7, pp. 3026-3032, 2014.

[52] G. Yang, J. Mo, Z. Kang, Y. Dohrmann, J. B. Green Jr, S. S. Babu*, et al.*, "Fully printed and integrated electrolyzer cells with additive manufacturing for high-

efficiency water splitting," *Applied Energy,* vol. 215, pp. 202–210, 1 April 2018 2018.

[53] N. De las Heras, E. Roberts, R. Langton, and D. Hodgson, "A review of metal separator plate materials suitable for automotive PEM fuel cells," *Energy & Environmental Science,* vol. 2, pp. 206-214, 2009.

[54] J. Park, H. Oh, T. Ha, Y. I. Lee, and K. Min, "A review of the gas diffusion layer in proton exchange membrane fuel cells: durability and degradation," *Applied Energy,* vol. 155, pp. 866-880, 2015.

[55] C. Wang and Y. Tao, "Coatings for Robust Metal Bipolar Plates," *ECS Transactions,* vol. 64, pp. 909-915, 2014.

[56] H. Tawfik, Y. Hung, and D. Mahajan, "Metal bipolar plates for PEM fuel cell—a review," *Journal of Power Sources,* vol. 163, pp. 755-767, 2007.

[57] L. Lei, Y. Wang, S. Fang, C. Ren, T. Liu, and F. Chen, "Efficient syngas generation for electricity storage through carbon gasification assisted solid oxide co-electrolysis," *Applied Energy,* vol. 173, pp. 52-58, 2016.

[58] N. D. Ket, T. Van Chung, V. M. Thanh, N. D. Ha, and L. Q. Tuan, "A NOVEL STUDY OF ELECTRO-REDUCTION OF GOLD CYANIDE COMPLEX IONS Au (CN) 2-IN WEAK ACIDIC SOLUTION," *International Journal of Pharmaceutical, Chemical & Biological Sciences,* vol. 6, 2016.

[59] Y. Wang and D. O. Northwood, "An investigation into TiN-coated 316L stainless steel as a bipolar plate material for PEM fuel cells," *Journal of Power Sources,* vol. 165, pp. 293-298, 2007.

[60] W. Yoon, X. Huang, P. Fazzino, K. L. Reifsnider, and M. A. Akkaoui, "Evaluation of coated metallic bipolar plates for polymer electrolyte membrane fuel cells," *Journal of Power Sources,* vol. 179, pp. 265-273, 2008.

[61] D. Zhang, L. Duan, L. Guo, and W.-H. Tuan, "Corrosion behavior of TiN-coated stainless steel as bipolar plate for proton exchange membrane fuel cell," *International Journal of Hydrogen Energy,* vol. 35, pp. 3721-3726, 2010.

[62] Y.-H. Yun, "Deposition of gold–titanium and gold–nickel coatings on electropolished 316L stainless steel bipolar plates for proton exchange membrane fuel cells," *international journal of hydrogen energy,* vol. 35, pp. 1713-1718, 2010.

[63] H. Zhang, M. Hou, G. Lin, Z. Han, Y. Fu, S. Sun*, et al.*, "Performance of Ti–Ag-deposited titanium bipolar plates in simulated unitized regenerative fuel cell (URFC) environment," *international journal of hydrogen energy,* vol. 36, pp. 5695-5701, 2011.

[64] M. M. Mench, *Fuel cell engines*: John Wiley & Sons, 2008.

[65] B. Han, J. Mo, Z. Kang, G. Yang, W. Barnhill, and F.-Y. Zhang, "Modeling of two-phase transport in proton exchange membrane electrolyzer cells for hydrogen energy," *International Journal of Hydrogen Energy,* vol. 42, pp. 4478-4489, 2017.

[66] P. Millet, N. Mbemba, S. Grigoriev, V. Fateev, A. Aukauloo, and C. Etiévant, "Electrochemical performances of PEM water electrolysis cells and perspectives," *International Journal of Hydrogen Energy,* vol. 36, pp. 4134-4142, 2011.

[67] T. E. Springer, T. Zawodzinski, and S. Gottesfeld, "Polymer electrolyte fuel cell model," *Journal of the Electrochemical Society,* vol. 138, pp. 2334-2342, 1991.

[68] A. Kumar, M. Ricketts, and S. Hirano, "Ex situ evaluation of nanometer range gold coating on stainless steel substrate for automotive polymer electrolyte membrane fuel cell bipolar plate," *Journal of Power Sources,* vol. 195, pp. 1401-1407, 2010.

CHAPTER V

A NOVEL PEMEC WITH 3D PRINTED NON-CONDUCTIVE BIPOLAR PLATE FOR LOW-COST HYDROGEN PRODUCTION FROM WATER ELECTROLYSIS

This chapter will be further edited and submitted for publication

I am fully responsible for the work submitted in this chapter, contributions from co-authors will be added prior to submission for publication.

5.1 Abstract

For establishing the large-scale hydrogen production as energy carrier from water electrolysis, improving cost-effectiveness and efficiency remains the main challenges. In this study, we propose a novel proton exchange membrane electrolyzer cell (PEMEC), consisting of non-conductive bipolar plates (BPs) and thin film liquid/gas diffusion layers (TF-LGDLs) to reduce the cost and improve the PEMEC performance. The 3D printed non-conductive BP is manufactured with low-cost polylactic acid (PLA) and is mainly functioned to distribute the water and gas products. A titanium thin film LGDL (TF-LGDL) with surroundings is developed for directly transporting electrons from the external power sources, which changes the electron transport path in the PEMECs. The PLA BP exhibits an extremely low cost (1/10 of that of the graphite BP), and the hydrogen production rate per unit BP cost in a PEMEC with PLA BP, is almost 6 times higher than a conventional one with graphite BPs. More importantly, the PEMECs with PLA BPs can achieve a good electrochemical performance of 2.21 V at 1 A/cm^{2}under room temperature. A model is also developed to investigate the impact of the BP resistivity of on the cell performance, and a threshold value of 0.433 Ω·cm is also calculated for the selection guideline of conductivity of BPs material. The easily accessible and low-cost PLA BPs coupled with the new

electron-conducting path will drive the exploration of plastic materials for economic and efficient water splitting or other energy conversion devices.

5.2 Introduction

Hydrogen is considered as an environmentally friendly renewable substitute for conventional fossil energy resources, and has attracted extensive attention, since it can provide 2.5 times more energy per unit mass than fossil energy, and provide hazard-free products.[1-7] Nowadays, the hydrogen is mainly generated by steam reforming of fossil fuel or coal gasification, which will cause toxic gas emission[8, 9]. Water splitting is one of the most convenient methods for hydrogen production as energy storage from off-peak electricity and other intermittent renewable energy resources, like wind, solar, and et.al[10-15]. Proton exchange membrane water splitting (PEMWS), developed by Russell in 1973, provides a number of advantages: high purity products, high working current density, and high operation pressure[5, 16]. So far, the use of H_2 as large-scale storage from water electrolysis has not been established, as a result of high cost of proton exchange membrane electrolyzer cell (PEMEC) stacks, and high electrical energy cost [17].

In order to commercialize the large-scale hydrogen production via PEMWS, two approaches can be used to reduce the hydrogen production costs from PEMECs. First of all, the cost of components need to be decreased, so that the capital expenditure can be decreased[5, 17]. The conventional PEMEC mainly consists of a catalyst coated membrane (CCM), two bipolar plates (BPs) and liquid/gas diffusion layers (LGDLs) at anode and cathode sides, shown in Figure 20[14, 18-23]. At anode side, the water diffuses from BP

to catalyst layer through LGDL, and is split into protons, oxygen and electrons. Electrons transport from catalyst layer to BP through the LGDL, and protons transport from anode to cathode catalyst layer through PEM. At cathode, the electrons transport from BP though LGDL to catalyst layer, then react with protons to form hydrogen. BPs, also called separator plates, are one of the most important components in PEMEC stacks. They usually conduct electrons in through-plane direction, distribute water and product gas to or from LGDL and catalyst layer, and provide mechanical support for the cells[24, 25]. BPs are usually made of graphite, stainless steel (SS), and titanium[26]. And the material cost and manufacturing expenditure make them the most costly components in PEMECs. BPs can attribute up to 50% cost and 60% weight of PEMECs[15, 17, 27-30]. For a 13 kg/day Electrolyzer, the stacks account for over half capital cost, and the BPs represent 48% of the stack cost[31].

With the purpose of reducing the cost of BPs, cheaper materials like aluminum, SS and copper were used, but those material will be easily corroded at highly oxidative anode environment[17, 32]. So corrosion resistant coating layers are usually required to protect those materials. Commonly used coatings for BPs are carbon-based and metal-based materials. Carbon-based coating materials include graphite, conductive polymer, diamond like carbon. And metal-based coating materials include noble metals, metal nitrides, metal carbides[32]. But those coating processes also increase the additional costs of BPs. Researches tried to fabricate BPs with additive manufacturing (AM) to lessen the cost. Plastic materials with advantages of high corrosion resistance and cheap price, have

attracted attentions for the development of BPs. Cronin's group developed a silver-coated plastic AM BPs from polypropylene, and Berlinguette's group introduced nickel onto composite polylactic acid (PLA) BPs [16, 33]. Those methods provided a light weight and low-cost manufacturing process, but the coating processes offset it low cost, and the performance (>2.40 V at 1 A/cm^2) was not comparable to that with metallic or graphite BPs. Zhang's group proposed AM BPs from SS using selective laser melting[15, 25, 27]. The AM BPs achieved a good performance, and this AM method lessened the weight and fabrication time of BPs with the capability of producing complex flow channel easily. Nevertheless, this method still did not break the limit of BP cost as a result of fabricating with metallic materials. Several other groups tried to produce BPs with carbon-based composite material for water electrolysis or fuel cell, but those BPs need complex manufacturing processes, and the brittleness is also a problem[34-36]. Therefore, a BP with simple manufacturing process and low-cost material is still desirable to lower the price of hydrogen production.

Second possibility to reduce the hydrogen production costs is improving the performance and efficiency of PEMECs. In PEMECs, the overall overpotential mainly includes activation overpotential and ohmic overpotential at the current range of water electrolysis (0 – 2 A/cm^2), and the mass transport overpotential can be neglected[37]. Therefore, one way to improve the performance is to reduce the ohmic resistance, especially the interfacial contact resistance (ICR)[38, 39]. Yang et.al. integrated BP with LGDL, current distributor and gasket using selective laser melting. Consequently, ICR

between those parts were eliminated, and the energy efficiency of the AM PEMEC reached up to 86.48% at 2 A/cm^2 [15, 40]. Kang et.al developed a novel titanium thin/tunable liquid/gas diffusion layer (TT-LGDL), which also resulted in the reduction of the ohmic and activation losses during water electrolysis [19, 21]. Also the coating aforementioned can modify the surface morphology, diminish the ICR between mating parts, and increase the lifetime of BPs[21, 41, 42]. Another way is to decrease the activation overpotential by developing novel electro-catalysts. So far, numerous of researches focused on the development of high-activity electrocatalyst for oxygen and hydrogen evolution reactions, such as nonprecious metal oxides [43-46]. Even those new invented catalysts can achieve a good catalytic activity, but the durability is not acceptable, and further researches are still needed.

In this paper, the purpose is simplifying the BP fabrication process, reducing the BP cost and enhancing the performance of PEMECs. We developed 3D printed plastic BPs using fused deposition modeling (FDM) without other post-processes (Figure 20a). The non-conductive PLA BPs are only used for mass distribution and mechanical support, and compared with the conductive graphene PLA (CGPLA) BPs. A novel Ti thin film LGDL (TF-LGDL) was fabricated using wet-etching for electron conducting and mass diffusing (Figure 20b). Most importantly, the electrons are conducted laterally (in-plane) from outside to the CL (Figure 20d), while the conventional electron-conducting path is through the plane of BPs and LGDLs (Figure 20c). Therefore, the PLA BPs are bypassed from the electron-conducting path, which allow the use of non-conductive PLA as BP material.

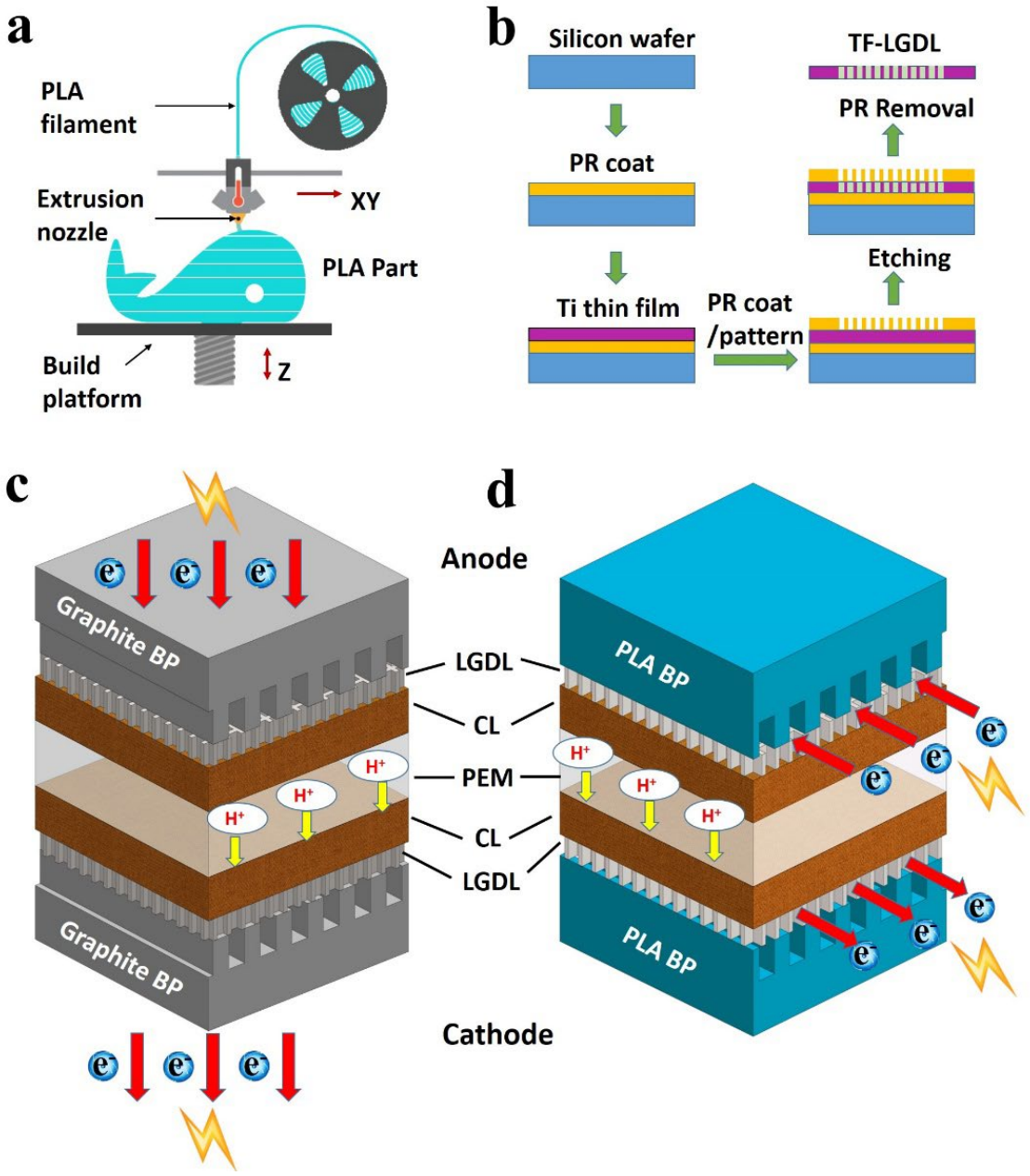

Figure 20. Schematic of (a) manufacturing non-conductive PLA BP with FDM, and (b) wet etching process for developing TF-LGDL. Configuration and electron-conducting path of (c) conventional PEMEC and (d) PEMEC with PLA BPs.

From the analysis, the cost of PLA BPs drops to 1/10 of that of the graphite BP. The PEMEC with PLA BP achieves a relatively low voltage of 2.21 V at 1 A/cm^2, and a good stability with a degradation rate of 1.03 mV/h. In addition, a simulation model is developed to investigate the impact of resistivity of BPs on the cell performance, and a threshold value is provided.

5.3 Experimental details

The BPs were designed using SOLIDWORKS 2017, and exported as *.STL files, then were processed and sliced in Cura 2.0 for printing. For non-conductive PLA BPs, PLA filament (NFC PLA, Ultimaker) with a diameter of 2.85mm was used in a 3D Printer (Ultimaker 2, Ultimaker), and the nozzle diameter was 4 mm. The printing was at light infill (20%) mode, and the printing time is 5 h 58 min. For the CGPLA BPs, CGPLA filament (GRPHN-PLA, Blackmagic3d) was used at solid infill (100%) mode to enhance the electrical conductivity, and the printing time is 10 h 16 min. During the printing, the filaments were supplied into the extrusion nozzle, then melted and extruded on the platform (Figure 20a). The movement of nozzle at XY direction resulted in the sliced pattern at the specified height. And the movement of build platform (Z direction) allowed the printing layer by layer. Other printing parameters included layer height (0.06mm), printing temperature (195 ^{o}C), build plate temperature (60 ^{o}C), and printing head speed (60 mm/s). The surfaces of BPs after printing were rough and not suitable for directly using in PEMECs, so they were ground with grinding papers (SiC grindings paper #250-2400, BUEHLER), then polished using Alumina suspensions with 1 um particle (AS1-32, Mark

V lab) and 0.05μm particle (AS05-32, Mark V lab). The dimensions of printed CGPLA BPs and PLA BPs were 61×61×5.7 mm. The reaction areas for those BPs were 5 cm^2, and the channel land was 10×1×1mm.

The TF-LGDLs used in the research were produced from 50 μm thick Ti film by using wet etching method[47-50]. Before the wet etching process, a photomask was needed. The mask was designed with a CAD/VLSI software (LayoutEditor, layouteditor.net), and developed using Heidelberg DWL 66 laser lithography system on a soda-lime glass. For PR coat process (Figure 20b), a cleaned silicon wafer was coated with the photoresist (MEGAPOSIT™ SPR™ 220, MicroChem), and Ti thin film was bonded onto the photoresist. For the PR coat/pattern process, the adhesion promoter and the second layer of photoresist was applied onto the Ti film. After exposing to UV light through the aforementioned photomask using a Microposit® MF® CD-26 developer (Shipley Company, Marlborough), the photoresist was patterned. The multilayer material was etched in HF to form the desired structure. The last step was removal of photoresist. The TF-LGDLs was 86×86 mm with an etched area at the center. The etched area was 34×34 mm, which has a pore size of 260 μm, a land width of 17.8 μm and a porosity of 87.5%.

Scanning electron microscopy (SEM) images were taken using a field emission SEM JEOL JSM-6320F with an accelerating voltage of 0.5 – 30 kV, a magnification of 250 x~650,000 x and a 5-axis specimen mount. ICR was measured with Wang's method, and a hydraulic press (3912, CARVER INC.) provided a compression pressure of 0.7-2.4 MPa. The resistances were measured by a micro-ohmmeter (6250, AEMC INSTRUMENTS)

Table 4. Configurations of different PEMECs.

Number	Cell name	Cathode BP	Anode BP	Electrons transport path	
				Cathode	Anode
1	C-CGPLA BP	CGPLA	Graphite BP	Through BP	Through BP
2	A/C-PLA BPs	PLA	PLA	Along TF-LGDL	Along TF-LGDL
3	C-PLA BP	PLA	Graphite BP	Along TF-LGDL	Through BP
4	A/C-Graphite BPs	Graphite BP	Graphite BP	Through BP	Through BP

with a resolution of 1μΩ. For all the PEMECs during the *in-situ* experiments, the CCMs (EZ-CCM, FuelCellsEtc) contained a Nafion® 115 membrane with an iridium ruthenium oxide anode CL and a platinum black cathode CL with loading of 3.0 mg/cm^2. The configurations of PEMECs used in this paper are listed in Table 4. For all the PEMECs, the TF-LGDLs with large surroundings were used at both anode and cathode sides. In cell 1, the CGPLA BP and the graphite BPs were incorporated into cathode and anode sides, respectively, and electrons transported through CGPLA. The dimension of graphite BP was 76.31×76.31×12.70 mm, which is to overcome the brittleness of graphite. In cell 2 (Figure 20d), the non-conductive PLA BPs were mounted into both sides, and electrons transported through TF-LGDL laterally from the contact points of LGDL and test station electrodes. In cell 3, non-conductive PLA BP and the graphite BP were incorporated into cathode and anode sides, respectively. Electrons transported through the plane of graphite BP, while transported in the plane of TF-LGDL laterally. The cell 4 had the graphite BPs at both sides, and electrons transported through graphite BPs (Figure 20c). The de-ionized water was supplied by a diagram liquid pump (SIMDOS 10, KNF Neuberger) with a flow rate of 20 ml/min. Electrochemical performances of the PEMECs were conducted by a potentiostat SP-300 chassis with a 5 V/10 A booster from Bio-Logic at 20 °C and atmospheric pressure. The polarization curve results of all plastic PEMECs were gathered from 0 to 10 A with a scan rate of 100 mA/s, and the voltage limit was 4 V. The EIS scans of cell 2-4 were swept from 200 kHz to 30 mHz at 0.2 A/cm^2, while that of cell 1 was swept at 20 mA/cm^2 due to its large total resistance. The high frequency resistance (HFR) results

were recorded at a frequency of 3 kHz. A chronopotentiometry technique was used to investigate the stability of cell 2 at 0.2 A/cm^2 for 100 h at 20 °C.

5.4 Results and discussions

5.4.1 Ex-situ analysis

The images of printed BPs and etched TF-LGDL are presented in Figure 21, the CGPLA is dark (Figure 21a) and solid with no inner structures in the plate (Figure 21d), so as to enhance the electrical conductivity of the BP. There are cracks appeared at the cross-section in CGPLA (Figure 21g, k) which is a result of delamination during printing. But this phenomenon is not found at the surface of the CGPLA BP (Figure 21h, f), so the leakproofness of the CGPLA can be ensured for using as BP. And graphene fibers can be seen at both cross-section and surface, which enhance the electrical conductivity. The PLA is in silver color (Figure 21b). And hollow structures can be found from the cut cross-section image (Figure 21e) as a result of the light infill printing mode, and beams are printed to fill and support the plate. The PLA BP has a smooth surface and demonstrates no delamination (Figure 21i, j, l, m), which will ensure the leakproofness of PEMECs. The etched TF-LGDLs (Figure 21c) have a mass and electron transport section (etched area) at the center, and the outer section (un-etched area) can be used to conduct electron laterally when the electrode of test station is connected with it. Its square pore size at the center is 260 μm, and its land width is 17.8 μm, which lead to a porosity of 87.5% (Figure 21f, n).

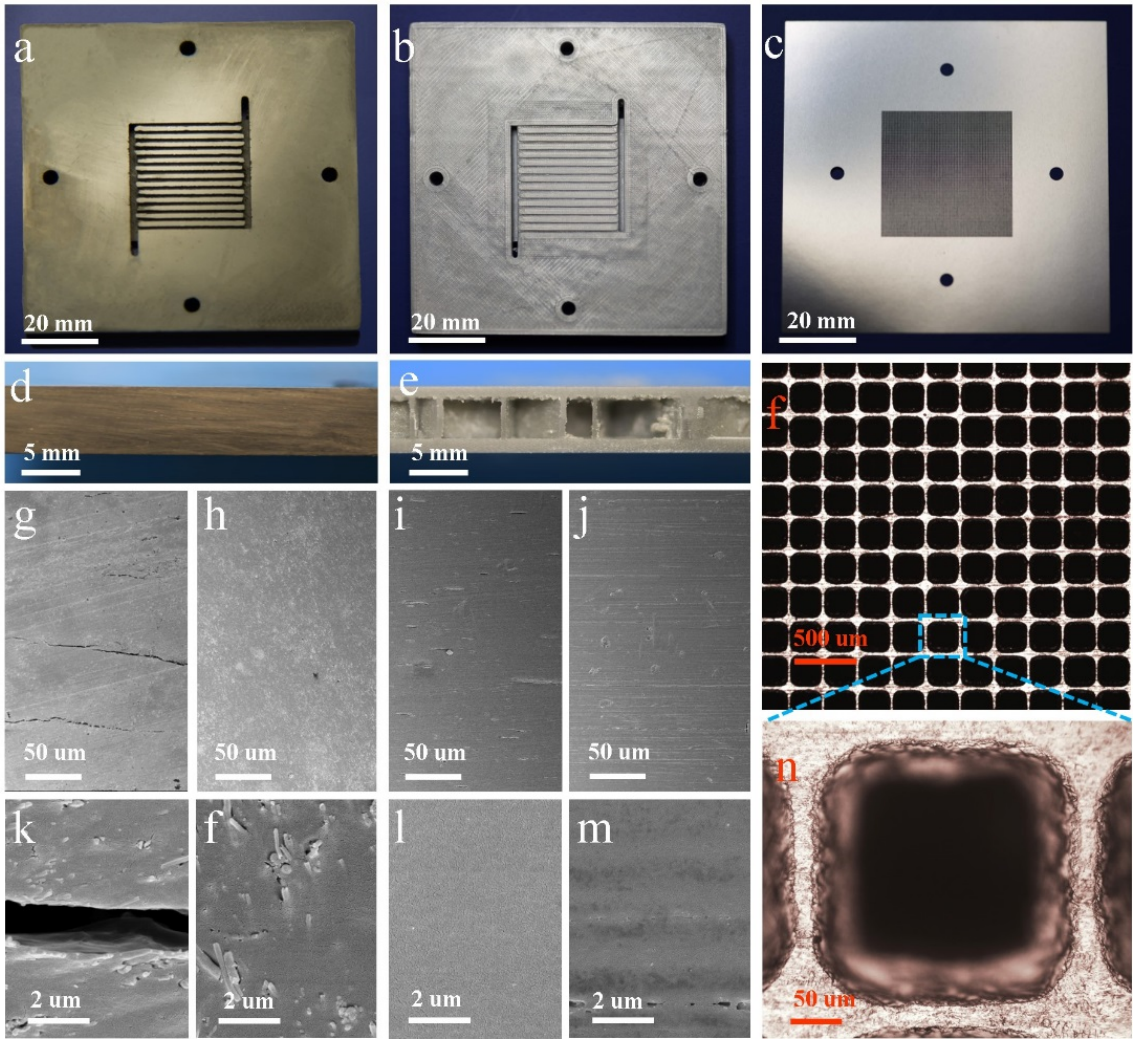

Figure 21. Printed BPs and etched TF-LGDL. Images of surface of (a) CGPLA BP, (b) PLA BP, and (c) TF-LGDL. Images of cross-section of (d) CGPLA BP and (e) PLA BP. (g,k) SEM images of cross-section of CGPLA BP. (h, f) SEM images of surface of CGPLA BP. (i, l) SEM images of cross-section of PLA BP. (j, m) SEM images of surface of PLA BP. (f, n) Microscopy images of TF-LGDL etched area.

For the weight and cost analysis, the volumes and cost of BP with SS and titanium are all based on the dimension of plastic BP used in the experiments, which 61×61×5.7 mm, while the dimension of graphite BP is 76.31×76.31×12.70 mm (in experimental details). The weights of PLA, CGPLA and graphite are measured in the experiments. And the relative data of different materials is shown in Table 5. The table demonstrates the PLA provides the lowest density and volumetric price, but the extremely large electrical resistivity. CGPLA has the moderate electrical resistivity, but its volumetric price is relatively high. The highly electrical-conductive materials (SS, Titanium and graphite) have a much larger density and higher volumetric price.

Table 5. Relative data of different materials for BP manufacturing.

Material	Volumetric pricing (US$·cm^{-3})	Density (g ·cm^{-3})	Electrical resistivity (Ω·cm)
PLA [a]	0.058 [a]	1.147 [d]	∞
CGPLA [b]	0.38 [b]	1.316 [d]	2.11 [d]
SS	0.26 [c]	7.75	6.90×10^{-5}
Titanium	0.32 [c]	4.51	4.2×10^{-5}
Graphite	0.16 [c]	2.26	4.2×10^{-3} [d]

[a]Dynamism. [b]Blackmagic3dMc. [c] From literature[33]. [d]Measured.

The normalized materials cost and weight of bipolar plates with different materials (Figure 22) demonstrate the possibility of lowing the cost of water electrolysis for hydrogen production with PLA materials. Considering that the BP attributes up to 50 % cost and 60% weight of PEMECs [5, 32], the PLA BP would result in a reduction in cost and weight by half for PEMECs if compared with titanium. Since the cost and weight of metal BPs are about 6.76 and 5.36 times larger than those of PLA BPs, respectively. The improvements are even more substantial if compared with graphite. The CGPLA exhibits no advantages than PLA, since its cost is almost the same as titanium, and even higher than SS. Of interest is if the PEMEC with PLA BP can present a good electrochemical performance, the concept of hydrogen production cost will be changed.

5.4.2 Electrochemical full-cell measurements

A series of *in-situ* electrochemical tests were conducted on cells with the aforementioned configurations in Table 4. The polarization curves (Figure 23a) show the PEMEC with CGPLA BP has as progressively increasing voltage, and quickly reaches the voltage limit (4 V) at ~ 200 mA/cm^2. While the PEMECs with A/C – PLA BPs, C-PLA BP, A/C-Graphite BPs require much lower voltages (1.66, 1.63, and 1.61 V, respectively) at 200 mA/cm^2, and the voltages increases slightly with current density. So the PLA BPs can deliver a comparable performance with graphite BPs at 200 mA/cm^2, room temperature and atmospheric pressure. The HFR lines (Figure 23c) are consistent with the polarization curves, and the PEMEC with C-CGPLA BP exhibits an extremely large ohmic resistance (2.0 Ω), but those of other PEMECs are smaller than 0.1 Ω.

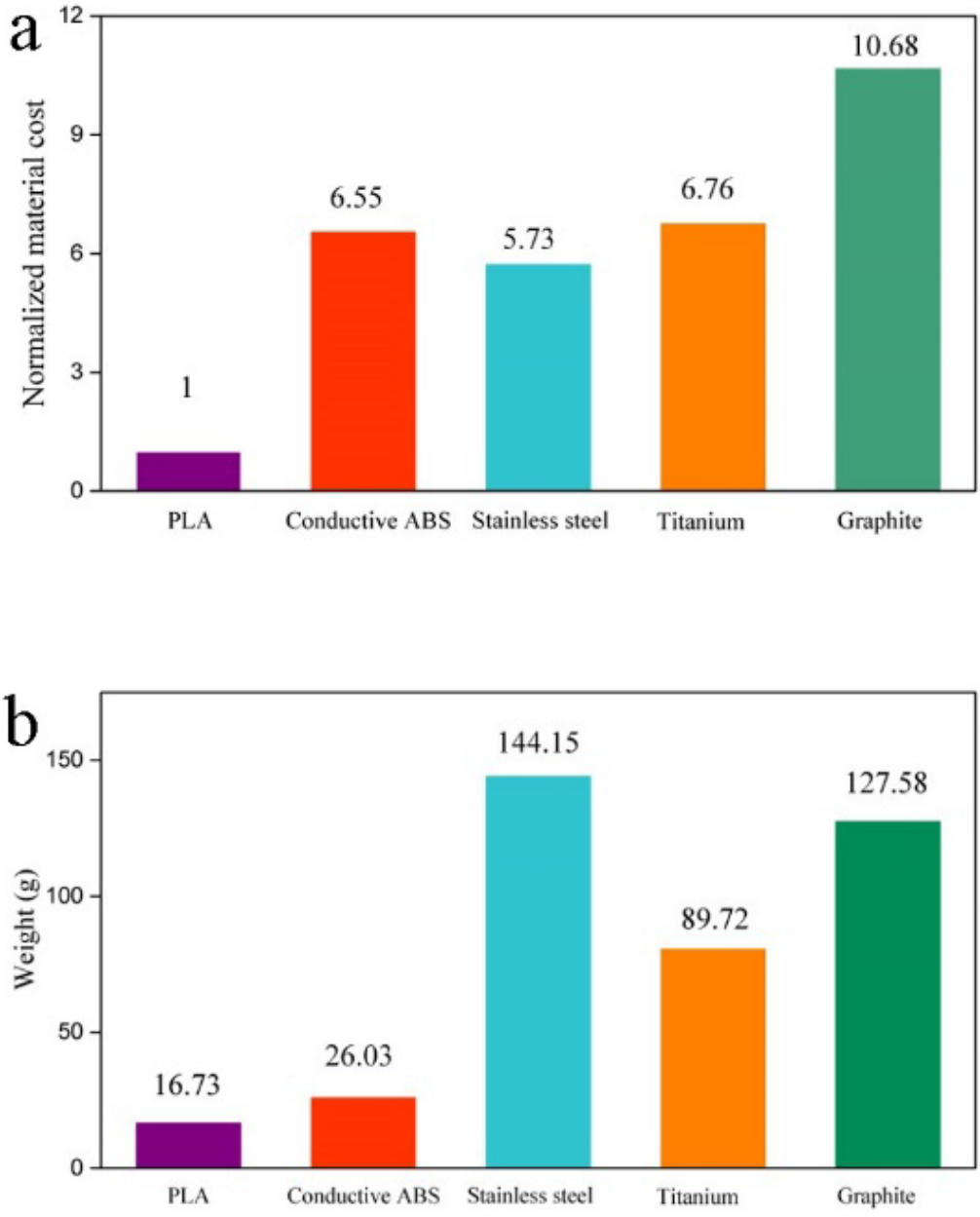

Figure 22. (a) Normalized materials cost, and (b) weight of BPs.

This is due to the high electrical resistance of CGPLA as results of high resistivity of conductive graphene PLA material and the delamination of the printed plate in Figure 23g, k. The delamination retains the electrical conductivity of the 3D printed parts[51]. So the high working voltage of PEMEC with CGPLA BP are mainly caused by its high ohmic overpotential. It can be concluded that even the CGPLA exhibit a smaller electrical resistance than non-conductive PLA, but it is still not comparable to the metallic materials, and not suitable as BP material for electron conducting.

Furthermore, the PEMECs with A/C – PLA BPs provides a low voltage of 2.21 V at 1 A/cm^2, which is much better than that in literatures (>2.40V) [16, 33]. It needs to be mentioned that the PLA BPs used here almost do not require other post-processing, which will decrease the cost and complexity of BP manufacturing, while those in the literatures are coated with Nickle or silver. For the PEMECs with A/C – PLA BPs, C-PLA BP, A/C-Graphite BPs, the graphite BPs deliver a slightly better performance. And the performance differences among PEMECs with A/C – PLA BPs, C-PLA BP, A/C- Graphite BPs can be explained in Figure 23d, their HFRs are 95, 79, 57 mΩ at 2 A/cm^2, respectively. The difference between HFRs of A/C – PLA BPs and C-PLA BP is 22 mΩ, and that between HFRs of C-PLA BP, A/C- Graphite BPs is 16 mΩ. From the *ex-situ* measurements, the contact resistance between LGDL and graphite BP is 4 mΩ, and the in-plane resistance from outer contact point to the center of LGDL is 22 mΩ. Therefore, their difference is 18 mΩ, which is almost consistent with the differences of HFRs (22 and 16 mΩ). And it can

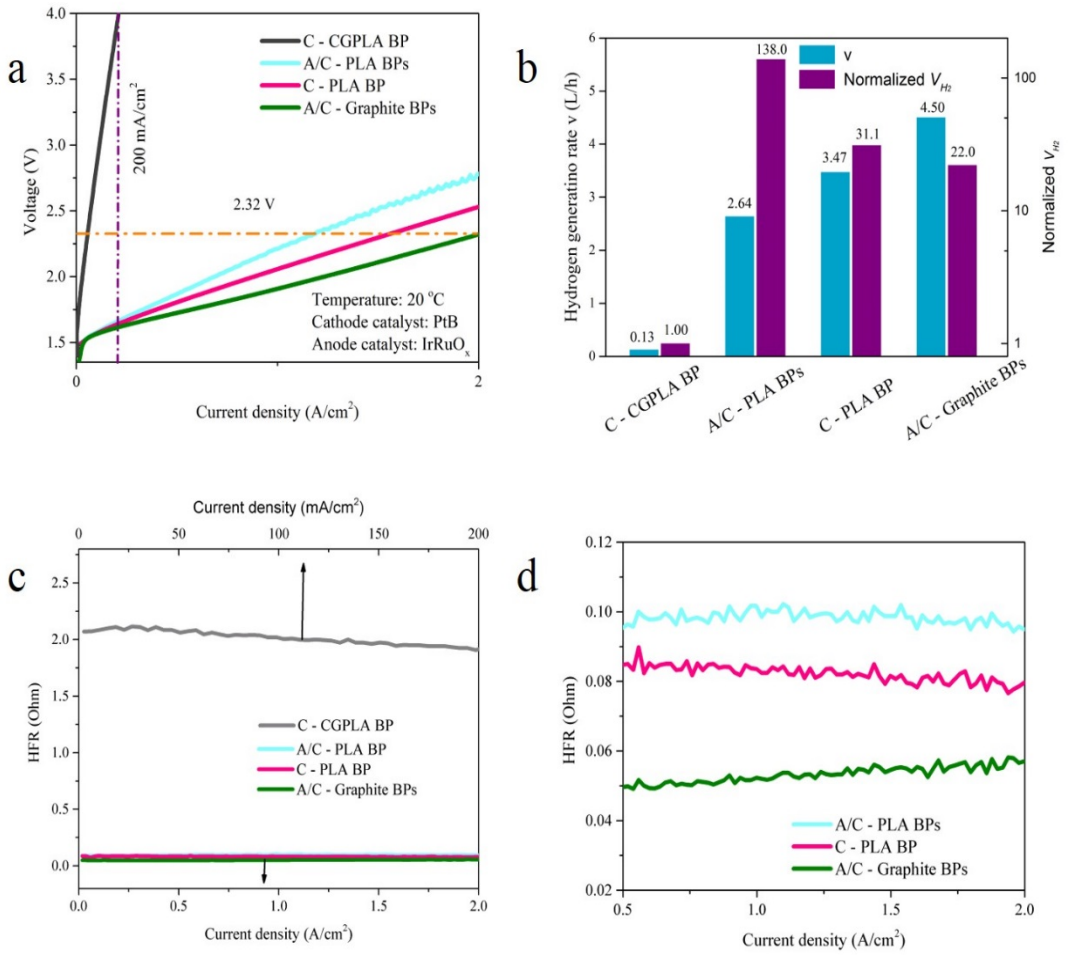

Figure 23. Electrochemical performance of PEMECs with different BPs. (a) Polarization curves recorded on PEMECs with CGPLA BP at cathode (gray), PLA BPs at both sides(cyan), PLA BPs at cathode(red), graphite BPs at both sides(green). (b) Hydrogen generation rate and normalized hydrogen production rates per unite BP cost at 2.32 V. (c) HFRs recorded on PEMECs and (d) the corresponded zoomed-in graph of (c).

be concluded that the in-plane resistance is responsible for the slight voltage increase in PEMECs with PLA BP.

At the constant voltage, the cells have different current density and hydrogen production rate. The hydrogen production rate can be written as[52, 53]:

$$\dot{n}_{H_2} = \frac{i_{cell}A}{nF} \tag{5-1}$$

$$\dot{v}_{H_2} = \dot{n}_{H_2} R_u \frac{T}{P} \tag{5-2}$$

Where $\dot{n}_{H_2}$ is the mole rate of hydrogen production, i_{cell} is the current density of cells, n is the equivalent electrons per mole of production (2 electron eq/mol for H_2), A is the reaction area (5 cm^2), F is charge carried on one equivalent mole (96485 C/eq), $\dot{v}_{H_2}$ is the volume rate of hydrogen generation, R_u is gas constant (8.314 J/mol/K), T is temperature (293.1 K), P is pressure (101 kPa).

The hydrogen production rate per unit BP cost is:

$$\ddot{v}_{H_2} = \frac{\dot{v}_{H_2}}{c_a + c_c} \tag{5-3}$$

where c_a and c_c are the cost of anode BP and cathode BP, respectively.

Then $\ddot{v}_{H_2}$ can be normalized based on the value of PEMEC with C-CGPLA BP:

$$\bar{v}_{H_2} = \frac{\ddot{v}_{H_2}}{\ddot{v}_{H_2}\big|_{C-CGPLA\ BP}} \tag{5-4}$$

where $\ddot{v}_{H_2}\big|_{C-CGPLA\ BP}$ is the hygrogen production rate per unit BP cost of PEMEC with C-CGPLA BP.

The calculated results at 2.32 V are gathered in Figure 23 (purple bar), the $\ddot{v}_{H_2}$ for the cells is 0.13, 2.64, 3.47, and 4.50 L/h, respectively, and the corresponding $\bar{v}_{H_2}$ is 1, 138.0,

31.1, 22.0. The PEMEC with C- CGPLA BP presents both the lowest hydrogen production and hydrogen production rates per unit BP cost. It is shown that the CGPLA BP can not be directly used as BP material without post-processing. The PEMEC with A/C- PLA BP has a medium hydrogen production rate, but the highest hydrogen production rates per unit BP cost, much better than that with A/C-graphite BPs (conventional PEMEC). The PEMEC with graphite BP provide a moderate hydrogen production rates per unit BP cost, but it is still 1/6 of that with PLA BP. Therefore, the PLA BP can significantly increase the hydrogen production rate at a constant capital cost, and also shows its capability of reducing the large-scale hydrogen production cost.

5.4.3 Stability assessment

In order to assess the stability of PLA BP in PEMECs, Chronopotentiometry measurement of PEMEC with A/C- PLA BP is conducted at 200 mA/cm^2 and 20 ^{o}C for 100 h (Figure 24). During the 100 h test, the cell voltage increases from 1.635 V to 1.751V by an average degradation rate of 1.16 mV/h. But the increasing rate varies with time. At the initial 5 h, the cell voltage increases from 1.635 V to 1.650V by an average degradation rate of 3.00 mV/h. Because the PLA BPs are not supposed to transport electron, and there are no electronic resistance and ICR between BP and LGDL. This rapid degrading is seems related to the oxidization and loss of RuO_2 in catalyst layer and degradation of PEM, or the parasitic currents and capacitor discharge originated form the electronics[15, 17]. In the next 10 h, it increases to 1.657 V by an average degradation rate of 1.40 mV/h, which is comparatively stable. In the last 90 h, the cell enter a stable condition with a degrading

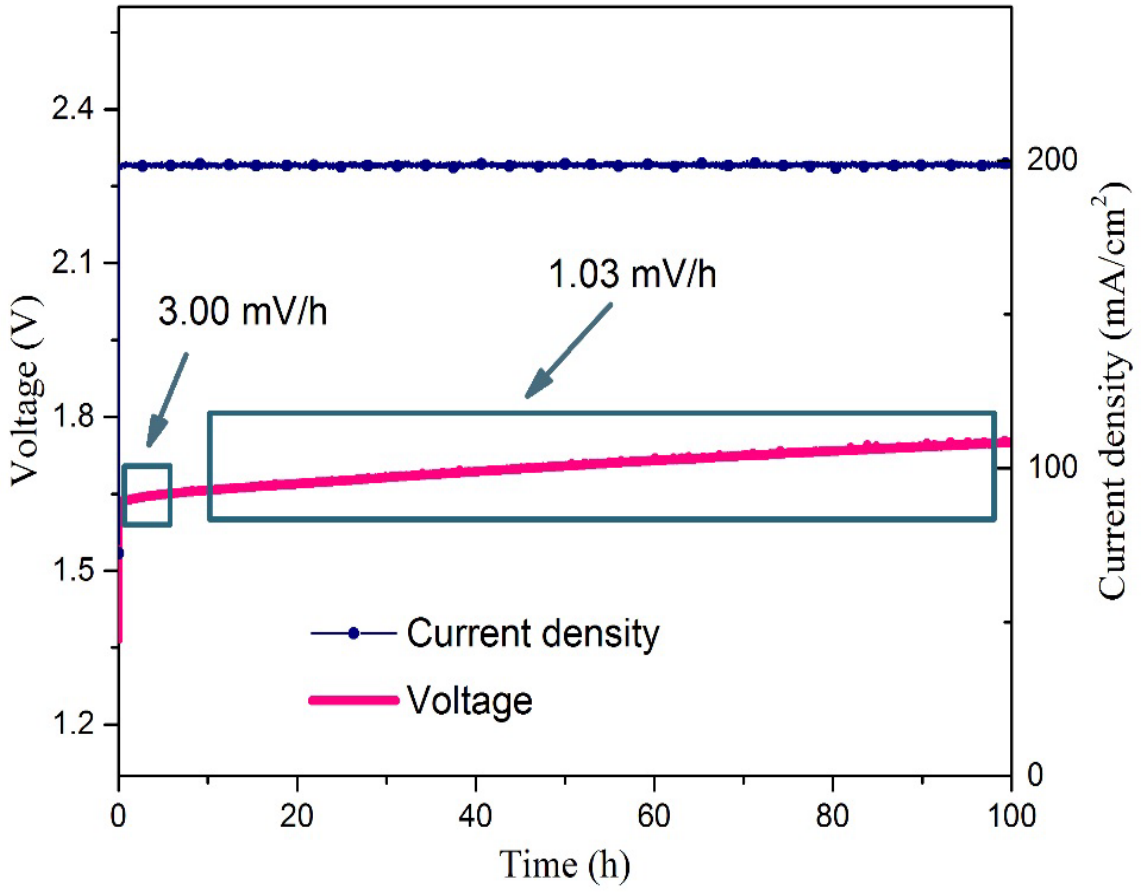

Figure 24. Chronopotentiometry measurements of PEMEC with A/C- PLA BP at 200 mA/cm^2 and 20 ^{o}C for 100 h.

of only 1.03 mV/h. If the degradation of PEM and loss and oxidization of catalyst are excluded from the Chronopotentiometry results, the degradation of PLA BPs will have limited influence on the stability of PEMEC.

5.4.4 Simulation analysis for BPs with different resistivity

In order to further investigate the electrochemical performance of the PEMECs with different BPs, and to study the influence of BP resistivity on the cell, situational computations will be conducted. A simulation model is developed with MATLAB/Simulink platform (Figure 25a), which consists of variable modules, including operation conditions module, ohmic resistance module, and overpotential calculation module[54, 55]. The current density is considered as variable during the polarization curve modeling (Figure 25b), and BP resistivity is variable during the evaluation of impact of BP resistivity on the performance of PEMECs (Figure 25c, d). Operation conditions, include reaction area (5 cm^2), pressure (1 atm), temperature (293.1 K), are kept constantly. Other parameters (Table 6) used in the simulation are based on the dimensions and factors of components in the experiments. Then the anode and cathode exchange current densities are varied to tune the mode, so that the simulation will fit the experimental data. The polarization curves of PEMEC with A/C-Graphite BPs are chose to validated the model and compared with the simulation results, and the resistivity of the BP is came from that of graphite, which is 1.5×10^{-3} Ω·cm[54]. The green line and pink dots (Figure 25b) shows they have a good agreement. When simulating the polarization curves of PEMECs with A/C-PLA BPs and C- CGPLA BP, only the resistivity

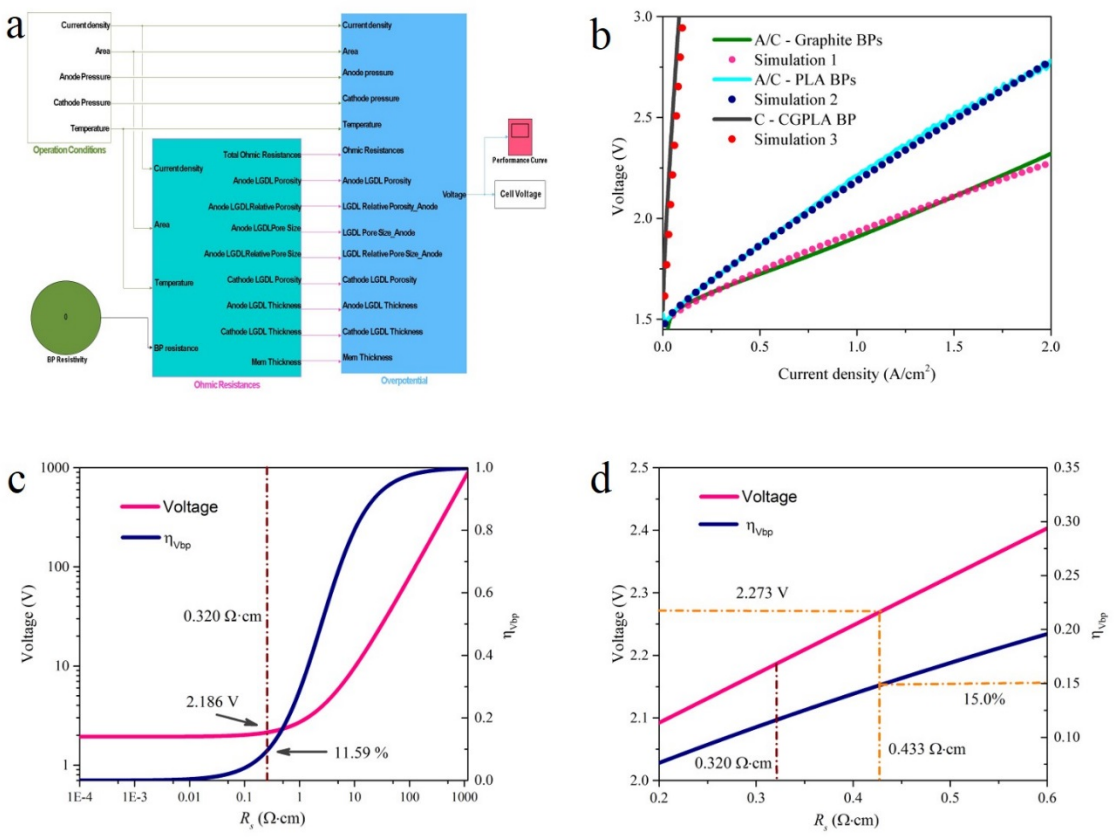

Figure 25. (a) MATLAB/Simulink model schematic of PEMECs with different BPs. (b) Simulated polarization curves. (c) Simulated cell voltage (red line), and percentage of voltage for BP resistance in total voltage (dark blue line) vary with BP resistivity, and (d) corresponded zoomed-in graph of c.

of BP was adjust to fit the experimental data. The adjusted equivalent resistivity of BPs with A/C-PLA BPs, and C- CGPLA BP in the cells in Figure 25b are 0.32 and 18 Ω·cm, respectively. Those simulated resistivity is agree with those from HFR data, and also demonstrate this model can be used to investigate the influence of resistivity on cell voltage.

The current density used during simulation for different resistivity is 1 A/cm^2. From Figure 25c, both simulated cell voltage and percentage of voltage for BP resistance in total voltage increase with resistivity of BP. At the resistivity range of 0 - 0.1 Ω·cm, the cell voltage and percentage increase slightly (1.933- 2.013 V, and 0 – 4.02 %, respectively), and the BP resistance has limited impact on the performance. The resistivity of metallic materials and graphite is in this range, which means the resistance of metal and graphite BP in the PEMECs are neglectable [28, 32, 56]. At the range of 0.1-1 Ω·cm, they have a moderate increase (2.013 - 2.713 V, 4.02 - 28.76 %), as a result of incremental proportion of BP resistance in total resistance. The equivalent resistivity of PEMEC with PLA BP is in this range. At the range of 1 - 1000 Ω·cm, they have a rapid increase (> 2.713 V, > 28.76 %), and the performance is not acceptable for hydrogen production.

In order to evaluate the material suitability for BPs, the threshold value of percentage of voltage for BP resistance is set as 15%, which results in a resistivity of 0.433 Ω·cm and a voltage of 2.27 V at 1 A/cm^2 (Figure 25). It means that a material can be used for BP manufacturing, only if its electrical resistivity is lower than 0.433 Ω·cm, and it will contribute no more than 15% of cell voltage. So far, the commonly used materials for BP

Table 6. Parameters for the simulation of PEMECs with BPs with different resistivity.

Parameters for simulation analysis	Value
PEMEC active area	5.0 cm^2
PEM	Nafion 115 with 125 μm thickness
Pressure	101 kPa for both sides
Temperature	293.1 K
LGDL thickness	50μm
LGDL pore size	260 μm
LGDL porosity	87.5%
LGDL electrical resistivity	5.4×10^{-5} Ω·cm
CL thickness	15 μm
CL electrical resistivity	Anode: 5.0×10^{-2} Ω·cm
	Cathode: 1.4×10^{-3} Ω·cm [54]
DI water density	1g/cm^3
DI water dynamic viscosity	3.55×10^{-3} N·s/m^2
Exchange current density	Anode: 2×10^{-12} A/cm^2
	Cathode: 2.5×10^{-1} A/cm^2
ICR between LGDL and BP(fitted)	22.2 mΩ
Resistivity of BP	Varied from 0 to 1000 Ω·cm
Faraday constant	96487.0 C/mol

Table 6 Continued

Parameters for simulation analysis	Value
PEM humidification degree	24 [55]
Charge transfer coefficient	Anode:2
	Cathode:0.5 [54]
Current density	Varied from 0 to 2 A/cm^2

can reach such a low resistivity, which include iron alloys (< 2× 10^{-7} Ω·cm), titanium (<5× 10^{-7} Ω·cm), graphite (~10^{-3} Ω·cm) and several kinds of composites (3× 10^{-3} -1 Ω·cm) [5, 15, 57, 58]. But the conductive plastic materials, even with coating layers, can not reach such threshold[33]. It is obviously if the PEMEC with A/C-PLA BPs can equipped with the LGDL with large surrounding, the electron will transport in the plane of LGDL laterally. Consequently, the PEMEC with A/C-PLA BPs can provide a low BP equivalent resistivity of 0.320 Ω·cm, a voltage of 2.186 V, and a percentage of 11.59 %.Those values are under the threshold for BP materials, and indicate the suitability of PLA BPs and TF-LGDLs for low-cost and high-efficiency water electrolysis.

5.5 Conclusion

In summary, a novel PEMEC with non-conductive BPs and TF-LGDLs is developed to reduce the cost and improve the performance of overall water splitting. The rapidly printed non-conductive PLA BPs without post-processing (coating, plating, etc.) enable the mass distribution, and provide mechanical support for the cell. A TF-LGDL with surroundings

wet-etched with Ti film offers a new electron conduction path, which directly transports electron into or out of PEMECs laterally. In PEMECs, PLA BPs exhibit an extremely low cost (1/10 of the graphite BP), and their hydrogen production rate per unit BP cost is almost 6 times higher than that of conventional cell. Furthermore, a relatively low voltage of 2.21 V at 1 A/cm^2 under room temperature, and a good stability with an average degradation rate of 1.03 mV/h are achieved in the PEMEC with PLA BPs. The numerical simulation helps to connect the resistivity of BPs and the cell performance, then a threshold value of 0.433 Ω·cm is derived for guiding the selection of BPs material. The accessible and extremely low-cost BP as well as the good electrochemical performance will open a road for developing plastic materials for low cost water splitting or energy conversion devices, such as batteries, solar cells, and fuel cells.

References

[1] J. A. Turner, "Sustainable hydrogen production," *Science,* vol. 305, pp. 972-974, 2004.

[2] B. Pivovar, N. Rustagi, and S. Satyapal, "Hydrogen at Scale (H2@ Scale): Key to a Clean, Economic, and Sustainable Energy System," *The Electrochemical Society Interface,* vol. 27, pp. 47-52, 2018.

[3] K. E. Ayers, C. Capuano, and E. B. Anderson, "Recent advances in cell cost and efficiency for PEM-based water electrolysis," *ECS Transactions,* vol. 41, pp. 15-22, 2012.

[4] V. R. Stamenkovic, D. Strmcnik, P. P. Lopes, and N. M. Markovic, "Energy and fuels from electrochemical interfaces," *Nature Materials,* vol. 16, pp. 57-69, 2017.

[5] M. Carmo, D. L. Fritz, J. Mergel, and D. Stolten, "A comprehensive review on PEM water electrolysis," *International Journal of Hydrogen Energy,* vol. 38, pp. 4901-4934, 2013.

[6] B. Lee, J. Heo, S. Kim, C. Sung, C. Moon, S. Moon*, et al.*, "Economic feasibility studies of high pressure PEM water electrolysis for distributed H 2 refueling stations," *Energy Conversion and Management,* vol. 162, pp. 139-144, 2018.

[7] U. Babic, M. Suermann, F. N. Büchi, L. Gubler, and T. J. Schmidt, "Critical Review—Identifying Critical Gaps for Polymer Electrolyte Water Electrolysis Development," *Journal of The Electrochemical Society,* vol. 164, pp. F387-F399, 2017.

[8] S. Y. Tee, K. Y. Win, W. S. Teo, L. D. Koh, S. Liu, C. P. Teng, *et al.*, "Recent Progress in Energy-Driven Water Splitting," *Advanced Science,* 2017.

[9] M. Al-Zareer, I. Dincer, and M. A. Rosen, "Analysis and assessment of a hydrogen production plant consisting of coal gasification, thermochemical water decomposition and hydrogen compression systems," *Energy Conversion and Management,* vol. 157, pp. 600-618, 2018.

[10] R. Bhattacharyya, A. Misra, and K. Sandeep, "Photovoltaic solar energy conversion for hydrogen production by alkaline water electrolysis: conceptual design and analysis," *Energy conversion and management,* vol. 133, pp. 1-13, 2017.

[11] M. A. Pellow, C. J. Emmott, C. J. Barnhart, and S. M. Benson, "Hydrogen or batteries for grid storage? A net energy analysis," *Energy & Environmental Science,* vol. 8, pp. 1938-1952, 2015.

[12] G. Nong, Y. Chen, M. Li, and Z. Zhou, "Generation of hydrogen free radicals from water for fuels by electric field induction," *Energy Conversion and Management,* vol. 105, pp. 545-551, 2015.

[13] A. Sternberg and A. Bardow, "Power-to-What?–Environmental assessment of energy storage systems," *Energy & Environmental Science,* vol. 8, pp. 389-400, 2015.

[14] D. Ferrero and M. Santarelli, "Investigation of a novel concept for hydrogen production by PEM water electrolysis integrated with multi-junction solar cells," *Energy Conversion and Management,* vol. 148, pp. 16-29, 2017.

[15] G. Yang, J. Mo, Z. Kang, Y. Dohrmann, F. A. List, J. B. Green*, et al.*, "Fully printed and integrated electrolyzer cells with additive manufacturing for high-efficiency water splitting," *Applied Energy,* vol. 215, pp. 202-210, 2018.

[16] G. Chisholm, P. J. Kitson, N. D. Kirkaldy, L. G. Bloor, and L. Cronin, "3D printed flow plates for the electrolysis of water: an economic and adaptable approach to device manufacture," *Energy & Environmental Science,* vol. 7, pp. 3026-3032, 2014.

[17] P. Lettenmeier, R. Wang, R. Abouatallah, B. Saruhan, O. Freitag, P. Gazdzicki*, et al.*, "Low-Cost and Durable Bipolar Plates for Proton Exchange Membrane Electrolyzers," *Scientific Reports,* vol. 7, p. srep44035, 2017.

[18] J. Mo, Z. Kang, G. Yang, S. T. Retterer, D. A. Cullen, T. J. Toops*, et al.*, "Thin liquid/gas diffusion layers for high-efficiency hydrogen production from water splitting," *Applied Energy,* vol. 177, pp. 817-822, 2016.

[19] Z. Kang, J. Mo, G. Yang, S. T. Retterer, D. A. Cullen, T. J. Toops*, et al.*, "Investigation of thin/well-tunable liquid/gas diffusion layers exhibiting superior multifunctional performance in low-temperature electrolytic water splitting," *Energy & Environmental Science,* 2017.

[20] B. Han, J. Mo, Z. Kang, G. Yang, W. Barnhill, and F.-Y. Zhang, "Modeling of two-phase transport in proton exchange membrane electrolyzer cells for hydrogen energy," *International Journal of Hydrogen Energy,* vol. 42, pp. 4478-4489, 2017.

[21] Z. Kang, J. Mo, G. Yang, Y. Li, D. A. Talley, S. T. Retterer*, et al.*, "Thin film surface modifications of thin/tunable liquid/gas diffusion layers for high-efficiency proton exchange membrane electrolyzer cells," *Applied Energy,* vol. 206, pp. 983-990, 2017.

[22] Z. Kang, G. Yang, J. Mo, Y. Li, S. Yu, D. A. Cullen*, et al.*, "Novel Thin/Tunable Gas Diffusion Electrodes with Ultra-Low Catalyst Loading for Hydrogen Evolution Reactions in Proton Exchange Membrane Electrolyzer Cells," *Nano Energy,* 2018.

[23] P. Liang, D. Qiu, L. Peng, P. Yi, X. Lai, and J. Ni, "Structure failure of the sealing in the assembly process for proton exchange membrane fuel cells," *International Journal of Hydrogen Energy,* vol. 42, pp. 10217-10227, 2017.

[24] S. S. Alrwashdeh, I. Manke, H. Markötter, J. Haußmann, N. Kardjilov, A. Hilger*, et al.*, "Neutron radiographic in operando investigation of water transport in polymer electrolyte membrane fuel cells with channel barriers," *Energy conversion and management,* vol. 148, pp. 604-610, 2017.

[25] G. Yang, S. Yu, J. Mo, Z. Kang, Y. Dohrmann, F. A. List*, et al.*, "Bipolar plate development with additive manufacturing and protective coating for durable and high-efficiency hydrogen production," *Journal of Power Sources,* vol. 396, pp. 590-598, 2018.

[26] A. Ghanbarian, M. Kermani, J. Scholta, and M. Abdollahzadeh, "Polymer electrolyte membrane fuel cell flow field design criteria–Application to parallel

serpentine flow patterns," *Energy Conversion and Management,* vol. 166, pp. 281-296, 2018.

[27] G. Yang, J. Mo, Z. Kang, F. A. List, J. B. Green, S. S. Babu*, et al.*, "Additive manufactured bipolar plate for high-efficiency hydrogen production in proton exchange membrane electrolyzer cells," *International Journal of Hydrogen Energy,* vol. 42, pp. 14734-14740, 2017.

[28] S. Karimi, N. Fraser, B. Roberts, and F. R. Foulkes, "A review of metallic bipolar plates for proton exchange membrane fuel cells: materials and fabrication methods," *Advances in Materials Science and Engineering,* vol. 2012, 2012.

[29] X. Li and I. Sabir, "Review of bipolar plates in PEM fuel cells: Flow-field designs," *International Journal of Hydrogen Energy,* vol. 30, pp. 359-371, 2005.

[30] N. Zehtabiyan-Rezaie, A. Arefian, M. J. Kermani, A. K. Noughabi, and M. Abdollahzadeh, "Effect of flow field with converging and diverging channels on proton exchange membrane fuel cell performance," *Energy Conversion and Management,* vol. 152, pp. 31-44, 2017.

[31] K. E. Ayers, E. B. Anderson, C. Capuano, B. Carter, L. Dalton, G. Hanlon*, et al.*, "Research advances towards low cost, high efficiency PEM electrolysis," *ECS Transactions,* vol. 33, pp. 3-15, 2010.

[32] H. Tawfik, Y. Hung, and D. Mahajan, "Metal bipolar plates for PEM fuel cell—a review," *Journal of Power Sources,* vol. 163, pp. 755-767, 2007.

[33] J. R. Hudkins, D. G. Wheeler, B. Peña, and C. P. Berlinguette, "Rapid prototyping of electrolyzer flow field plates," *Energy & Environmental Science,* 2016.

[34] K. Alayavalli and D. L. Bourell, "Fabrication of modified graphite bipolar plates by indirect selective laser sintering (SLS) for direct methanol fuel cells," *Rapid prototyping journal,* vol. 16, pp. 268-274, 2010.

[35] S. Chen, D. L. Bourell, and K. L. Wood, "Fabrication of PEM fuel cell bipolar plates by indirect SLS," in *International SFF Symposium, Austin, TX, August*, 2004, pp. 2-4.

[36] D. Bourell, M.-C. Leu, K. Chakravarthy, N. Guo, and K. Alayavalli, "Graphite-based indirect laser sintered fuel cell bipolar plates containing carbon fiber additions," *CIRP Annals-Manufacturing Technology,* vol. 60, pp. 275-278, 2011.

[37] R. García-Valverde, N. Espinosa, and A. Urbina, "Simple PEM water electrolyser model and experimental validation," *international journal of hydrogen energy,* vol. 37, pp. 1927-1938, 2012.

[38] P. Millet, D. Dragoe, S. Grigoriev, V. Fateev, and C. Etievant, "GenHyPEM: a research program on PEM water electrolysis supported by the European Commission," *International Journal of Hydrogen Energy,* vol. 34, pp. 4974-4982, 2009.

[39] P. Liang, D. Qiu, L. Peng, P. Yi, X. Lai, and J. Ni, "Contact resistance prediction of proton exchange membrane fuel cell considering fabrication characteristics of

metallic bipolar plates," *Energy Conversion and Management,* vol. 169, pp. 334-344, 2018.

[40] G. Yang, J. Mo, Z. Kang, Y. Dohrmann, F. A. List, J. B. Green*, et al.*, "3D Printed Bipolar Plate for Water Electrolysis," in *Meeting Abstracts*, 2017, pp. 1517-1517.

[41] A. Gago, S. Ansar, B. Saruhan, U. Schulz, P. Lettenmeier, N. Cañas*, et al.*, "Protective coatings on stainless steel bipolar plates for proton exchange membrane (PEM) electrolysers," *Journal of Power Sources,* vol. 307, pp. 815-825, 2016.

[42] D. Prasai, J. C. Tuberquia, R. R. Harl, G. K. Jennings, and K. I. Bolotin, "Graphene: corrosion-inhibiting coating," *ACS nano,* vol. 6, pp. 1102-1108, 2012.

[43] S. Park, Y. Shao, J. Liu, and Y. Wang, "Oxygen electrocatalysts for water electrolyzers and reversible fuel cells: status and perspective," *Energy & Environmental Science,* vol. 5, pp. 9331-9344, 2012.

[44] T. Reier, H. N. Nong, D. Teschner, R. Schlögl, and P. Strasser, "Electrocatalytic Oxygen Evolution Reaction in Acidic Environments–Reaction Mechanisms and Catalysts," *Advanced Energy Materials,* 2016.

[45] Y. Yan, B. Y. Xia, B. Zhao, and X. Wang, "A review on noble-metal-free bifunctional heterogeneous catalysts for overall electrochemical water splitting," *Journal of Materials Chemistry A,* vol. 4, pp. 17587-17603, 2016.

[46] P. Lettenmeier, J. Majchel, L. Wang, V. Saveleva, S. Zafeiratos, E. Savinova*, et al.*, "Highly active nano-sized iridium catalysts: synthesis and operando

spectroscopy in a proton exchange membrane electrolyzer," *Chemical science,* vol. 9, pp. 3570-3579, 2018.

[47] F.-Y. Zhang, A. K. Prasad, and S. G. Advani, "Investigation of a copper etching technique to fabricate metallic gas diffusion media," *Journal of Micromechanics and Microengineering,* vol. 16, p. N23, 2006.

[48] F.-Y. Zhang, S. G. Advani, and A. K. Prasad, "Performance of a metallic gas diffusion layer for PEM fuel cells," *Journal of Power Sources,* vol. 176, pp. 293-298, 2008.

[49] Z. Kang, G. Yang, J. Mo, S. Yu, D. A. Cullen, S. T. Retterer*, et al.*, "Developing titanium micro/nano porous layers on planar thin/tunable LGDLs for high-efficiency hydrogen production," *International Journal of Hydrogen Energy,* 2018.

[50] J. Mo, S. M. Steen, S. Retterer, D. A. Cullen, A. Terekhov, and F.-Y. Zhang, "Mask-Patterned Wet Etching of Thin Titanium Liquid/Gas Diffusion Layers for a PEMEC," *ECS Transactions,* vol. 66, pp. 3-10, 2015.

[51] V. Sanchez-Romaguera, M.-B. Madec, and S. G. Yeates, "Inkjet printing of 3D metal–insulator–metal crossovers," *Reactive and Functional Polymers,* vol. 68, pp. 1052-1058, 2008.

[52] M. M. Mench, *Fuel cell engines*: John Wiley & Sons, 2008.

[53] M. Shen, N. Bennett, Y. Ding, and K. Scott, "A concise model for evaluating water electrolysis," *international journal of hydrogen energy,* vol. 36, pp. 14335-14341, 2011.

[54] B. Han, J. Mo, Z. Kang, and F.-Y. Zhang, "Effects of membrane electrode assembly properties on two-phase transport and performance in proton exchange membrane electrolyzer cells," *Electrochimica Acta,* vol. 188, pp. 317-326, 2016.

[55] Z. Kang, J. Mo, G. Yang, Y. Li, D. A. Talley, B. Han*, et al.*, "Performance Modeling and Current Mapping of Proton Exchange Membrane Electrolyzer Cells with Novel Thin/Tunable Liquid/Gas Diffusion Layers," *Electrochimica Acta,* vol. 255, pp. 405-416, 2017.

[56] H. Wang, M. P. Brady, G. Teeter, and J. Turner, "Thermally nitrided stainless steels for polymer electrolyte membrane fuel cell bipolar plates: Part 1: Model Ni–50Cr and austenitic 349™ alloys," *Journal of Power Sources,* vol. 138, pp. 86-93, 2004.

[57] N. De las Heras, E. Roberts, R. Langton, and D. Hodgson, "A review of metal separator plate materials suitable for automotive PEM fuel cells," *Energy & Environmental Science,* vol. 2, pp. 206-214, 2009.

[58] I. Bar-On, R. Kirchain, and R. Roth, "Technical cost analysis for PEM fuel cells," *Journal of Power Sources,* vol. 109, pp. 71-75, 2002.

CHAPTER VI

ADDITIVE MANUFACTURED MICRO-SENSOR FROM SILVER NANOPARTICLES FOR MEASURING SHEAR STRESS AND PRESSURE

A version of this chapter was originally published by Gaoqiang Yang:

Yang, Gaoqiang, Jingke Mo, Zhenye Kang, Yeshi Dohrmann, Feng-Yuan Zhang, Shahnavaz Eilbeigi, Farnaz Farahanipad, and Haiying Huang. "Additive manufactured micro-sensor from silver nanoparticles for measuring shear stress and pressure." In *Nano/Micro Engineered and Molecular Systems (NEMS), 2017 IEEE 12th International Conference on*, pp. 164-168. IEEE, 2017.

I am fully responsible for the work submitted in these publications.

6.1 Abstract

Additive manufacturing is considered as a revolution in manufacturing. One of this type of manufacturing, three-dimensional (3D) inkjet printing is capable of quickly printing conductive tracks on flexible materials, and have attracted considerable attentions in recent years. To take advantage of this technology, flexible micro-sensors for measuring shear stress and pressure are fabricated from silver nanoparticles with digital models by 3D inkjet printing rapidly. The influence of printing layers and sintering temperature on the chemical and physical properties of micro-sensors are investigated. Surface morphology and electrical resistivity are also examined ex-situ. Test results show the thickness and electrical resistivity of AM micro-sensors deceased significantly as the increase of sintering temperature, which achieve 1.41 μm and 7.64×10^{-8} Ω·m at the sintering temperature of 250 °C, respectively. Furthermore, in-situ experiments are also carried out to investigate the performance of AM micro-sensors for measuring shear stress and pressure. The novel AM

micro-sensors provide a new route to the economic and rapid development of shear stress and pressure sensing.

6.2 Background

Pressure and shear stress are the components of mechanical stress applied on a planar surface, but most studies have been focused on pressure sensing. Recently, our group has developed shear and pressure sensors based on microstrip patch antenna technology [1, 2]. These sensors were fabricated from conventional printed circuit boards using the lithography and chemical etching process, which is time-consuming and inflexible [2-5]. In recent years, 3D inkjet printing, a drop-on-demand (DOD) process, can provide a facile and low-cost way to produce micro-sensors rapidly. Successful fabrication of those micro-sensors will accelerate the studies on mechanical stress sensing, which requires small-batch production of electronics with frequent design changes [6-10]. Due to the high conductivity and thermal stability, gold and silver nanoparticles. suspensions were widely used in the research of conductive inks[11-13]. Silver nanoparticles with a diameter below 50 nm have a significantly lower sintering temperature, typically 160-300°C, compared with the melting temperature of the bulk material, 963°C [11, 14-16]. Thus, Silver nanoparticles are suitable to form the micro-sensors on Kapton substrates. Herein, we employed 3D inkjet printing to fabricate flexible micro-sensors for measuring shear stress and pressure from silver nanoparticles. The parameters for printing and sintering are discussed, and the radiation characteristics of the antenna sensors are validated.

6.3 Current results

An electrically conductive nano-silver ink (Metalon® JS-A102, Novacentrix) is used in this study, it is characterized as having 40 wt% Ag, viscosity of 8-12 cP, surface tension 25-30 dyne/cm, average particle size of 40-60 nm at 25°C. Polyimide films (Kapton® HN, DuPont) with thickness of 25 μm are chosen as substrate and preheated to 60 °C before printing. The printing processes were conducted by a Dimatix materials printer (DMP-2831, Fujifilm), as shown in Figure 26. The printer had a 16-nazzle print head, and a 1 pl disposable piezo ‘‘ink jet” cartridge was utilized. The patterns of micro-sensors were

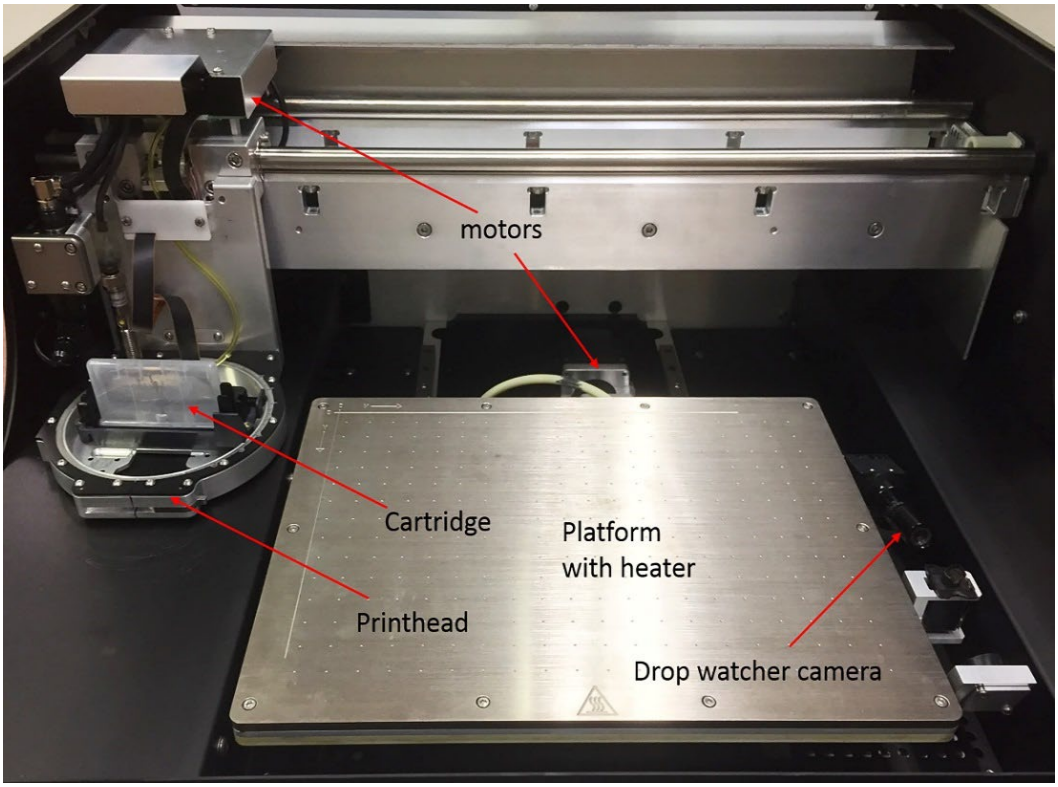

Figure 26. Photo of 3D ink jet printer.

designed by AutoCAD 2016 software. Drop Watcher camera system allowed to monitor the droplets from the print head, as shown in Figure 27. the black line shows the movement of the droplet. Before printing, the temperature of the vacuum platform was adjusted up to 60 °C, which would accelerate the evaporation of solvent, and the head angle of print head was set to 2.3° for dropping space of 10 μm.

Micro-sensors were printed with different layers, and dried at 60 °C for 30 minutes in the printer. The sensors were then sintered at 100 °C, 150 °C, 200 °C and 250 °C, and compared with un-sintered one, respectively. Figure 28(a) shows the bright AM micro-sensors with silver films, and Figure 28(b) shows the flexibility of the sensors which can broaden its usage in different conditions.

Figure 27. Drop watcher view of droplet.

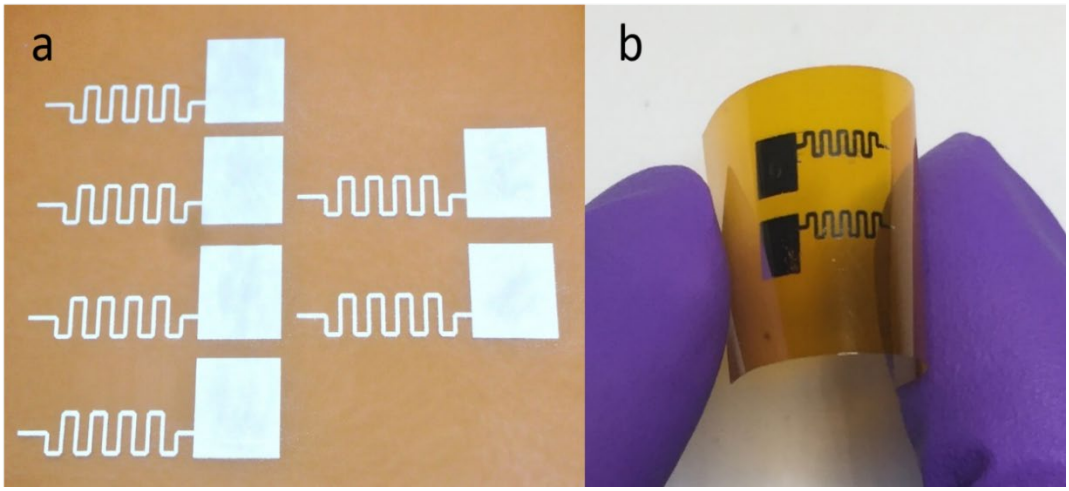

Figure 28. Flexible micro-sensor.

The Scanning electron microscopy (SEM) images of those sensors in Figure 29 show the morphology and element distributions of the silver film before and after sintering at 200 °C, the silver nanoparticles in Figure 29a have a clear edge before sintering, but Figure 29b indicates the particles were sintered together and the sphere edge disappeared. Prior to EDS analysis, the un-sintered sensors were coated with Au to increase its electrical conductivity. In Figure 29c, EDS analysis of the silver film shown only Ag and slight Cl left before sintering, and Figure 29d indicates the elements almost remained the same before and after sintering. The surface profile image of the antenna after sintering at 200 °C were also provided in Figure 30, and the image shows the even and smooth suface of the antenna. The electrical resistivity and thickness of the micro-sensors with one layer were measured using micro-Ohmmeter (6250, AEMC) and microscopy (SM2-U, Olympus), and the results were shown in Figure 31. Test results show the thickness and

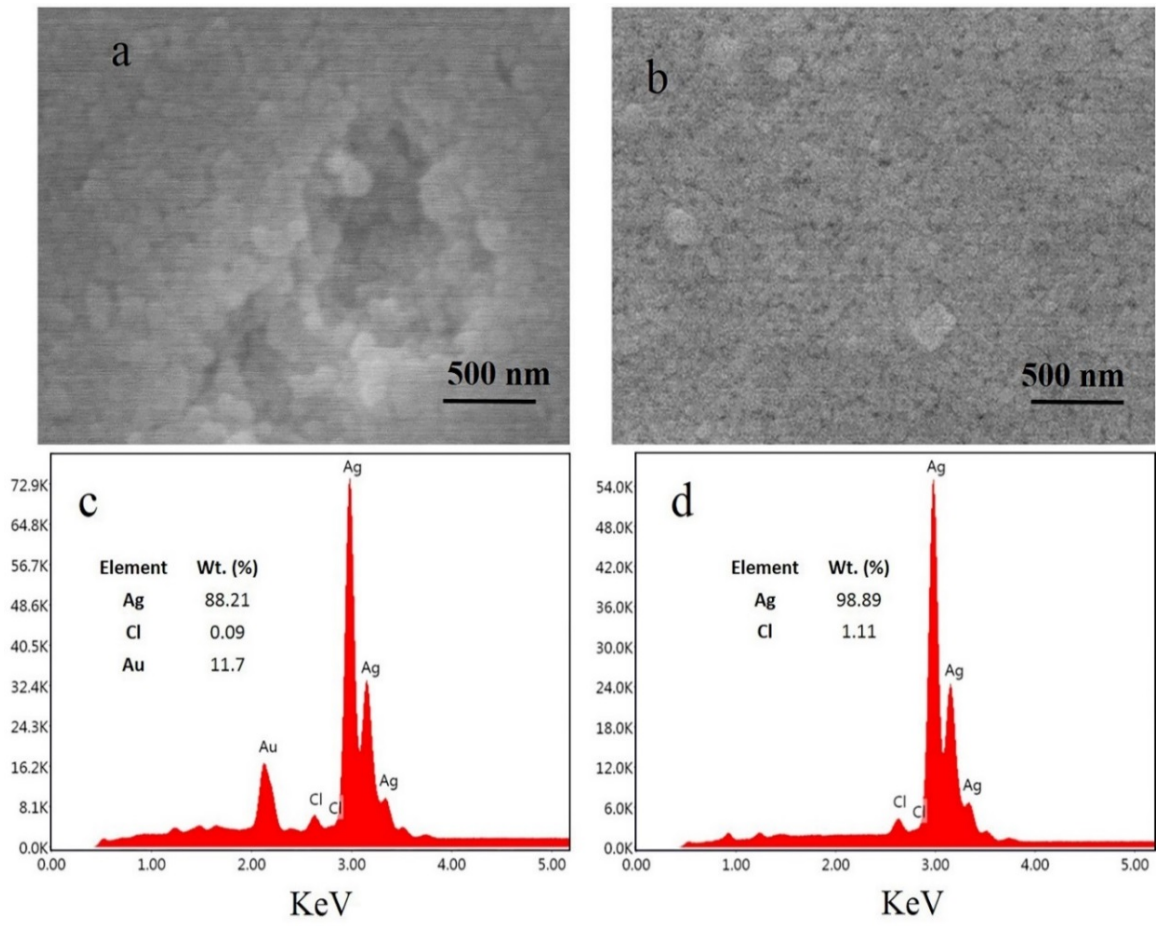

Figure 29. SEM and EDS images of the silver films. (a) SEM image of the silver films before sintering at 200 °C. (b) SEM image of the silver films after sintering at 200 °C. (c) EDS analysis of the silver films before sintering at 200 °C. (b) EDS analysis of the silver films after sintering at 200 °C.

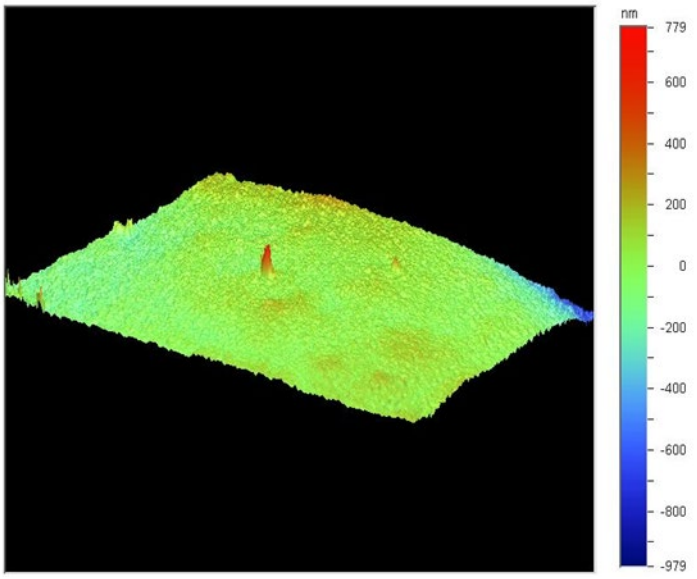

Figure 30. Surface profile image of the antenna after sintering at 200 °C.

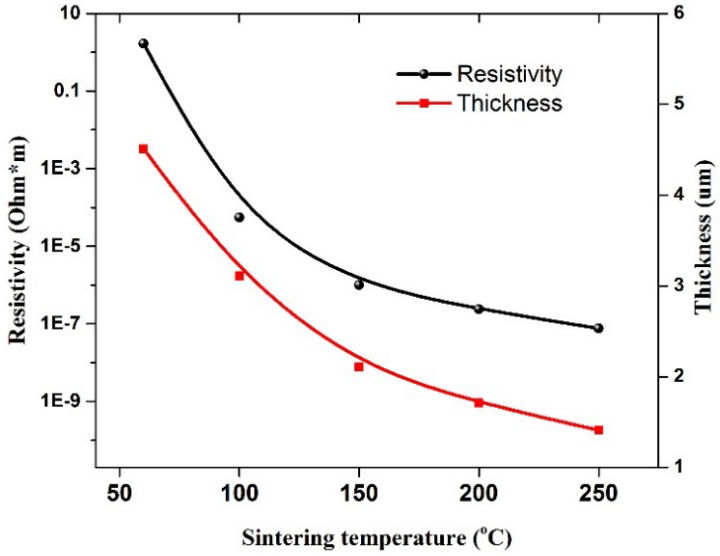

Figure 31. Change of resistivity of silver films with sintering temperature.

resistivity of AM micro-sensors deceased significantly as the increase of temperature, which achieved 1.41 μm and 7.64×10-8 Ω·m at sintering temperature of 250 °C, respectively. This study can be a new guide for future research and development towards rapidly manufacturing of micro-sensor for measuring shear stress and pressure.

The 3D printed antenna sensor was bonded on a printed circuit board and an SMA connector was installed. Conductive epoxy was used to connect the pin of the SMA connector to the micro strip transmission line. A photographic image of the assembled antenna sensor is shown in Figure 32. The radiation characteristics of the antenna sensor was measured using a vector network analyzer. As shown in Figure 33, the measured S11 parameter showed two resonant frequencies; one at 5.9 GHz and the other at -7.9 GHz. The return losses are -11.6 dB and -7.9 dB, respectively. These results are similar as the antenna sensor fabricated from printed circuit board and thus validate the effectiveness of the 3D printing technology.

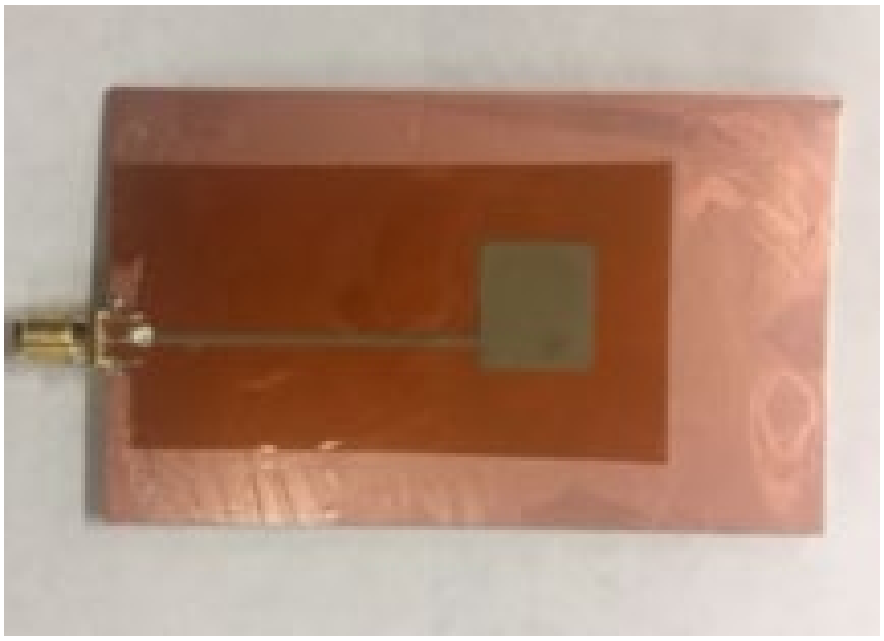

Figure 32. Antenna sensor bonded on a printed circuit board.

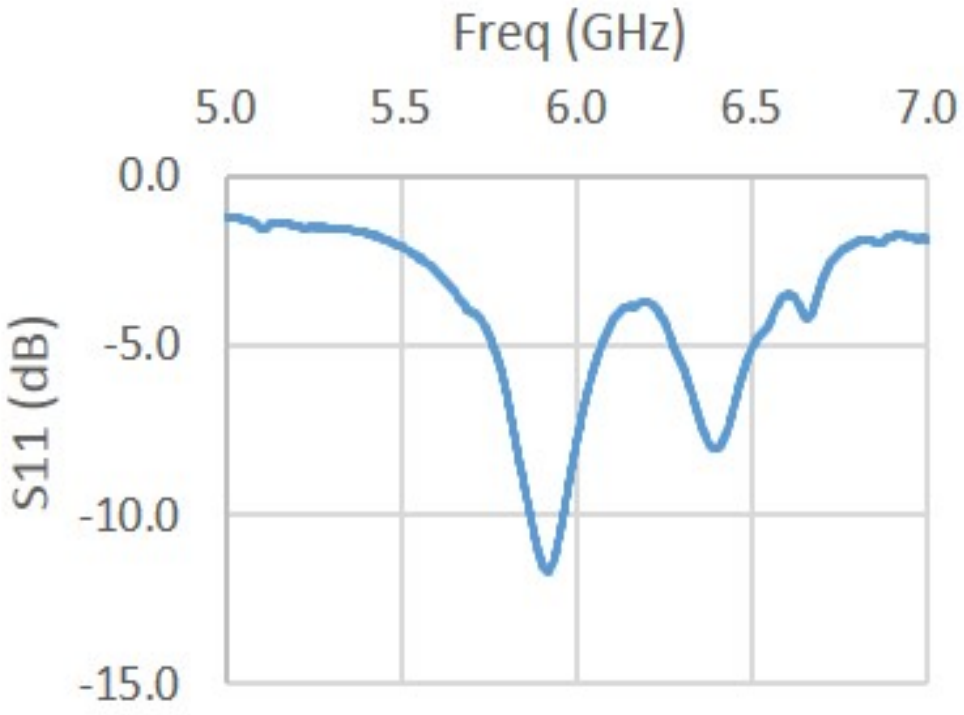

Figure 33. Measured S11 parameter of the antenna sensor.

References

[1] H. Jiang and H. Huang, "Simultaneous shear and pressure sensing based on patch antenna," in *SPIE Smart Structures and Materials+ Nondestructive Evaluation and Health Monitoring*, 2015, pp. 943533-943533-8.

[2] I. Mohammad and H. Huang, "Shear sensing based on a microstrip patch antenna," *Measurement Science and Technology,* vol. 23, p. 105705, 2012.

[3] F.-Y. Zhang, A. K. Prasad, and S. G. Advani, "Investigation of a copper etching technique to fabricate metallic gas diffusion media," *Journal of Micromechanics and Microengineering,* vol. 16, p. N23, 2006.

[4] Z. Kang, J. Mo, G. Yang, S. T. Retterer, D. A. Cullen, T. J. Toops*, et al.*, "Investigation of thin/well-tunable liquid/gas diffusion layers exhibiting superior multifunctional performance in low-temperature electrolytic water splitting " *Energy & Environmental Science* 2016.

[5] S. Deshmukh and H. Huang, "Wireless interrogation of passive antenna sensors," *Measurement Science and Technology,* vol. 21, p. 035201, 2010.

[6] K. Yorov, A. Sidorov, A. Y. Polyakov, I. Sukhorukova, D. Shtansky, W. Grünert*, et al.*, "Correction: Inkjet printing of silver rainbow colloids for SERS chips with polychromatic sensitivity," *RSC Advances,* vol. 6, pp. 39541-39541, 2016.

[7] J. Noh, D. Yeom, C. Lim, H. Cha, J. Han, J. Kim*, et al.*, "Scalability of roll-to-roll gravure-printed electrodes on plastic foils," *IEEE Transactions on Electronics Packaging Manufacturing,* vol. 33, pp. 275-283, 2010.

[8] X. Nie, H. Wang, and J. Zou, "Inkjet printing of silver citrate conductive ink on PET substrate," *Applied surface science,* vol. 261, pp. 554-560, 2012.

[9] J. Perelaer, M. Klokkenburg, C. E. Hendriks, and U. S. Schubert, "Microwave flash sintering of inkjet-printed silver tracks on polymer substrates," *Advanced Materials,* vol. 21, pp. 4830-4834, 2009.

[10] S. F. Jahn, T. Blaudeck, R. R. Baumann, A. Jakob, P. Ecorchard, T. Rüffer*, et al.*, "Inkjet Printing of Conductive Silver Patterns by Using the First Aqueous Particle-Free MOD Ink without Additional Stabilizing Ligands†," *Chemistry of Materials,* vol. 22, pp. 3067-3071, 2010.

[11] H.-H. Lee, K.-S. Chou, and K.-C. Huang, "Inkjet printing of nanosized silver colloids," *Nanotechnology,* vol. 16, p. 2436, 2005.

[12] V. Lakafosis, A. Rida, R. Vyas, L. Yang, S. Nikolaou, and M. M. Tentzeris, "Progress towards the first wireless sensor networks consisting of inkjet-printed, paper-based RFID-enabled sensor tags," *Proceedings of the IEEE,* vol. 98, pp. 1601-1609, 2010.

[13] Y. Kawahara, S. Hodges, B. S. Cook, C. Zhang, and G. D. Abowd, "Instant inkjet circuits: lab-based inkjet printing to support rapid prototyping of UbiComp devices," in *Proceedings of the 2013 ACM international joint conference on Pervasive and ubiquitous computing*, 2013, pp. 363-372.

[14] G. Allen, R. Bayles, W. Gile, and W. Jesser, "Small particle melting of pure metals," *Thin solid films,* vol. 144, pp. 297-308, 1986.

[15] W. Shen, X. Zhang, Q. Huang, Q. Xu, and W. Song, "Preparation of solid silver nanoparticles for inkjet printed flexible electronics with high conductivity," *Nanoscale,* vol. 6, pp. 1622-1628, 2014.

[16] J. Perelaer and U. S. Schubert, "Novel approaches for low temperature sintering of inkjet-printed inorganic nanoparticles for roll-to-roll (R2R) applications," *Journal of Materials Research,* vol. 28, pp. 564-573, 2013.

CHAPTER VII

2-D CONDUCTIVE MESOPOROUS BI-MATERIAL CATALYSTS (CMBMCS) ENABLES ULTRA-HIGH REACTION SITES AND EFFICIENCY FOR OXYGEN EVOLUTION REACTION

This chapter will be further edited and submitted for publication

I am fully responsible for the work submitted in this chapter, contributions from co-authors will be added prior to submission for publication.

7.1 Graphic abstract

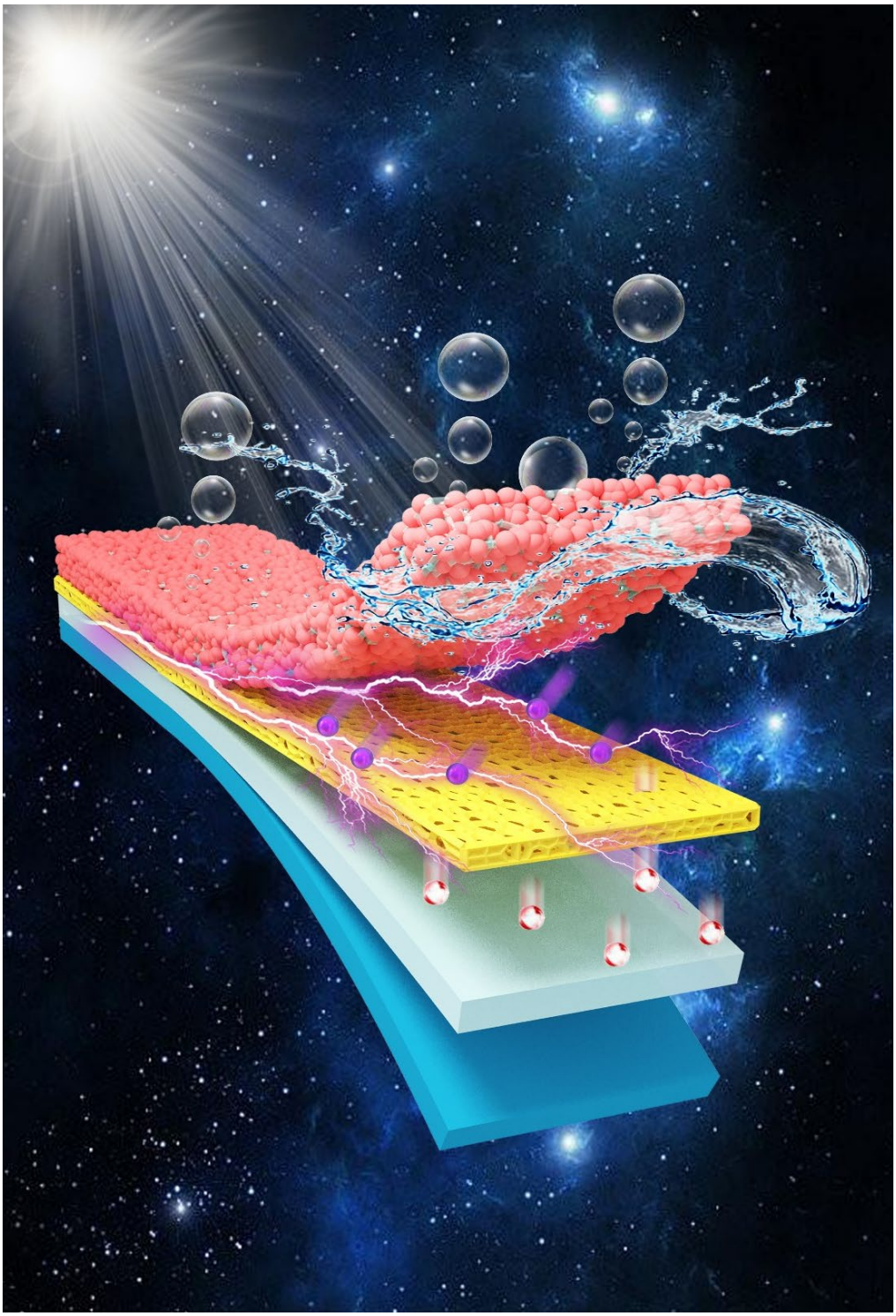

7.2 Abstract

Highly efficient and robust electrocatalysts with good conductivity, high cost-effectiveness and low loading are desirable for oxygen evolution reactions (OERs) associated with renewable energy storage. Here, highly conductive 2-D mesoporous bi-material catalysts (CMBMCs) were fabricated with advanced manufacturing approaches, which enable the ultra-high mass activity for OERs. The CMBMCs exhibit an excellent electrical conductivity (0.54 Ω/□) due to the conductive Au nanolayers (AuNLs), which also allow the proton transport though the mesopores. Furthermore, the novel structure of the CMBMCs facilitates the direct investigation of influence of conductivity on OER kinetics, and enables the establishment of relationship between the conductivity and reaction sites. The low loading of noble-metal catalysts (0.1195 mg/cm^2) can achieve 3 times faster OER kinetics than the conventional IrO_2 catalyst layer (CL).

7.3 Introduction

Power generated from renewable energy sources is widely considered as an alternative to the carbon-based fuel, which is unrenewable and release excess amounts of carbon dioxide and other hazardous gases[1-5]. The renewable energies have grown rapidly, for example, the wind and solar energies increased by 19% and 42% in the last 10 years, respectively[6]. However, they are typically intermittent and undulating, which will cause the destabilization of electricity grids. Thus, efficient energy storage or conversion systems are

highly demanded to overcome its intermittence, and hydrogen production from electrochemical water splitting is a promising method [2, 7, 8].

The oxygen evolution reaction (OER) at anode electrode in water splitting is a four electron-proton coupled reaction which requires a higher overpotential, and its slow kinetics greatly limit the hydrogen production [9-12]. So far, breakthroughs have been made regarding the discovery of perovskites[13], Co, Mo[14], Ni[15] and Fe[12] as the alternatives, which can break the limitation of scarcity of noble metals, but their performances, such as the activation kinetics, overpotential, durability, etc. are still not desirable. At this moment the widely used commercial catalysts are still made of precious metals, include Ir and Ru, which provide good OER catalytic activity and stability[2, 10, 11, 16]. Nevertheless, their wide applications for hydrogen economy are limited by the scarcity and the associated high cost.

For proton exchange membrane electrolyzer cells (PEMECs), the OERs only occur on the "triple-phase boundaries" (TPBs), where contact the electrolyte, water, and electrically connected catalyst [17, 18]. Furthermore, the in-plane ohmic resistivity of those catalyst layer (CL) is extremely large (~1000 times) compared to PtB CL for hydrogen evolution reaction (HER) and metal layers, which limits the electrochemical reaction locations only in 1D sites (at the edge of liquid and gas diffusion layer (LGDL)), and leads to a waste of middle regions of the CL and a higher overpotential[18, 19]. The 1-dimensional (1D) reaction sites need to be enlarged to 2D, so as to increase the volumetric catalyst activity and reduce the cost. Carbon based materials (graphene and carbon nanotubes (CNTs),

carbon paper), Ti based materials, Sn based and W-based materials were used as supports for catalyst, but most researches focused on enhancing the support–electrocatalyst interaction [20, 21]. Moreover, for testing conventional electrochemical catalysts, the 3 electrode assembles with a thin film rotating disk electrode (RDE) are usually employed, and the catalysts are mixed with conductive materials such as carbon[13], or the RDE is made of glassy carbon[14]. Those methods ignored the impact of resistivity of electrode. But in real catalytic reactions in full cells, the electrical conductivity of catalysts is essential for their electrochemical performance, and cannot be neglected. Following this line of inquiry, developing and investigating conductive catalysts without sacrificing its electrochemical activity is highly needed. To the best of our knowledge, only few researches have been done to study the electronic and protonic conductivity of CL.

Herein, a series of new 2-D conductive mesoporous bi-material catalysts (CMBMCs) were manufactured by using spay printing, sputter coating, and 3D inkjet printing, subsequently (Figure 34). Instead of using conventional configuration of PEMECs, a unique coplanar PEMEC was developed to better investigate the reaction and performance of CMBMCs. The conductive tracks (AuNLs) were laid on the spay printed nafion membrane, then the CLs were inkjet-printed to cover the conductive tracks. Compared with the CL without conductive tracks, the highly conductive CLs (as low as 0.54 Ω/□) provide a larger reaction area and more reaction sites. The relationship between conductivity and reaction length is also quantitatively investigated via high-speed and microscale visualization systems (HSMVS). The CMBMCs with ultralow catalyst loading (0.1195

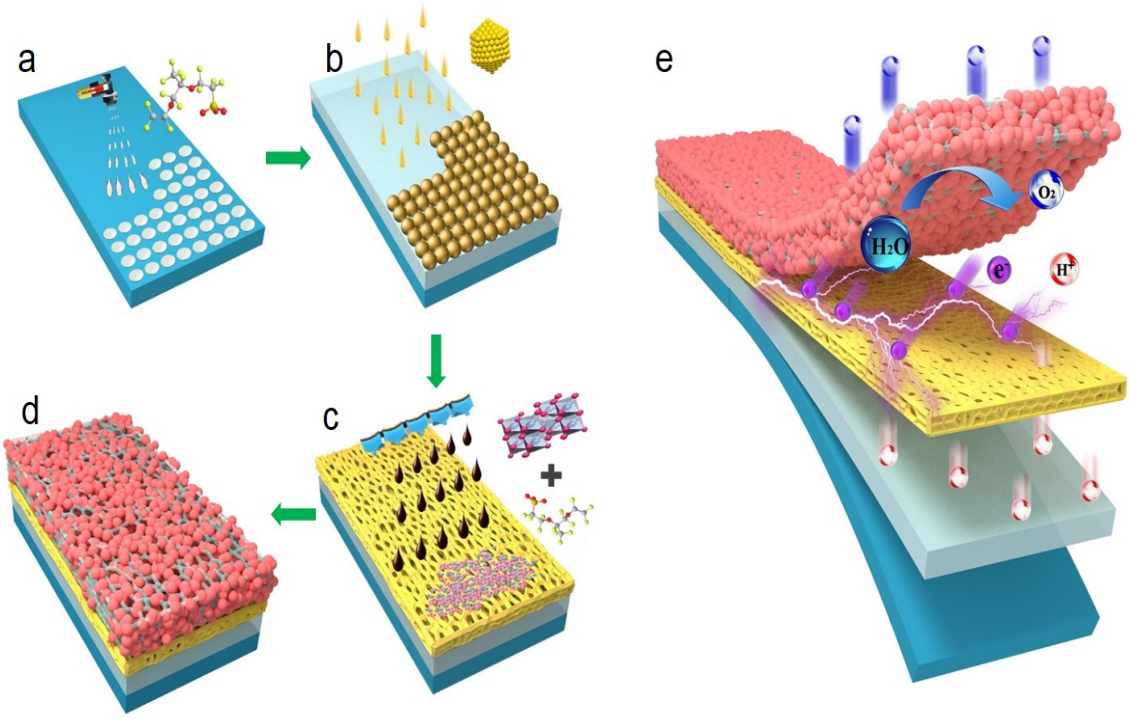

Figure 34. Synthetic process and reaction pathway of CMBMCs. (a) Spraying of nafion membrane, (b) depositing AuNLs with sputter coating, and (c) inkjet printing of CLs with IrO_2 NP ink. (e) Reaction pathway on CMBMCs.

mg/cm^2) can achieve 3 times faster OER kinetics than the conventional IrO_2 CL. The CMBMCs, which integrate the advantages of high electrical conductivity of metals and high electrochemical catalytic activity of noble metal oxide, are among the most active catalysts.

7.4 Fabrication method

7.4.1 Synthesis of CMBMCs

For the nafion membrane, 2 ml nafion solution (5%) was mixed with 4 ml IPA, then was sprayed on the cleaned Teflon (125 um thick, 40mm × 33mm), and subsequently dried to form a thin layer of nafion membrane. The temperature was 100 °C for faster evaporating of IPA. Au nano-layers (AuNL) with a dimension of 0.5 mm × 10 mm were manufactured using sputtering coating onto the sprayed nafion membrane with a patterned mask. The thicknesses were controlled by sputtering time, and roughly measured by weighting the reference Ti foil before and after sputter coating with a microbalance, and then calculated with gold density. For CL synthesis, IrO_2 NP (3151663, FuelCellStore) with the particle size of ~ 12 nm and surface area of ~ 15 m²/g was used. Typical catalyst inks were prepared by gently mixing IrO_2 NP (100 mg), nafion solution (10 wt%, 100 mg), ethylene glycol (3 g), and isopropanol (1.5 g). Then the mixtures were sonicated for 2h for fully mixing. The obtained IrO_2 NP ink was loaded into a 10 pL disposable piezo ‘‘inkjet” cartridge with 16-nozzle print head, the nozzles had a diameter of 20 μm. And the ink was printed by using a Dimatix materials printer (DMP-2831, Fujifilm) with a dropping space of 25 μm

and a time interval of 180 seconds between each layer. After the fabrication, the CMBMCs were dried on the paper tray for at least 60 min. For the channel plate, it was designed and processed using Cura 2.0, followed by printing with 3D printer (Ultimaker 2, Ultimaker) and ABS filament (Ultimaker NFC ABS - Pearl Gold) in solid infill (100%) mode.

7.4.2 Ex-situ Characterization

Scanning electron microscopy (SEM) performed on a field emission SEM JEOL JSM-6320F with an accelerating voltage of 0.5 – 30 kV, a magnification of 250 x~650,000 x and a 5-axis specimen mount. The electrical resistances were measured using 4-probe micro-ohmmeter (6250, AEMC INSTRUMENTS) with a resolution of 1μΩ. For electrochemical investigation of CMBMCs with different thicknesses of AuNLs, the samples were placed at the bottom of flow channel of 3D printed plate, and a Ti foil stripe was connect to one side of CMBMCs which were used as anode electrode. All the electrochemical tests were conducted at room temperature and atmospheric pressure. A 99.95% pure platinum square wire (4582, Surepure Chemetals) with cross-section of 0.5 mm× 0.5 mm was used as cathode catalyst. Then the assembled parts were incorporated into a cell with clear Acrylic plate. The endplate was opened a window at the center for direct observation through the Acrylic plate. DI water was supplied into the flow channel using a diaphragm liquid pump (SIMDOS 02, KNF Neuberger) with a flow rate of 2 ml/min. All tests were conducted at 22 °C and atmospheric pressure. A potentiostat SP-300 chassis with a 5 V/10 A booster from Bio-Logic was used to study the electrochemical performance of those samples. Polarization curves were scanned from 0 to 20 mA/cm^2 with

a scan rate of 50 uA/s. The LSV curves were gathered from 0 to 2.5 V with a scan rate of 10 mV/s. The high frequency resistance (HFR) tests were conducted at 3 kHz. For visualization, a high-speed camera (Phantom V711) and long working distance optical system (Infinity K2 DistaMax) were used in the high-speed and micro-scale visualization system (HMVS). Cyclic voltammetrys (CVs), scanned from 0.9 V to 1.0 V at 5, 10, 20, 40, 60, 80, and 100 mV/s, were used to measure electrochemical surface area (ECSA). The stability tests were conducted by Chronopotentilmetry technique at 1.25 mA/cm^2 for more than 18 h.

7.5 Results

7.5.1 Ex-situ characterization

We developed a method for fabricating high electrical conductivity catalyst layer with low catalyst loading via three advanced manufacturing methods (Figure 34). Firstly, a layer of nafion membrane was spay printed with nafion solution on the Polytetrafluoroethylene (PTFE) film (Figure 34a), and followed by selectively sputter coating of AuNLs on the nafion membrane (Figure 34b). The last step was to print IrO_2 catalyst ink on the AuNLs with 3D inkjet printing (Figure 34c), and the CMBMC is shown as Figure 34d. We expect water molecule can split into electrons, protons and oxygen on IrO_2 CL, and then electrons can be freely transported away by AuNLs, and protons can pass through the mesopores on AuNLs to reach nafion membrane and move to cathode side easily (Figure 34e). From the SEM images (Figure 35), it is apparent that 18 um thick Nafion membrane is sprayed

uniformly on the PTFE film. To control the thickness of Au layer, the coating time was adjusted, and the thicknesses of sputter coated AuNLs vary from 3 to 197 nm. As shown in Figure 35a-b, the printed IrO_2 CLs are distributed uniformly on AuNLs, and mesopores are found on catalyst layer, which will facilitate the diffusion of protons and water molecules.

For a thin enough AuNL (< 5 nm), only discrete Au nanoclusters (AuNCs) will form on the substrate[22]. When the sputtering time increases, the clusters grow and merge among adjacent AuNCs, and a transition from the electrical discontinuous to electrical continuous of metal layers will occurs when the AuNL is thicker than the critical effective film thickness (≈ 6 nm)[23]. Furthermore, well defined mesopores notably appear along with the emerging of AuNCs. And the mesopores would promote the transport of proton from catalysts to the nafion membrane through AuNLs. As the continuously increasing sputtering duration, the mesopores are reduced, and are blocked by Au crystals[24]. Between completely change from the electrical discontinuous to continuous and transition from discrete clusters to AuNLs, there should have a transition state which possesses both electrical discontinuous and discrete clusters. At this state, the Au clusters are connected together to form a net, but there are still mesoporous gaps among clusters. And electrons can transport though the Au clusters net, and proton can pass through the Au layer via the gaps.

The sheet resistance for CMBMCs as a function of the AuNL thickness is shown in Figure 35d. Initially, the CMBMC-0AuNL (CMBMC with 0 nm AuNL) shows an

extremely large sheet resistance (~2200 Ω/□) as a result of large electrical resistivity of IrO_2 CL[18]. And CMBMC-3AuNL share almost the same sheet resistance as CMBMC-0AuNL, which indicate the 3 nm AuNL does not exhibit electrical conductivity when the AuNCs are not interconnected. A pronounced change (from 2200 to 32 Ω/□) between 3-10 nm range of Au NCs thickness is observed. This is due to the transition of AuNLs from discontinuous to continuous layer, and the AuNLs are thinner than the mean free path (≈ 25 nm) of electrons in Au[23, 25].

This phenomenon is also confirmed from the SEM image of AuNLs[23, 24]. With the continuing sputtering process, the sheet resistance decreased linearly with the Au thickness due to the increase of cross-section of electron transport path. Eventually, CMBMC achieves an ultra-low value of 0.54 Ω/□ with 197 nm thick AuNL. The theoretical sheet resistances calculated with the resistivity of Au (2.20×10^{-8} Ω·m) exhibit smaller values than those of CMBMCs. This difference is attributed to the roughness of the substrate, which are not considered during the theoretical calculation. While the real substrate is sprayed Nafion membrane which have a large roughness, especially at small thickness.

More importantly, the discontinuances of thin AuNLs and limitation of mean free path for conduction electrons are also not considered during the theoretical simulation[26]. As shown in Figure 35d, even though the nafion membrane expends after absorbing water molecule during electrochemical test, the sheet resistances of AuNLs remain almost the same before and after electrochemical testing, indicating AuNLs are not corroded and have a good stability in harsh anodic environment.

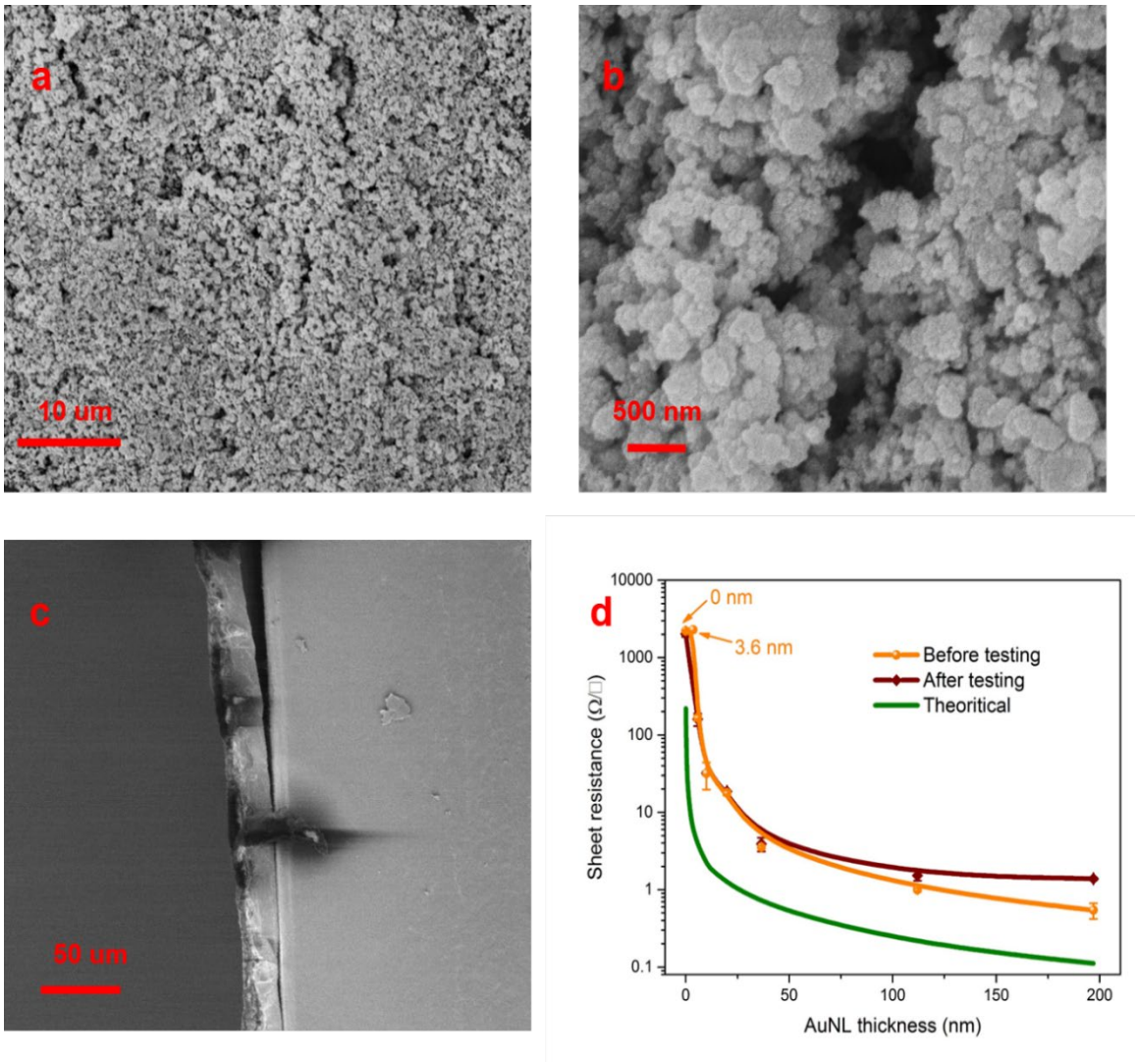

Figure 35. Top-view SEM images of CMBMCs with (a) 10 um scale bar and with (b) 500 nm scale bar. (c) Cross-section SEM image of CMBMCs. (d) Sheet resistances of CMBMCs with different thicknesses of AuNLs before testing, after testing, and in theoretical.

7.5.2 Electrocatalystic water splitting

For the water splitting test, the conventional three-electrochemical cell with electrically conductive working electrodes, such as 3-electrode cell and half-cell, could not truly reflect the catalytic performance of catalyst with different electrical conductivity in a real electrolyzer cell. Therefore, we developed a novel testing station as shown in Figure 39. The unique coplanar electrodes contain cathode and anode electrodes at the same plane. The anode electrode is the CMBMC, and the cathode electrode is a 0.5 mm wide square Platinum (Pt) wire. It needs to be mentioned that the Pt wire has a ultra-low resistivity ($\sim 10^{-7}$ Ω·m) and a large cross-section area, so the influence of resistivity of cathode electrode can be eliminated in all tests. The electrode sensor adaptors of test station are connected to the top side of the electrode strip and wire, which allows to investigate the mechanism of how the current transports and reaction occurs on the CMBMCs. And a cell with flow channel is 3D printed from plastic PLA filaments for electrodes aligning and mass transporting. Then the galvanostatic performances of the electrodes at room temperature and atmospheric pressure are carried out.

As shown by the polarization curves in Figure 36a, the CMBMCs with 0 and 3 nm Au NLs almost share the same trend, and the performances are much worse than other samples, even though IrO_2 is one of the best catalyst for OER[27]. Interestingly, with the continuously increasing thickness, lower voltages are achieved with thicker Au NLs below 112 nm, which indicate the better overall water splitting performances. However, when the

thickness keeps increasing (>112 nm), the performance is weakened even its sheet resistivity is lower (Figure 35d).

Meanwhile, the activation polarization in the low current density range (< 1.8 mA/cm^2) and the ohmic polarization in the high current density range (> 5 mA/cm^2) show different relationships with Au NLs thickness, which need to be further investigated. According to the linear sweep voltammograms (LSV) in Figure 36b, the 112 nm Au NL delivered the smallest overpotential in those samples, and exhibits a smaller onset potential of ≈ 1.45 V. The current densities at 1.7 V are in the order of 112nm (3.14 mA/cm^2) > 36 nm (2.07 mA/cm^2) > 197 nm (1.85 mA/cm^2) > 10 nm (1.68 mA/cm^2) > 5 nm (1.34 mA/cm^2) > 3.6 nm (0.55 mA/cm^2) ≈ 0 nm (0.57 mA/cm^2). This demonstrates the superior electrocatalytic activity of CMBMC with 112 nm and 36 nm AuNLs compared.

However, the LSV curves do not exclude the influence of ohmic resistance. Therefore, Tafel plots derived from LSVs results with IR-correction are also investigated (Figure 36c). The superior OER performance of CMBMC-112 AuNL (173 mV dec^{-1}, Figure 36c) is verified by the Tafel plots than those of 197nm (294 mV dec^{-1}), 10 nm (189 mV dec^{-1}), 5 nm (324 mV dec^{-1}), 3 nm (413 mV dec^{-1}) and 0 nm (429 mV dec^{-1}), which imply the much faster reaction kinetics. Notably, the Tafel slope for 36 nm (145 mV dec^{-1}) is even smaller than that for 112 nm, indicates the fastest reaction kinetics.

It is assumed that too thick AuNLs will weaken the OER reaction kinetics, which can be revealed by an increasing distance between reaction site (catalyst) and nafion membrane, and by the decreasing mesopores on the AuNLs. It is notable that the CMBMC-

0AuNL shows a much lower catalytic activity than those observed for IrO_2 in TES (three electrodes system)[14]. This is because the CL was usually deposited on the conductive substrate in the publications[14, 27], which eliminate the effect of ultra-high electrical resistivity of catalysts, while the high resistivity can significantly reduce the catalytic activity in the real electrolyzer cell.

To reveal the reason of high catalytic activity of CMBMCs, cyclic voltammetrys (CVs) scanned from 0.9 V to 1.0 V are used to measure electrochemical surface area (ECSA)[28]. ECSA is calculated based on the CV measurements at different scan rate by extracting the double-layer capacitance (C_{dl}). The resulted current density plotted against the scan rate is shown in Figure 40, and the differences in current density variation ($\Delta J = J_a - J_c$) at the no faradic region (0.95 V) plotted as a function of scan rate fitted to a linear regression enables the estimation of C_{dl} (Figure 36d) [29, 30]. C_{dl} for CMBMCs with 197, 112, 10, 5, 3, and 0 nm AuNLs is 610, 816, 493, 280, 179 and 208 μF·cm^{-2}, respectively. During the estimating of ECSA, we assume it will scale proportionally to the total surface area, The voltammetric charge, q*, is calculated by integrating the CV over the whole potential range [31].

According to equation [16]

$$ECSA = \frac{C_{dl}}{C_s} \tag{7-1}$$

Where C_s is the specific capacitance of catalysts, and we use a typical value of 40 μF·cm^2 [14, 16].

Figure 36. Electrochemical performance of CMBMCs with AuNL thicknesses range from 0-197 nm in DI water. (a) Polarization curves corresponding to CMBMCs with different AuNL thickness, clearly indicating the AuNLs can improve the performance, and an optimal thickness is obtained. (b) LSV plots and (c) the corresponding Tafel slopes of CMBMCs. (d) Fitting Plots showing the extraction of C_{dl} for each type of CMBMCs with differences in current density variation ($\Delta J = J_a - J_c$) at the no faradic region (1.25 V). (e) HFRs recorded at 3 KHz frequency. (f) Chronopotentilmetry curves of CMBMCs at a constant current density of 1.25 mA/cm^2 for 20 h.

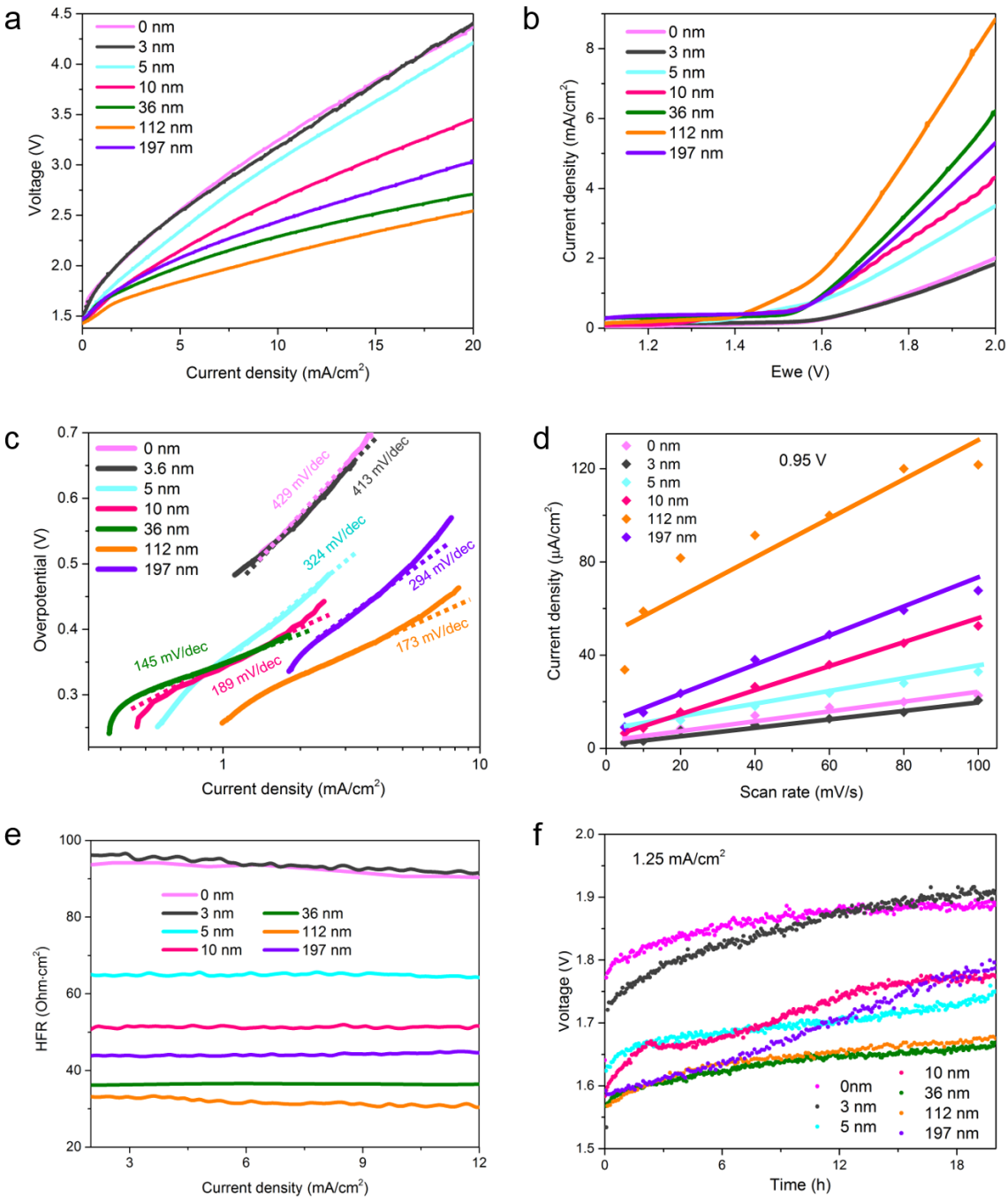
a
Voltage (V)
Current density (mA/cm²)
0 nm
3 nm
5 nm
10 nm
36 nm
112 nm
197 nm
b
Current density (mA/cm²)
Ewe (V)
c
Overpotential (V)
Current density (mA/cm²)
0 nm
3.6 nm
5 nm
10 nm
36 nm
112 nm
197 nm
429 mV/dec
413 mV/dec
324 mV/dec
294 mV/dec
145 mV/dec
189 mV/dec
173 mV/dec
d
Current density (μA/cm²)
Scan rate (mV/s)
0.95 V
e
HFR (Ohm·cm²)
Current density (mA/cm²)
f
1.25 mA/cm²
Voltage (V)
Time (h)
0nm
3 nm
5 nm
10 nm
36 nm
112 nm
197 nm

The CMBMCs show the ECSA of 15.3, 20.4, 12.3, 4.5 and 5.2 cm^2 for 112, 197, 5, 3, 0 nm, respectively. Therefore, CMBMC-112AuNL processes the most active sites for OER among all the samples, which is 3 times higher than that of CMBMC-0AuNL and CMBMC-3AuNL, and the more active sites are responsible for its excellent electrocatalytic activity.

HFR can provide the information of ohmic resistance of the whole cell at high frequency (~ 3 kHz), which include the protonic and electronic resistance resistances, and the catalytic kinetics and concentration overpotential are excluded. With the increase of AuNLs thickness (0 - 112 nm), it is found that the HFR decreases accordingly (93 - 31 $\Omega \cdot cm^2$) in Figure 36e. Notably, the increase of HFR is observed when the thickness is larger than 112 nm, this phenomenon is corresponded to the slope of polarization curves at high current density (Figure 36a). This phenomenon indicates that the overall transport of electron and proton on the CMBMCs are facilitated with larger thickness in the range of 0 ~112 nm. Firstly, a lower resistance of the CMBMCs can be obtained with thicker AuNLs. Secondly, when CL resistance is reduced, and more nafion membrane will take part in the proton transport from anode side to cathode side, and lead to a smaller protonic resistance in the nafion membrane, which would be demonstrated by the following section. Notice that the HFR increases with197 nm AuNLs. Even though the electron conductivity of CMBMCs was enhanced with thicker AuNLs, the active sites were limited, which lead to the less and longer proton transport paths from catalyst layer to the nafion membrane through

mesopores on the AuNL. This further results in a large proton transport resistance and higher HFR.

Apart from the activity, stability or durability is also a critical criterion to evaluate catalytic activity of electrocatalysts. The CMBMCs exhibit superior stability as confirmed by prolonged potentiostatic polarization experiments (fixed at 1.25 mA/cm^2 for 20 hours, Figure 36f). Remarkably, the overpotentials for CMBMC-36AuNL and CMBMC-112AuNL remains almost constant for the last 12 h, whereas that for other CMBMCs increased distinctly. This phenomenon suggests the proper thickness of AuNLs can not only improve the performance of WE, but also enhance the electrochemical stability. The good stability is not only due to the stability of IrO_2, but also due to the similar sheet resistance of CMBMCs before and after testing as a result of good corrosion resistance of Au toward anodic oxidation[32] (Figure 35d).

7.5.3 Visualization and current mapping

To gain further insight into the mechanism of the influence of AuNLs on the catalytic activity of CMBMCs, visualizations and simulation were conducted. A HMVS was introduced into the test station, so as to enable direct investigation of the electrochemical reaction on the CMBMCs, which allows the quantification of reaction area and length. From the transparent window, the reactions of OER and HER can be visualized by the generation of oxygen and hydrogen bubbles at anode (CMBMCs) and cathode (Pt wire) simultaneously at a flow of 2 mL/s and a current of 500 uA. The bubble nucleation or generation sites have been confirmed to be the electrochemical reaction sites for OER and

HER[18, 33]. And the local bubble growth rate indicates the intensity of reaction at the specific region along with the different CMBMCs, so we can quantitatively investigate the relationship between reaction sites and sheet resistances.

During the simulation and current mapping, we take the electronic resistance on the CL and the protonic resistance on proton membrane into the circuit (Figure 41), and the reduction of current along with the CL is equal to the increment of protons or electrons (Figure 37a). It need to be mentioned that the number of generated protons is equal to that of generated electrons, and is 4 times as many as that of generated oxygen molecules[1]. The detailed simulation analytical method is provided in our former publication[33]. The proton current distributions versus distance in CMBMCs with 0, 5, 10 nm AuNLs are shows in Figure 37b. The proton current on CMBMC-0AuNL drops dramatically from 0.21 mA to almost 0 mA, and that on CMBMC-5AuNL shows a smoother drop. Notably, a uniform proton current distribution is achieved on the CMBMC-10AuNL, which implies the OER reaction can occurs all over the CL. The inset of Figure 37b shows the CMBMC-10AuNL has a smaller slope, and this confirms the electric current distribution is more uniform on the 10 nm AuNL. The visualization and current mapping results show a good agreement in Figure 37c-e. For the CMBMC-0AuNL, the oxygen bubbles only generate at the very top of the catalyst layer (Figure 37c), and no bubbles are found at other area, that means the OER reaction do not occur at other area, and most of the catalyst is wasted. This phenomenon is also found on CMBMC-3AuNL (Figure 42), which also explain the similar performance of those two samples. Interestingly, the visualization image of

Figure 37. Simulation and visualization analysis of CMBMCs with different AuNL thicknesses. (a) Schematic of in-plane current and proton transport on the CMBMCs. (b) Proton current or generated electron current distribution along the CMBMCs; the inset of (b) Current density distribution along the CMBMC. Visualization of distribution of OER reaction sites, and current mapping along the CMBMC-0AuNL (c), CMBMC-5AuNL (d), and CMBMC-10AuNL (e).

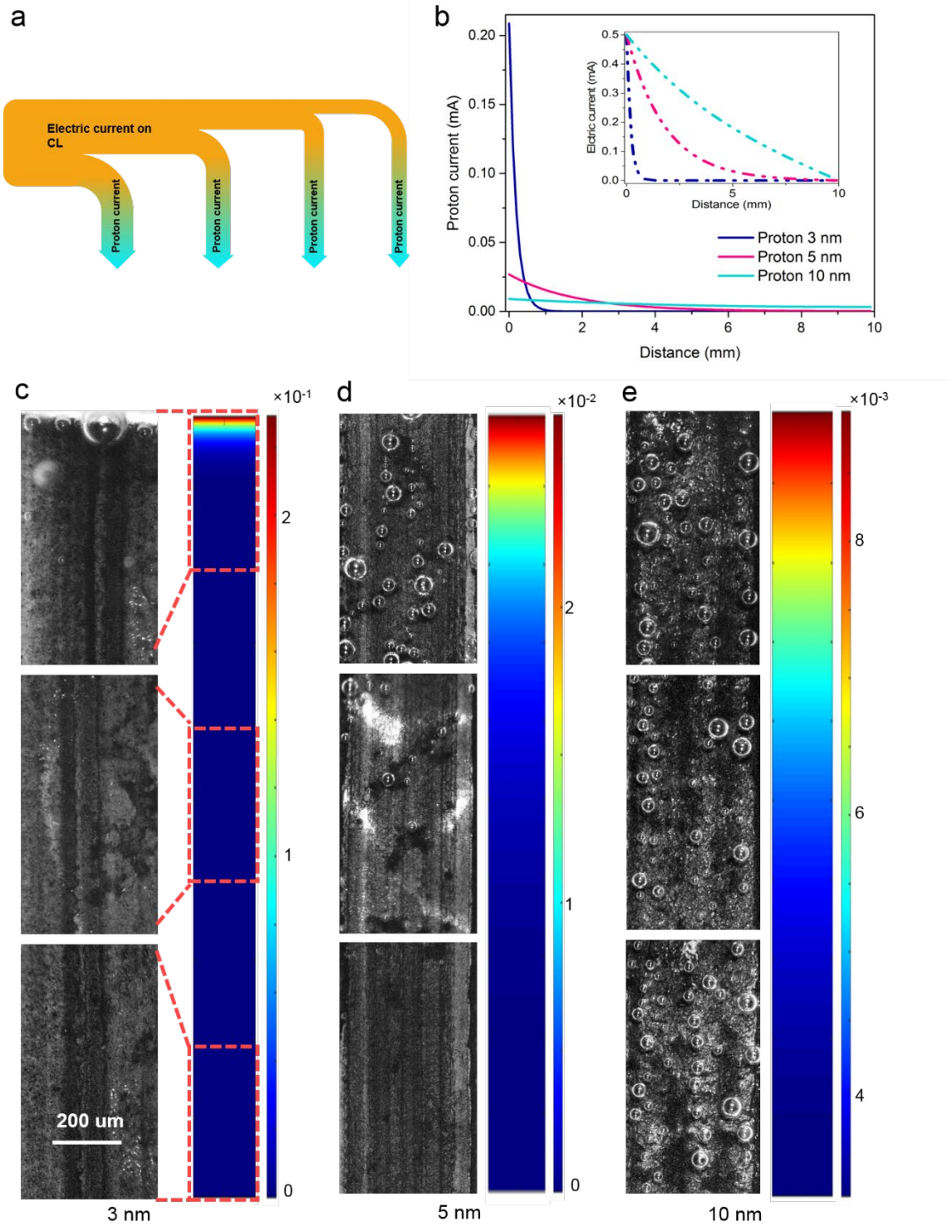
a
Electric current on CL
Proton current
Proton current
Proton current
Proton current
b
Proton current (mA)
Distance (mm)
Electric current (mA)
Distance (mm)
Proton 3 nm
Proton 5 nm
Proton 10 nm
c
×10-1
200 um
3 nm
d
×10-2
5 nm
e
×10-3
10 nm

CMBMC-5AuNL shows the bubbles appeared at the top half part of catalyst layer, even though its AuNL is only 2 nm thicker than that of CMBMC-3AuNL. However, 5.6 nm AuNL is still not thick enough for activating all the CL areas on CMBMC. For CMBMC-10AuNL, the oxygen bubbles can be observed all over the catalyst layer, which illustrates all the regions are activated. In the literature, the field-assisted pure water electrolysis only occurs at the edge of the anode electrode. [32] In our experiments, it needs to be highlighted that the bubbles can grow not only at the right and left edge of the AuNLs, but also the center part. This is attributed to the mesopores on the AuNLs, which contributes to broadened reaction sites by ensuring effective proton transport to nafion membrane, while the ion transport in the literature is hindered by the silicon nitride film in the literature[32]. If the reaction only occurs at the very top of the CL, which means the electron and proton transport paths are very limited, and lead to the large resistance. Actually, instead of TPBs, four-way opened catalysts (FWOCs) are more accurate for the boundary that carries out the reaction, especially in PEMECs. Since the reaction can only occur on the catalyst that have four paths for the water molecule-in, oxygen-out, current-in and proton out. Water molecule-in and oxygen-out paths mean a route to transport liquid and gas mass between catalyst and surroundings. The current-in path requires a good electrical conductor to the anode electrode, and the proton-out path means a good proton carrier to the cathode electrode.

7.5.4 Performance with different catalyst loadings

CMBMCs have different structures compared to the conventional CL. So the insight into the influence of catalyst loadings need to be investigated by adjusting the number of printing layers of IrO_2 CL. And the 1, 5, 10, and 20 layers are corresponding to 0.0299, 0.1195, 0.2390, and 0.4780 mg/cm^2, respectively, which are much lower than the commonly used commercial MEA[34, 35]. The electrochemical performances of CMBMCs with different IrO_2 loading are shown in Figure 38. The polarization curves reveal the Bare AuNL has the poorest performance, and the turning point is at around 2.2 V, which indicates a weak catalytic activity and high overpotential for OER (Figure 37a) [1]. Ever though the 1 layer CMBMC shows better performance, but it is still no comparable to those with higher loading. The 5, 10 and 20 layer CMBMCs almost share the same performance. Extracted from IR-correction LSV (Figure 43), the Tafel slops confirms the remarkable low catalytic activity of bare AuNL (1040 mV/dec^{-1}), even though some nanostructured Au materials showed high catalyst activity in several oxidation reactions (Figure 37b) [36, 37]. And the extremely low IrO_2 loading (0.4780 mg/cm^2) results in a sufficient OER performance (225 mV/dec^{-1}) compared with higher loading. When the IrO_2 loading is ultra-low, there will be a non-uniform catalyst layer on the AuNL, and consequently the catalyst is not enough for OER, which result in larger Tafel slop[35, 38]. Even the Tafel plots for 5 layers (130 mV/dec^{-1}), 10 layers (144 mV/dec^{-1}), and 20 layers (173 mV/dec^{-1}) are similar, the 5 layer CMBMC provide a higher catalytic kinetics for OER. The proton transport resistance to the catalytic sites located at the surface

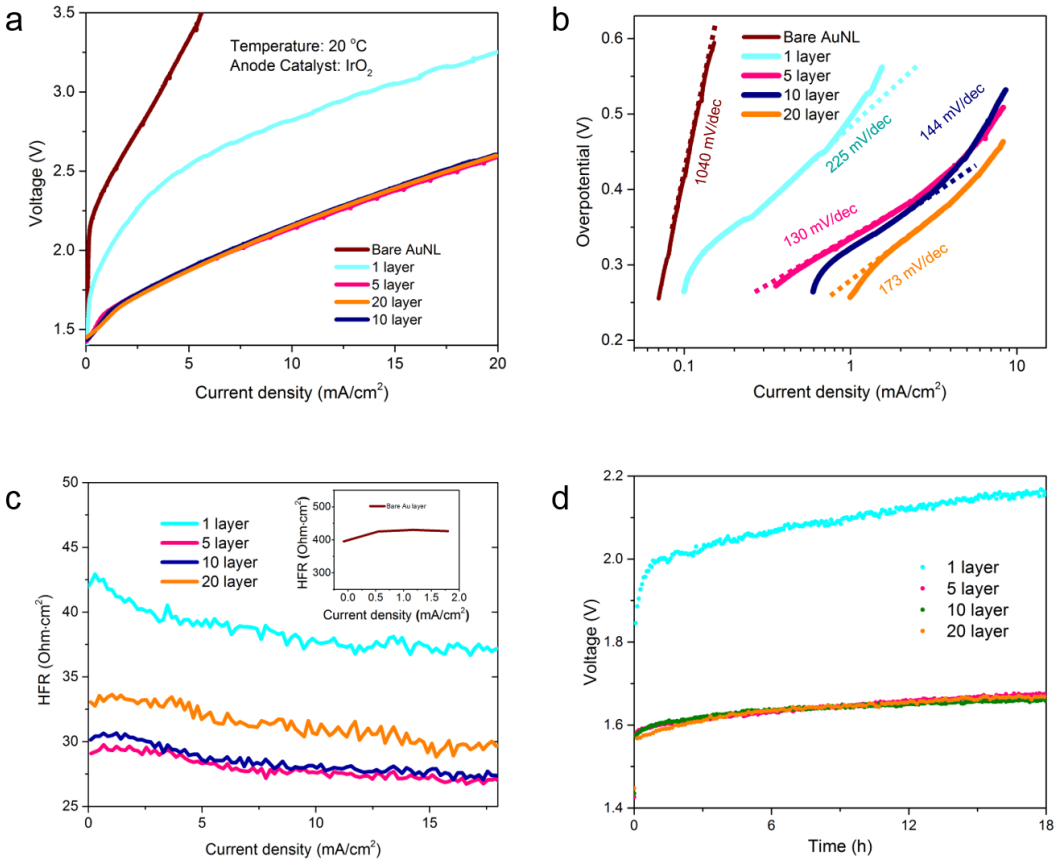

Figure 38. Electrochemical performance of CMBMCs with different IrO_2 loadings. (a) Polarization curves corresponding to CMBMCs with printed layers range from 0-20. (b) Tafel slopes of CMBMCs extracted from IR-correction LSV plots. (c) HFRs recorded at 3 KHz frequency. (d) Chronopotentilmetry curves of CMBMCs at a constant current density of 1.25 mA/cm^2 for 18 hours.

of IrO_2 NPs inside the CL is expected to be more prominent in thick electrode, which can explain the higher Tafel plots for 10 and 20 layer CMBMC [35, 38]. The HFRs in Figure 37c demonstrate the 5 layer CMBMC process the smallest ohmic resistance, and bare AuNL shows an extremely large value (~ 400 Ohm·cm^2). As proven in the previous section, the lack of active sites can lead to the less and longer electron and proton transport path, and further result in a higher HFR. During the Chronopotentiometry test for 18 h, 1 layer CMBMC shows a worse stability than other electrodes (Figure 37d). Firstly, the high overpotential at certain current density can lead to a corrosion and oxidization of catalyst layers. Besides, the AuNL is not well covered by CL with an extremely low loading, so it will be easily broken as a results of nafion membrane swelling after absorbing water.

7.6 Summary

In summary, we developed a facile method for fabricating 2-D CMBMCs with advanced manufacturing, which enable the excellent electrical conductivity (0.54 Ω/□) and ultra-high mass activity for OERs. We also discovered the mesopores on the sputter coated AuNLs allow the transport of proton from reaction sites to nafion membrane. Moreover, the novel structure of the CMBMCs facilitates the direct investigation of influence of conductivity on OER kinetics, thus relationship between conductivity and reaction length is established. At last, the low loading of noble-metal catalyst (0.1195 mg/cm^2) can achieve 3 times faster OER kinetics than conventional IrO_2 CL.

References

[1] S. Park, Y. Shao, J. Liu, and Y. Wang, "Oxygen electrocatalysts for water electrolyzers and reversible fuel cells: status and perspective," *Energy & Environmental Science,* vol. 5, pp. 9331-9344, 2012.

[2] Z. W. Seh, J. Kibsgaard, C. F. Dickens, I. Chorkendorff, J. K. Nørskov, and T. F. Jaramillo, "Combining theory and experiment in electrocatalysis: Insights into materials design," *Science,* vol. 355, p. eaad4998, 2017.

[3] B. C. Steele and A. Heinzel, "Materials for fuel-cell technologies," *Nature,* vol. 414, pp. 345-352, 2001.

[4] J. A. Turner, "Sustainable hydrogen production," *Science,* vol. 305, pp. 972-974, 2004.

[5] S. J. Davis, K. Caldeira, and H. D. Matthews, "Future CO2 emissions and climate change from existing energy infrastructure," *Science,* vol. 329, pp. 1330-1333, 2010.

[6] A. Sternberg and A. Bardow, "Power-to-What?–Environmental assessment of energy storage systems," *Energy & Environmental Science,* vol. 8, pp. 389-400, 2015.

[7] S. Y. Tee, K. Y. Win, W. S. Teo, L. D. Koh, S. Liu, C. P. Teng*, et al.*, "Recent Progress in Energy-Driven Water Splitting," *Advanced Science,* 2017.

[8] M. A. Pellow, C. J. Emmott, C. J. Barnhart, and S. M. Benson, "Hydrogen or batteries for grid storage? A net energy analysis," *Energy & Environmental Science,* vol. 8, pp. 1938-1952, 2015.

[9] X. Yang, H. Li, A.-Y. Lu, S. Min, Z. Idriss, M. N. Hedhili*, et al.*, "Highly acid-durable carbon coated Co 3 O 4 nanoarrays as efficient oxygen evolution electrocatalysts," *Nano Energy,* vol. 25, pp. 42-50, 2016.

[10] N.-T. Suen, S.-F. Hung, Q. Quan, N. Zhang, Y.-J. Xu, and H. M. Chen, "Electrocatalysis for the oxygen evolution reaction: recent development and future perspectives," *Chemical Society Reviews,* vol. 46, pp. 337-365, 2017.

[11] O. Diaz-Morales, S. Raaijman, R. Kortlever, P. J. Kooyman, T. Wezendonk, J. Gascon*, et al.*, "Iridium-based double perovskites for efficient water oxidation in acid media," *Nature communications,* vol. 7, p. 12363, 2016.

[12] R. D. Smith, M. S. Prévot, R. D. Fagan, Z. Zhang, P. A. Sedach, M. K. J. Siu*, et al.*, "Photochemical route for accessing amorphous metal oxide materials for water oxidation catalysis," *Science,* p. 1233638, 2013.

[13] Y. Zhu, W. Zhou, Y. Zhong, Y. Bu, X. Chen, Q. Zhong*, et al.*, "A Perovskite Nanorod as Bifunctional Electrocatalyst for Overall Water Splitting," *Advanced Energy Materials,* vol. 7, 2017.

[14] H. Li, S. Chen, X. Jia, B. Xu, H. Lin, H. Yang*, et al.*, "Amorphous nickel-cobalt complexes hybridized with 1T-phase molybdenum disulfide via hydrazine-induced phase transformation for water splitting," *Nature Communications,* vol. 8, 2017.

[15] S. Zhao, Y. Wang, J. Dong, C.-T. He, H. Yin, P. An*, et al.*, "Ultrathin metal–organic framework nanosheets for electrocatalytic oxygen evolution," *Nature Energy,* vol. 1, p. 16184, 2016.

[16] C. C. McCrory, S. Jung, J. C. Peters, and T. F. Jaramillo, "Benchmarking heterogeneous electrocatalysts for the oxygen evolution reaction," *Journal of the American Chemical Society,* vol. 135, pp. 16977-16987, 2013.

[17] R. O'Hayre and F. B. Prinz, "The air/platinum/nafion triple-phase boundary: characteristics, scaling, and implications for fuel cells," *Journal of The Electrochemical Society,* vol. 151, pp. A756-A762, 2004.

[18] J. Mo, Z. Kang, S. T. Retterer, D. A. Cullen, T. J. Toops, J. B. Green*, et al.*, "Discovery of true electrochemical reactions for ultrahigh catalyst mass activity in water splitting," *Science Advances,* vol. 2, p. e1600690, 2016.

[19] X. Lu, W.-L. Yim, B. H. Suryanto, and C. Zhao, "Electrocatalytic oxygen evolution at surface-oxidized multiwall carbon nanotubes," *Journal of the American Chemical Society,* vol. 137, pp. 2901-2907, 2015.

[20] R. I. Jafri, N. Rajalakshmi, and S. Ramaprabhu, "Nitrogen doped graphene nanoplatelets as catalyst support for oxygen reduction reaction in proton exchange membrane fuel cell," *Journal of Materials Chemistry,* vol. 20, pp. 7114-7117, 2010.

[21] T. Reier, H. N. Nong, D. Teschner, R. Schlögl, and P. Strasser, "Electrocatalytic Oxygen Evolution Reaction in Acidic Environments–Reaction Mechanisms and Catalysts," *Advanced Energy Materials,* 2016.

[22] X. Sun and H. Li, "Gold nanoisland arrays by repeated deposition and post-deposition annealing for surface-enhanced Raman spectroscopy," *Nanotechnology,* vol. 24, p. 355706, 2013.

[23] M. Walther, D. Cooke, C. Sherstan, M. Hajar, M. Freeman, and F. Hegmann, "Terahertz conductivity of thin gold films at the metal-insulator percolation transition," *Physical Review B,* vol. 76, p. 125408, 2007.

[24] P. Malinský, P. Slepička, V. Hnatowicz, and V. Švorčík, "Early stages of growth of gold layers sputter deposited on glass and silicon substrates," *Nanoscale research letters,* vol. 7, p. 241, 2012.

[25] J. Siegel, O. Lyutakov, V. Rybka, Z. Kolská, and V. Švorčík, "Properties of gold nanostructures sputtered on glass," *Nanoscale research letters,* vol. 6, p. 96, 2011.

[26] K. Chopra, L. Bobb, and M. Francombe, "Electrical Resistivity of Thin Single-Crystal Gold Films," *Journal of Applied Physics,* vol. 34, pp. 1699-1702, 1963.

[27] A. Grimaud, A. Demortière, M. Saubanere, W. Dachraoui, M. Duchamp, M.-L. Doublet*, et al.*, "Activation of surface oxygen sites on an iridium-based model catalyst for the oxygen evolution reaction," *Nature Energy,* vol. 2, p. 16189, 2017.

[28] M. Cabán-Acevedo, M. L. Stone, J. Schmidt, J. G. Thomas, Q. Ding, H.-C. Chang*, et al.*, "Efficient hydrogen evolution catalysis using ternary pyrite-type cobalt phosphosulphide," *Nature materials,* vol. 14, p. 1245, 2015.

[29] Z. Li, X. Dou, Y. Zhao, and C. Wu, "Enhanced oxygen evolution reaction of metallic nickel phosphide nanosheets by surface modification," *Inorganic Chemistry Frontiers,* vol. 3, pp. 1021-1027, 2016.

[30] S. Song, H. Zhang, X. Ma, Z. Shao, R. T. Baker, and B. Yi, "Electrochemical investigation of electrocatalysts for the oxygen evolution reaction in PEM water electrolyzers," *international journal of hydrogen energy,* vol. 33, pp. 4955-4961, 2008.

[31] M. Mandal, A. Valls, N. Gangnus, and M. Secanell, "Analysis of Inkjet Printed Catalyst Coated Membranes for Polymer Electrolyte Electrolyzers," *Journal of The Electrochemical Society,* vol. 165, pp. F543-F552, 2018.

[32] Y. Wang, S. Narayanan, and W. Wu, "Field-Assisted Splitting of Pure Water Based on Deep-Sub-Debye-Length Nanogap Electrochemical Cells," *ACS nano,* vol. 11, pp. 8421-8428, 2017.

[33] Z. Kang, J. Mo, G. Yang, Y. Li, D. A. Talley, B. Han*, et al.*, "Performance Modeling and Current Mapping of Proton Exchange Membrane Electrolyzer Cells with Novel Thin/Tunable Liquid/Gas Diffusion Layers," *Electrochimica Acta,* vol. 255, pp. 405-416, 2017.

[34] Z. Kang, J. Mo, G. Yang, S. T. Retterer, D. A. Cullen, T. J. Toops*, et al.*, "Investigation of thin/well-tunable liquid/gas diffusion layers exhibiting superior multifunctional performance in low-temperature electrolytic water splitting," *Energy & Environmental Science,* 2017.

[35] M. Bernt, A. Siebel, and H. A. Gasteiger, "Analysis of Voltage Losses in PEM Water Electrolyzers with Low Platinum Group Metal Loadings," *Journal of The Electrochemical Society,* vol. 165, pp. F305-F314, 2018.

[36] A. Wittstock, V. Zielasek, J. Biener, C. Friend, and M. Bäumer, "Nanoporous gold catalysts for selective gas-phase oxidative coupling of methanol at low temperature," *Science,* vol. 327, pp. 319-322, 2010.

[37] C. Li, Ö. Dag, T. D. Dao, T. Nagao, Y. Sakamoto, T. Kimura*, et al.*, "Electrochemical synthesis of mesoporous gold films toward mesospace-stimulated optical properties," *Nature communications,* vol. 6, p. 6608, 2015.

[38] C. Rozain, E. Mayousse, N. Guillet, and P. Millet, "Influence of iridium oxide loadings on the performance of PEM water electrolysis cells: Part I–Pure IrO2-based anodes," *Applied Catalysis B: Environmental,* vol. 182, pp. 153-160, 2016.

Appendix

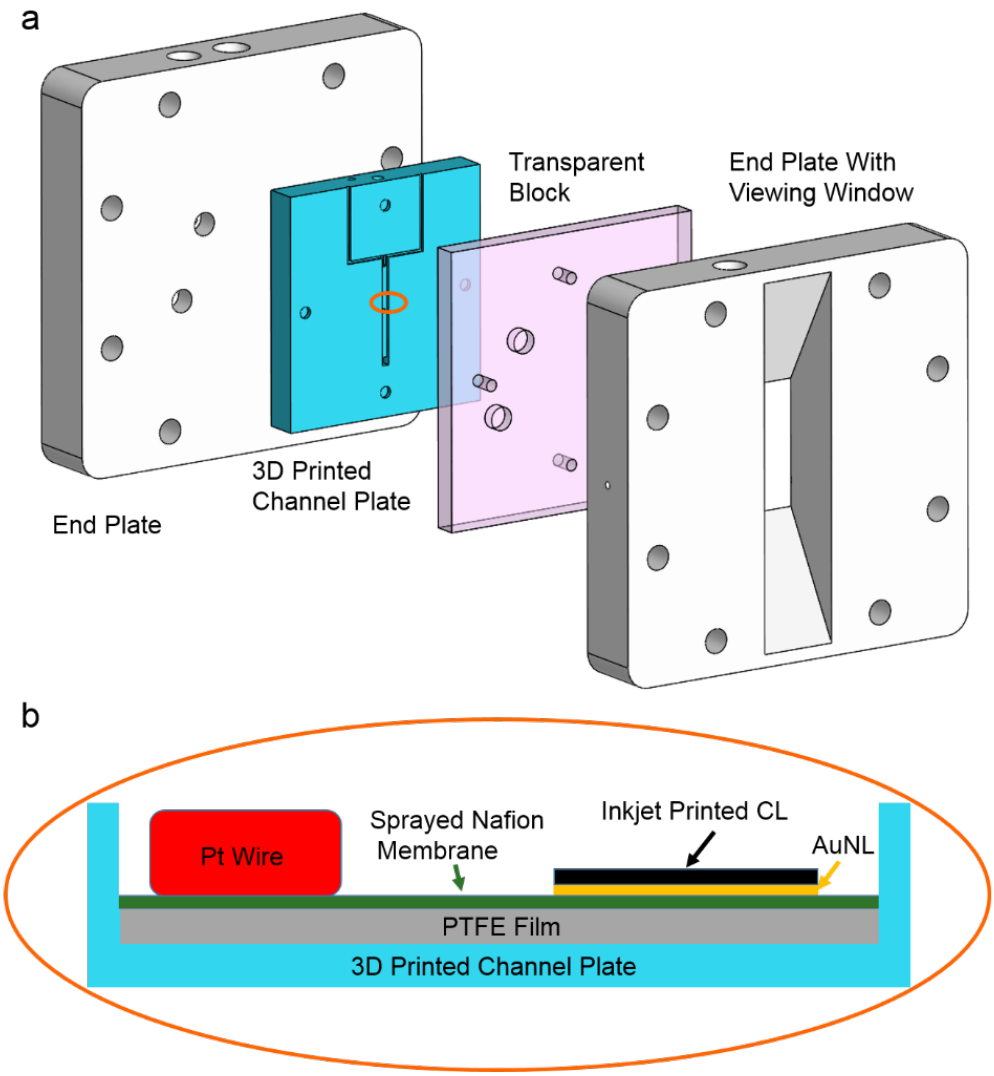

Figure 39. (a) Schematic of the novel PEMEC with coplanar electrodes. (b) Schematic of the cross-section of the coplanar electrodes.

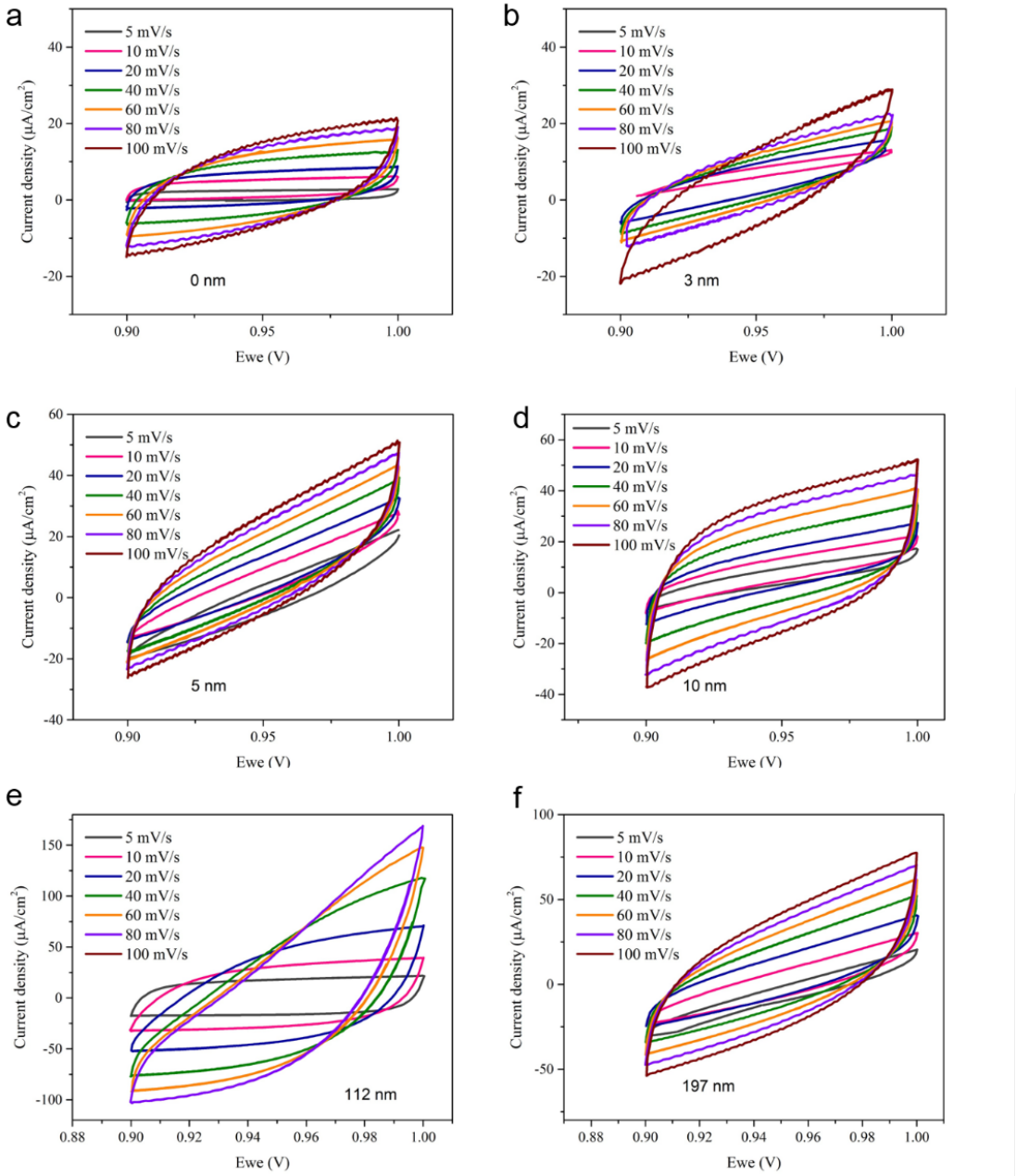

Figure 40. Cyclic voltammetrys (CVs) of CMBMCs with a AuNL thickness of 0 (a), 3 (b), 5 (c), 10 (d), 112 (e), and 197 nm (f) scanned from 0.9 V to 1.0 V at different scan rate.

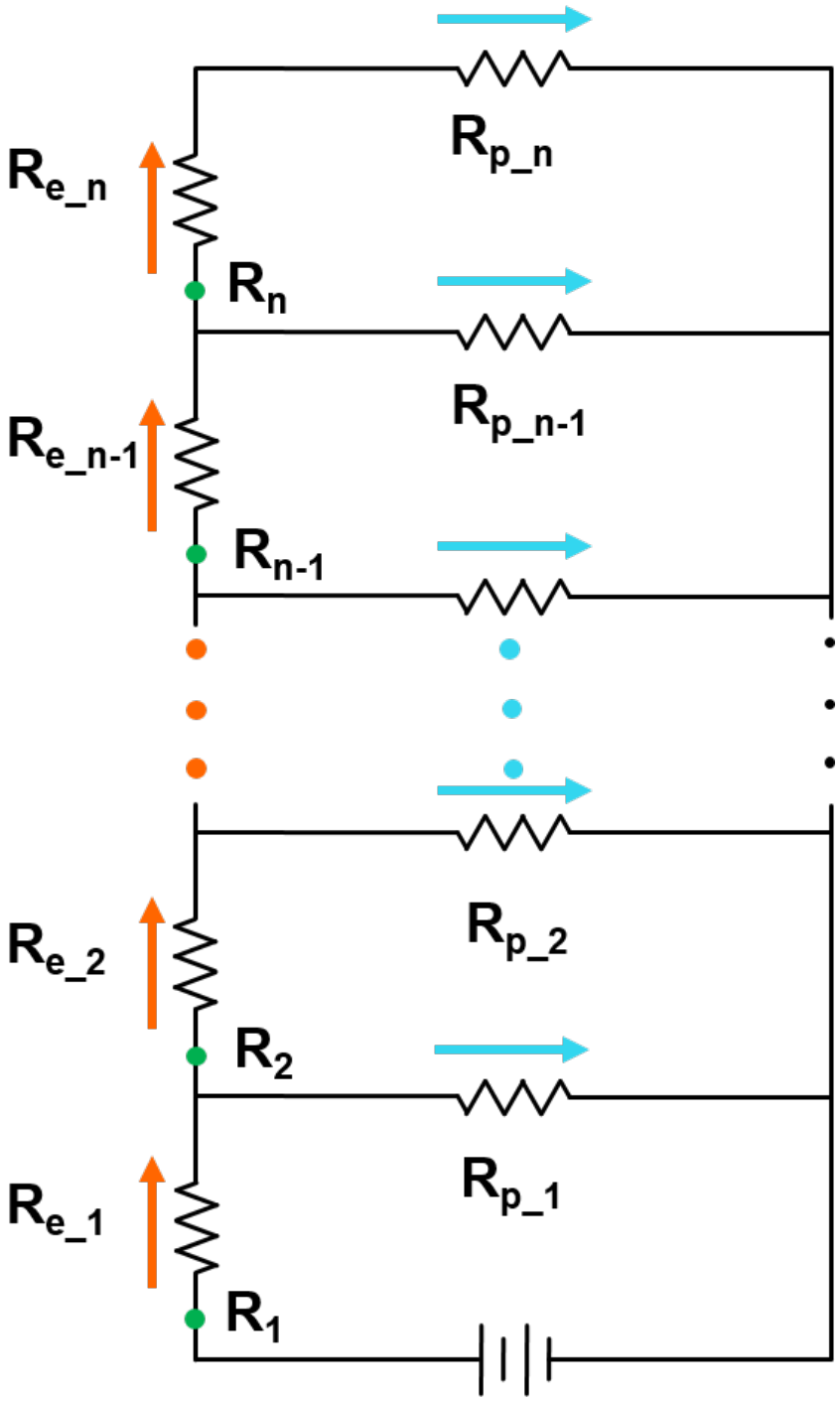

Figure 41. Circuit of the electronic resistance on the CL and the protonic resistance on proton membrane

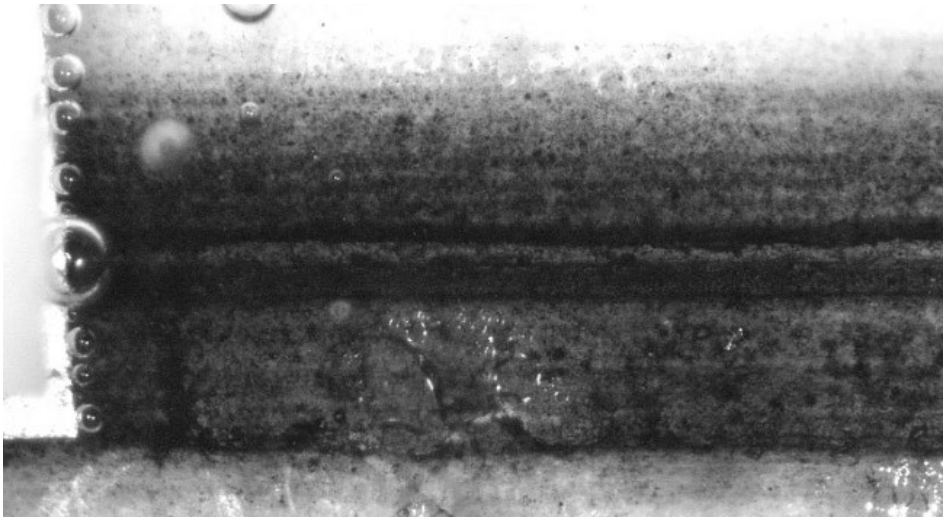

Figure 42. Visualization of OERs on CMBMC-3AuNL.

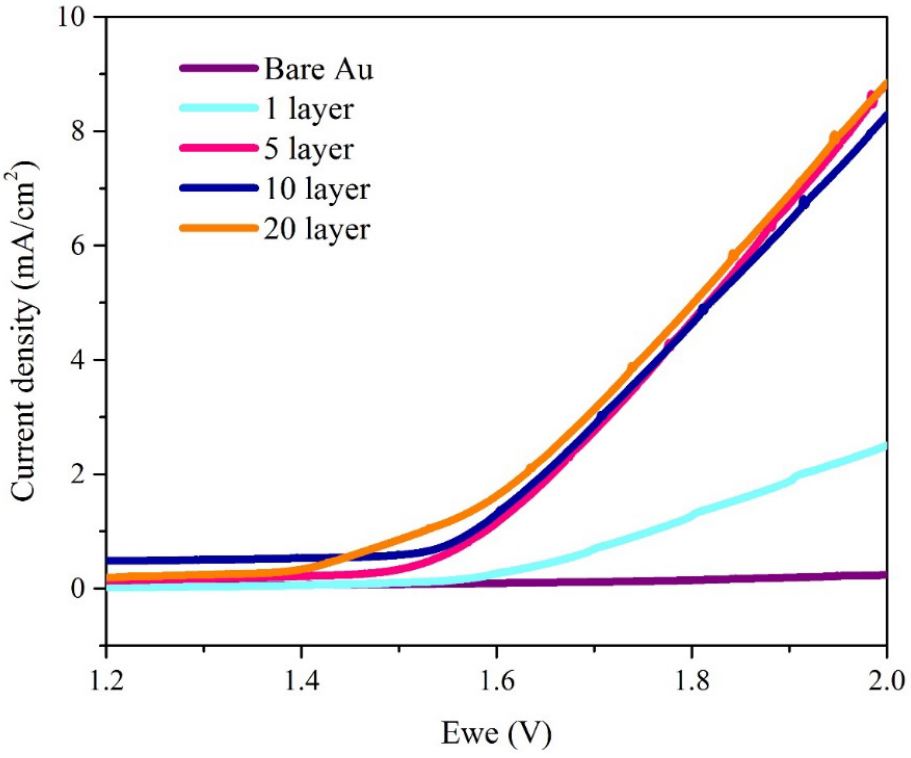

Figure 43. LSV of CMBMCs with different loadings

CHAPTER VIII

CONCLUSIONS AND FUTURE RESEARCH

In this thesis, advanced manufacturing methods, including selective laser melting, fusion extrusion, inkjet printing, electroplating, sputtering coating, spray method, have been employed to facilitate fundamental materials and structure innovations, which significantly increase the energy-conversion efficiency, and reduce the cost, weight, volume and component number of PEMECs. *Ex-situ* and *in-situ* characterizations were conducted to comprehensively investigate the performance of synthesized materials and parts. Numerical simulations and visualizations were also used to reveal the mechanism of the good performance of those novel PEMECs.

Firstly, the multifunctional and integrated cells with highly complex inner structures, which served as a combination of several components in PEMECs, were developed from stainless steel powders with the selective lase melting. To the best of our knowledge, it is the first time that the PEMEC parts are integrated into one plate for water splitting and hydrogen production. The structural innovations of the plates provide a fundamental development for the simplification of PEMECs, which significantly reduce their part number and weight. Moreover, an excellent performance of 1.716 V is achieved at 80 °C and 2 A/cm^2, which leads to the superior efficiency of 86.48% due to the ultralow ohmic resistance. Then EIS results are simulated with equivalent electrochemical circuits (EECs) to characterize the resistance, impedance, and capacitance in AM PEMECs. These results demonstrate the viability of efficient PEMECs with ultralow ohmic resistances for

hydrogen production. The AM technology opens the opportunity for optimal configurations of PEMECs, as well as marks a new step to the development of other energy conversion devices.

Secondly, to promote the corrosion resistance of stainless steel BPs printed with the selective laser melting (SLM) in an oxygen rich anodic ambient, we coated the BPs with thin film Au by an electroplating process. To the best of our knowledge, this is the first time that AM SS BPs were used at both the cathode and anode sides for water splitting in PEMECs. The electrodes with SS BPs printed by AM at both sides possess a much lower ICR, 6.4 $m\Omega \cdot cm^2$ under 1.45 MPa, and a much lower voltage (higher efficiency) of 1.71 V at 2 A/cm^2, compared to conventional electrodes with an ohmic resistance of 17.0 $m\Omega \cdot cm^2$ and voltage of 1.887 V under the same operating conditions. The corrosion tests, conducted in a three-electrode assembly, demonstrate that the Au-electroplated AM SS BPs have good corrosion resistance and durability for 100 h under simulated acidic and high-voltage conditions. This research demonstrates that a protective coating enables the application of additively manufactured components of inexpensive materials on highly integrated PEMECs for low-cost, efficient water splitting and hydrogen production.

Thirdly, a novel PEMEC with non-conductive BPs and TF-LGDLs is developed to reduce the cost and improve the performance of overall water splitting. The rapidly printed non-conductive PLA BPs without post-processing (coating, plating, etc.) enable mass distribution and provide mechanical support for the cell. A TF-LGDL with surroundings wet-etched with Ti film offers a new electron conduction path, which directly transports

electrons in or out of PEMECs laterally. In PEMECs, PLA BPs exhibit an extremely low cost (1/10 of the graphite BP), and their hydrogen production rate per unit BP cost is almost 6 times higher than that of a conventional cell. Furthermore, a relatively low voltage of 2.21 V at 1 A/cm^2 under room temperature and a good stability with an average degradation rate of 1.03 mV/h are achieved in the PEMEC with PLA BPs. The numerical simulation helps to connect the resistivity of BPs and the cell performance, and then a threshold value of 0.433 Ω·cm is derived for guiding the selection of BPs material. The accessible and extremely low-cost BP as well as the good electrochemical performance will open a road to developing plastic materials for low cost water splitting or energy conversion devices, such as batteries, solar cells, and fuel cells.

More importantly, we developed a facile method for fabricating 2-D CMBMCs with advanced manufacturing, which enable the ultra-high mass activity for oxygen evolution reaction. The CMBMCs exhibit excellent electrical conductivity (0.54 Ω/□) due to the easily controllable conductive AuNLs. The mesopores on the sputter-coated AuNLs that allow the transport of proton to nafion membrane were discovered. Moreover, the novel structure of the CMBMCs facilitates the direct investigation of the influence of conductivity on OER kinetics, and thus the relationship between conductivity and reaction length or site is established. The OER kinetics of noble-metal catalysts with low loading (0.1195 mg/cm^2) is three times faster than that of conventional IrO_2 CLs, allowing for the wide application of noble-metals in energy conversion devices.

In summary, this research demonstrates that AM technologies with other advanced manufacturing methods have profound potential for the development of high efficiency and low-cost energy conversion devices and will facilitate the wide application of PEMECs to build a hydrogen society.

In the future, more complex and delicate LGDLs can be printed with BPs by using metallic AM technologies in order to increase the reaction area and improve the efficiency of PEMECs, because the AM SS plate contains a LGDL and a BP in Chapter III has a mass transport issue as a result of large pore sizes and small porosities. Furthermore, ceramic components with electrical conductivity can be developed for water splitting by binder jetting technology, which involves mixing materials of ceramic powders and metal powders and then going through post-processing, such as pyrolysis. In this way, the cost of BPs and other components will be reduced. More advanced manufacturing methods, such physical vapor deposition (PVD), chemical vapor deposition, dry etching, and wet etching can also be used to fabricate LGDLs and CLs so as to develop new structures of CL for both OERs and HERs. With the combination of the metallic AM method and 3D inkjet printing, it would be possible to produce fully integrated PEMECs. If so, the rapid prototyping of energy conversion devices would be widely applied among the research community.

VITA

Gaoqiang Yang was born in Qixian, Henan, China. He studied in Henan Agricultural University from 2008 to 2012 for the B.S. degree in major of Thermal and Power Engineering. Then he went to graduate school at the Southeast University in Nanjing where he received his M.S. in Power Engineering in 2015. He began to study at the University of Tennessee, Knoxville (UTK) in Mechanical Engineering for Ph.D. degree from 2016.